DECAY CHARACTERISTICS OF Xe^{138}

DECAY CHARACTERISTICS OF Xe^{138}

by

NORMAN PHILIP ARCHER, B.Sc.

A Thesis

Submitted to the Faculty of Graduate Studies

in Partial Fulfilment of the Requirements

for the Degree

Doctor of Philosophy

McMaster University

September, 1965

DOCTOR OF PHILOSOPHY (1965)

McMASTER UNIVERSITY
Hamilton, Ontario

TITLE: Decay Characteristics of Xe^{138}

AUTHOR: Norman Philip Archer, B. Sc. (University of Alberta)

SUPERVISOR: Dr. G. L. Keech

NUMBER OF PAGES: xi, 75, A62

SCOPE AND CONTENTS:

Experimental techniques which are useful in nuclear spectroscopy studies of the radioactive fission-product rare gases have been developed, and applied to the study of the decay characteristics of Xe^{138}. A decay scheme of this nucleus is proposed which is based upon the experimental results obtained. The use of digital computer techniques in the analysis of scintillation spectroscopy data is also discussed in detail.

ACKNOWLEDGEMENTS

The list of the individuals who have assisted me in the preparation of the work described in this thesis is very long indeed.

First of all I would like to thank my supervisor, Dr. G. L. Keech, for his thoughtful advice and encouragement throughout the period of this study. His friendly assistance has been greatly appreciated. I would especially like to thank Dr. T. J. Kennett with whose group I have had the privilege of working, and whose attitude that scientific research is amusing as well as interesting has helped to make this work enjoyable. To Dr. W. V. Prestwich I wish to express my gratitude for many stimulating and enlightening discussions. The work described in this thesis which entails chemical analysis would have been impossible without the collaboration of Dr. H. J. Fiedler to whom I am greatly indebted. I wish to thank Mr. Darius Slavinskas for the use of his beta-analysis computer programs and also Mr. Larry Johnson and Mr. Geoffrey Norman for their assistance in the preparation of this work. To the atomic beam group, and especially Mr. Glen Stinson, I owe a debt of thanks for their collaboration in the nuclear spin measurements. I wish also to thank the McMaster reactor staff and the McMaster computation centre staff for their advice and assistance.

I would like to thank my wife, whose literary criticisms have greatly improved the quality of my writing. I am also greatly indebted to Mrs. Helen Kennelly, whose fast and accurate typing have been of great value in the preparation of this work.

This work has been supported financially by the National Research Council of Canada.

TABLE OF CONTENTS

APPENDICES

LIST OF TABLES

APPENDIX TABLES

LIST OF ILLUSTRATIONS

CHAPTER I

INTRODUCTION

The study of the beta-decay of unstable nuclei has proved to be a fruitful source of information on nuclear structure. A detailed knowledge of certain configurations which may be formed by the constituent nucleons is made possible through the study of the modes by which the excited eigen-states are populated and also the study of their de-excitation modes. The excitation process is, in this case, the process of beta-decay by the parent nucleus while de-excitation of the states in the newly-created daughter nucleus usually occurs by either gamma emission or internal conversion.

The beta decay process results in a transformation of the parent nucleus, with mass number and atomic number denoted by (A,Z), to a product nucleus (A,Z + 1). The probability of this process is proportional to

$$\left| \langle \psi_f \phi_f \right| H \left| \psi_i \phi_i \rangle \right|^2 \rho(E) \qquad (1.1.a)$$

where H is the weak interaction Hamiltonian, ψ_i, ψ_f are the initial and final nuclear wave functions, and ϕ_i, ϕ_f refer to the initial and final lepton states. $\rho(E)$ is the density of final states. This discussion will be limited to negative beta-particle decay; in this case the decay process results in the emission of a neutrino and a negaton. The total energy released in a ground state negaton transition is

$$\Big\{ M(A,Z) - M(A,Z+1) \Big\} C^2 = \Delta E$$

provided that the electronic binding energy of the last electron may be

neglected. Here, M(AZ) and M(A,Z + 1) are the atomic masses of the parent and daughter nuclides respectively.

The relativistic negaton energy will be denoted by E, and W_ν will refer to the neutrino energy. Hence,

$$\Delta E = E - M_o c^2 + W_\nu$$

where M_o is the electron rest mass.

If a state in the daughter nucleus is populated which subsequently decays by gamma emission, then

$$\Delta E = E - M_o c^2 + W_\nu + E_\gamma \qquad (1.1.b)$$

ΔE in both the above equations is also referred to as the Q-value for the decay. The neutrino has a zero rest-mass and exhibits a continuous probability distribution in energy which ranges from zero energy to W_o, the end-point energy. The emitted negatons will have a corresponding distribution according to equation (1.1.b) and the same end-point W_o. Thus equation (1.1.b) may be modified to read

$$Q = W_o - M_o c^2 + E_\gamma \qquad (1.1.c)$$

The conversion of equation (1.1.a) to an equation in experimentally observable quantities is dealt with in standard references (1,2). The negaton has an energy distribution N(E) with a probability per unit time of emission of a particle into the energy interval dE given by

$$N(E)dE = \frac{1}{2\pi^3} pE(W_o - E)^2 F(Z,E) S_n(W_o,E) \qquad (1.1.d)$$

$$= N(p,q)dE = \frac{1}{2\pi^3} pEq^2 F(Z,E) S_n(W_o,E)$$

Here, p is the beta-particle momentum,

q is the neutrino momentum

F(Z,E) is the Fermi function which allows for Coulomb and electronic screening effects, and

S_n (W_o,E) is the "shape factor".

S_n is the purely nuclear dependent parameter, containing the matrix elements of the transition. The form of S_n is dependent upon the type of the transition which is subject to certain selection rules based on the conservation of angular momentum.

For beta-transitions from the state having spin J_i and parity π_i to the state J_f,π_f, only transitions having total lepton angular momentum ΔJ are permitted, where

$$\left|J_i - J_f\right| \leqslant \Delta J \leqslant J_i + J_f$$

For allowed transitions, $\Delta J = 0$ or 1 and $\pi_i = \pi_f$. In this case the shape factor S_o is not dependent upon beta-particle energy.

For first-forbidden transitions, $\pi_i\pi_f = -1$ and $\Delta J = 0$, 1 or 2. The shape factor, S_1, is usually considerably smaller than S_o. For $\Delta J = 0$ or 1 there is normally a minimal energy dependence in S_1. The type of first-forbidden transitions with $\Delta J = 2$ are referred to as "first-forbidden unique" transitions and in this case S_1 has an energy dependence which is proportional to $(q^2 + p^2)$. This is a useful property from the experimental point of view because this type of transition can be identified by observation of the measured spectral shape.

The end-point W_o of a measured beta spectrum is usually determined by plotting $\left\{N(E)/pE\ F(Z,E)\ S_n(W_o,E)\right\}^{\frac{1}{2}}$ against negaton energy. Such a plot is referred to as a Fermi plot of the spectrum and, according to equation (1.1.d) should be linear with intercept W_o.

Nuclear beta-decay rates are useful as an aid in determining nuclear spins and parities, and moreover when the spins and parities have been determined, the decay rates may be related to the matrix elements of the transition. The decay rate may be determined by integrating equation (1.1.d).

Thus,

$$\lambda = \int_1^{W_o} N(E)dE$$

$$= \frac{1}{2\pi^3} \int_1^{W_o} pE(W_o - E)^2 F(Z,E) S_n(W_o,E) dE$$

The decay rate is seen to be roughly proportional to W_o^5. If a quantity $f(Z,W_o)$ is defined,

$$f(Z,W_o) = \int_1^{W_o} F(Z,E) pE(W_o - E)^2 dE$$

then

$$\frac{f}{\lambda} = \frac{ft_{1/2}}{\ln 2} \propto \frac{1}{S_n}$$

Here the energy dependence of the function S_n has been removed by assuming an average value. The quantity $ft_{1/2}$ is referred to as the comparative half-life for the transition. Tables of $f(Z,W_o)$ are available in several works (3,4). Since the value of ft is inversely proportional to the matrix element for the transition, this quantity is an indication of the type of transition involved. When there are beta transitions to more than one state in the transformed nucleus, then the partial decay rate λ_p for

transitions to each level is appropriate to this discussion. The partial decay rate to a level is given by $\lambda_p = \lambda/b$, where b is the branching to that level, and λ is the total decay rate. A systematic tabulation of $\log_{10}$ ft for beta-decays in which the type of transition is known has been made by Feenberg (5). Allowed transitions have been found to fall into two groups. The first group has $\log_{10}$ ft of approximately 3.0 to 3.7 and corresponds to the 'super-allowed' transitions in which $\Delta l = 0$ for the transformed nucleon. The remainder of allowed transitions have a $\log_{10}$ ft distributed about a mean value of 5. This class is more peculiar to the heavier nuclides (with $A > 40$). First forbidden transitions have $\log_{10}$ ft grouped around 7, except that first forbidden unique transitions tend to a mean value of about 9.

It is appropriate, since the present work involves the beta decay of the nuclide ${}_{54}Xe^{138}_{84}$, to obtain the distribution of ft values in this region as an aid in determining the types of beta-transitions involved. Beta-transitions in this region will involve matrix elements more appropriate to the nuclear structure of this nuclide. The distribution of $\log_{10}$ ft for established allowed and first-forbidden transitions in the region $82 < N < 90$ and $50 < Z < 60$ is shown in Figure 1.

The mean value of log ft for allowed transitions shown in the figure is 6.3 while the mean value for first-forbidden transitions is 7.5 . However, the overlap of the two distributions indicates that log ft values are not particularly definitive of the type of transition in this region.

GAMMA DECAY

The mode by which de-excitation by gamma-ray emission occurs depends primarily on three factors: the spin change $|J_i - J_f|$, the

FIGURE 1

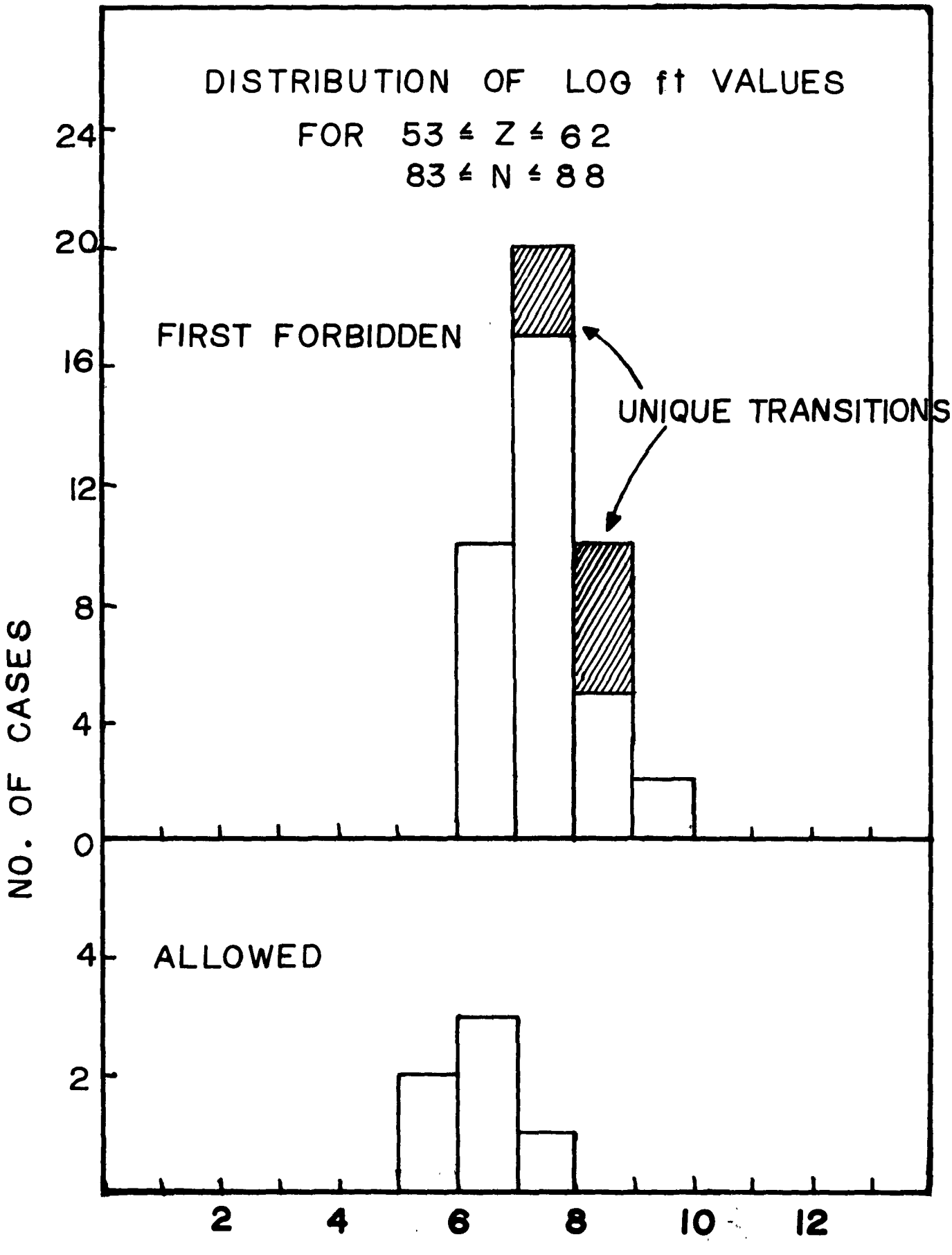
DISTRIBUTION OF LOG ft VALUES
FOR 53 ≤ Z ≤ 62
83 ≤ N ≤ 88
FIRST FORBIDDEN
UNIQUE TRANSITIONS
ALLOWED
NO. OF CASES
24
20
16
12
8
4
0
4
2
2
4
6
8
10
12

energy of the transition, and the parity change between the initial and final states. The selection rules for photon emission of multipolarity L are

$$\left|J_i - J_f\right| \leq L \leq J_i + J_f, \text{ no } 0 \longrightarrow 0 \qquad (1.1.e)$$

Here, as before, J_i and J_f are the spins of the initial and final states, respectively. For electric multipole transitions the parity change between J_i and J_f is $\pi_i\pi_f = (-1)^L$, and for magnetic transitions the parity change is $\pi_i\pi_f = (-1)^{L+1}$. According to single particle estimates by Weisskopf (6) and Moszkowski (7) of gamma-transition probabilities, the lifetime of the excited level is proportional to $E_\gamma^{-(2L+1)}$. Tables showing the Weisskopf single-particle estimates appear in Preston (1). Comparisons between these values and measured values for gamma-transition rates are also shown in the same reference.

The L-dependence in the predicted life-time tends to restrict the type of gamma-transition to the lowest multipolarity, $L = \left|J_i - J_f\right|$. However when the lowest multipolarity transition is necessarily a magnetic transition, the next highest electric transition will contribute to the decay. The reverse is generally not true. For example, E2 transitions will compete with M1 transitions, but an M2 transition rate is generally low compared to the E1 transition rate. The ratio of the magnetic to the electric multipole contributions to the transition is defined as the mixing ratio for the transition.

INTERNAL CONVERSION

In competition with gamma-ray emission is internal conversion where the nucleus de-excites by the transfer of the transition energy to an atomic electron. The conversion electron is expelled from the atom

with an energy

$$E_c = E_\gamma - E_B$$

where E_B is the electron binding energy. Tne ratio of the probability of internal conversion to the probability of gamma emission is the conversion coefficient α, where

$$\alpha = \frac{N_e}{N_\gamma}$$

The conversion coefficient is dependent upon the atomic number of the decaying nucleus, the energy of the transition, and the multipolarity of the transition. Since the atomic number and the transition energy are known, a measurement of α will often suffice to determine the multipolarity of the transition. Tabulations of α as a function of Z and E_γ for various transition multipolarities are available in several references (8,9).

NUCLEAR MODEL PREDICTIONS FOR ODD-ODD NUCLEI

The nuclear shell model as suggested by Mayer (10), and Haxel, Jensen and Suess (11), has enjoyed a great deal of success in the prediction of nuclear properties, and in particular the ground state spins of odd-A nuclei. If the nucleus in question is in the regions of the periodic table where deformed nuclei are observed, then it is necessary to modify the spherical potential of the shell model to a non-spherical form which is due to the deformed nuclear core. Such a combination of collective and single particle configurations is known as the unified model. Since both collective and single-particle modes are important in the explanation of the properties of most nuclei, the following brief discussion will include the contributions to be expected from each mode in odd-odd nuclei.

The successful shell model predictions for ground state spins and parities of many odd-A nuclei is due to the fact that, in most cases, the single odd particle may be treated as moving independently in the nuclear field. Low energy excitations in these nuclei are often associated with a transition of the odd particle from one state to another and consequently only its average interaction with the rest of the nucleus is involved.

A ground-state spin of zero is always observed in even-even nuclei. This is due to the pairing force which couples all nucleon pairs in each shell to zero effective spin. In the region of spherical nuclei, the first excited state of an even-even nucleus is usually due to a collective vibrational mode, brought on by the excitation of a quadrupole phonon. More highly excited states may be due either to collective or intrinsic particle excitations.

Of great interest in the study of nuclear structure is the form of the nucleon-nucleon interaction in the presence of the field due to the remainder of the nucleus. The interaction for each of the two unpaired particles of the odd-odd nucleus is accounted for to a large extent in the single-particle shell-model potential which represents the average effect on one nucleon of the remaining nucleons. The remainder of the interaction may be described by an effective force between the two odd nucleons and is referred to as the "residual" nucleon-nucleon interaction. Unfortunately the study of this interaction in odd-odd nuclei is inhibited by the fact that shell-model states other than the ground-state configuration in such nuclei often occur at very low energies. The presence of other nucleons in the same unfilled shells will tend to obscure the relatively simple single neutron-proton coupling interaction. However,

the spins of the ground state and the first few excited states of such nuclei should provide a basis of comparison with theoretical predictions. The ground-state spins of many odd-odd nuclei follow empirical rules postulated by Nordheim (12) and further modified by Brennan and Bernstein (13). These rules state that, if we denote Nordheim's number by N, where

$$N = j_p - l_p + j_n - l_n$$

and j_p, l_p and j_n, l_n refer to the total angular momentum and orbital angular momentum of the unpaired proton and neutron respectively, then if the ground-state spin of the odd-odd nucleus is J, then

$$J = \left| j_n - j_p \right| \qquad \text{if } N = 0 \qquad \text{(strong rule)}$$

$$J = j_n + j_p \text{ or } \left| j_n - j_p \right| \quad \text{if } N = \pm 1 \text{ (weak rule)}$$

Theoretically it has been shown that the tendency to obey these rules is due to the greater strength of triplet as opposed to singlet coupling between the unpaired particles. There is therefore a likelihood that the nucleons will tend to couple with parallel intrinsic spins. The theory of such j-j coupling between the odd nucleons has been given in detail by deShalit and Walecka (14). A multiplet of levels should also be observed with spins ranging in order of level energy from $\left| j_n - j_p \right|$ to $j_n + j_p$, providing that there is no interference from other configurations.

The agreement of the measured values of ground-state spins for odd-odd nuclei with the Nordheim coupling rules is impressive since the rules can account for greater than 60% of 139 known values (15). The values for j_p, j_n, l_p and l_n are usually inferred from neighboring odd-A nuclei. Inversion of the single-particle levels has often been found in odd-odd nuclei as compared with odd-A neighbors if the shell model levels lie close together in energy.

A more valid test of the theory is afforded by the manner in which the two odd nucleons couple when these nucleons are the only particles outside major shell closures. Such an example is $_{83}Bi^{210}_{127}$. Here, the proton and neutron lie outside the major shells of 82 protons and 126 neutrons, respectively. The level structure of this nucleus has been studied experimentally by Erskine et al (16). According to the shell model predictions the odd proton should be in the $h_{9/2}$ configuration and the odd neutron should be in the $g_{9/2}$ configuration. If the theoretical predictions for the j-j coupling model are valid, then a multiplet of levels should be observed, with spins ranging from 0- to 9-, in that order. The predicted ground-state spin is 0-, according to Nordheim's strong rule. The multiplet is observed. However, the 0- and 1- levels are inverted and the 9-level is much lower in the sequence than predicted. Kim and Rasmussen (17) have performed extensive calculations for this nucleus, obtaining agreement with experiment only when allowing both tensor and central forces in the residual interaction, along with a certain amount of configuration mixing. When faced with the complexity of these arguments for what is, in theory, the simple case, there is a tendency to wonder whether or not the impressive prediction of ground state spins in far more complex configurations is fortuitous. This is particularly true of the region $35<Z<50$, $40<N<65$, where the shell-model levels for each odd nucleon lie rather close in energy and there is an increasing probability of configuration mixing. In many cases there are several other nucleons in the same shell as the odd nucleon. These nucleons would not be expected to behave as inert closed shell particles. The predicted multiplets very seldom appear in the proper sequence if at all, although the ground-state

spin prediction is often correct. It is true, however, that some of these states are not easily populated.

One region where even the ground state spin prediction is invalid is in the region $50 < Z < 60$, $82 < N < 90$, just above doubly magic shells. Table I lists the observed ground state spins for nuclei in this region as compared to predictions by the modified Nordheim's rules.

TABLE I

Observed Ground State Spins of Odd-Odd Nuclei

for $52 < Z < 62$, $82 < N < 88$

Z \ N	83	85	87
53	(2-)		
55	3(-)		
57	3 -	2 -	
59	2 -	0 -	2 -
61	(5-,6-)	(2-)	(1-,2-)

Note: According to Nordheim's coupling rules the predicted spins are:

$I =$ 0 - for $1g_{7/2}$, $2f_{7/2}$ p-n coupling (strong rule)

6- or 1- for $2d_{5/2}$, $2f_{7/2}$ p-n coupling (weak rule)

The possible proton configurations considered are $1g_{7/2}$ and $2d_{5/2}$, since both of these ground-state configurations are found in odd-proton nuclei in this region. The neutron configuration is $2f_{7/2}$

according to measurements by Cohen (18). The lack of agreement of observed ground-state spins with the Nordheim rule predictions is notable. However, there seems to be a trend toward agreement with predicted values which improves inversely to "nearness" to the doubly magic shell. Since ground-state spin predictions in this region are poor it is unlikely that extrapolation to predictions for excited levels is valid. Kisslinger and Sorenson (19) have postulated that phonon coupling to the j-j coupled particles in this region may improve the theoretical predictions. However, they have not performed an extensive analysis for odd-odd nuclei. Since the predictions for nuclei in this region are unsatisfactory, it is preferable to use an interpolation between similar nuclei in order to compare results. This comparison will be made in the discussion of experimental results for the Cs^{138} nucleus in Chapter IV.

1.2 Survey of Previous Work

A certain proportion of experimental data available at the present time on low-energy nuclear structure stems from the discovery by Hahn and Strassman of nuclear fission in 1939. The fission process produces a variety of neutron-rich isotopes which, through subsequent beta-emissions, decay to more stable configurations.

Many of the fission-products are far removed from the line of stability and are therefore difficult to produce from other reactions. From the parabolic mass dependence which is typical of isobaric nuclide chains, it is evident that such nuclides will exhibit high Q-values and correspondingly short half-lives. However in the case of even-A nuclei, from the increased binding due to the pairing effect, the even-even isobars lie on a mass parabola somewhat below the mass

parabola for corresponding odd-odd isobars. Therefore the Q-value for the beta-decay of an even-even parent nucleus is often considerably less than the Q-value for the daughter nucleus decay.

The great variety of isotopes available from fission is a disadvantage from the point of view that it is necessary to chemically separate the desired element from the gross fission products before any detailed analysis of the characteristic radiations may be carried out. The fission-product rare gases xenon and krypton are perhaps the most easily obtainable fission products and were therefore among the first to be studied. Hahn and Strassman (20) first reported the existence of a xenon isotope which decayed to form a 32 minute cesium daughter activity. Glasoe and Steigman (21), by an indirect measurement, found a half-life of 17 $\pm$ 1 minutes for this xenon isotope. A mass assignment of 138 was established by Thulin et al (22) for this isobaric decay chain. A recent mass-spectrometric determination by Clarke and Thode (23) yielded a value of 14.0 $\pm$ 0.2 minutes for the Xe^{138} half-life. This compares with a value of 14.5 $\pm$ 0.5 minutes reported by Hermann and Patzelt (24). Few measurements of the Xe^{138} radiations have been reported. The only result reported thus far on the Xe^{138} beta radiations was an absorption measurement by Nassiff and Seeleman-Eggebert (25) which gave an end-point of 2.4 MeV. Sodium-iodide detector measurements of the Xe^{138} gamma-ray spectrum have been carried out by Thulin (26) and Ockenden and Tomlinson (27) and by Ovechkin and Demidovich (28). Their results are compared in Table II.

Ovechkin and Demidovich estimate the multipolarities of the

0.16 and 0.26 MeV transitions to be M1 and E2 respectively. These authors have also proposed a decay scheme, based on energy and intensity measurements alone, for which the salient features are shown in Table II.

TABLE II

Xe^{138} Gamma Measurements

γ Ray Energy (keV)	Intensity		
	Ref.(26)	Ref.(27)	Ref.(28)
30 (x-ray)			5
160		33	14
260		100	100
420	100	40	63
510	20	8	-
1780		66	44
2020		58	30

Xe^{138} Level Scheme According to Ovechkin and Demidovich (28)

Level (keV)	β Population (%)	Decays by γ's (keV)
2000	27	2000, 1780
420	30	420, 160
260	15	260
0	28	-

CHAPTER II

APPARATUS AND TECHNIQUES USED IN THE PREPARATION OF FISSION-PRODUCT RARE GAS SOURCES

2.1 Source Material

The desirability of a fissionable material as a source for fission-product gases is directly related to the emanating power of the material. The term "emanation" has been applied to the radioactive rare gases and their escape from the substances in which they are formed by radioactive decay (such as radon gas formed in thorium ores, etc.) Quantitatively the term "emanating power" of a substance is defined as the fraction of the radioactive inert gas which escapes from the substance before radioactive decay occurs. The emanating power of a material depends upon the composition, crystal structure, specific surface and temperature of the solid as well as the half-life and recoil formation energy of the rare gas atom.

During the initial stages of the present work with the fission-gas isotopes, enriched (94% U^{235}) uranium stearate was used as the fission-gas source. This selection was based upon information according to Wahl (29) that certain long-chain organic salts such as barium stearate and barium palmitate exhibit a high emanating power. Problems soon arose with this source material when an increasing number of long irradiations were required since in this circumstance the sample was found to disintegrate rapidly with a consequent reduction in emanating power. Wahl et al (30) state that

decomposition of a similar uranyl stearate fission-gas source became noticeable following a thermal neutron flux exposure giving a total of 1.5×10^{12} fissions in the source. The present work therefore required that a fission-gas emanator be found which was more resistant to radiation damage. The final selection of the emanating compound to be used was based on the following criteria:

i) good emanating efficiency

ii) high resistance to radiation damage

iii) a minimum of any long-lived activities which could be formed by (n,γ) reactions in the compound

iv) ability to retain emanating power in the dry helium atmosphere of the gas sweeping apparatus.

The compounds which were tested for fission-gas emanating power are listed in Table III.

TABLE III

Emanating Efficiencies of Selected Compounds for Fission-Product Kr^{88}

No.	Compound	Emanating Power (%)
1	$UO_2(OH)_2$	76
2	Silica gel co-precipitate	81
3	Hydrous Zirconium Oxide	95
4	Zirconium tungstate gel	38
5	Ammonium molybdophosphate	67
6	Zirconium molybdate gel	40

Compound No. 1 was prepared by precipitation of 2 ml. of $UO_2(NO_3)_2$ solution (25 mg. natural U/ml.) with an excess of NH_4OH. Compound No. 2 was prepared by co-precipitation of the uranyl nitrate

in an acid solution together with silica gel. Compounds 3 to 6 are inorganic ion-exchange crystals* which have been developed commercially for use in the processing of spent nuclear reactor fuels. These materials should therefore exhibit a high resistance to radiation damage. Emanating samples of these compounds were prepared in each case by adsorption of uranyl ions from a uranyl nitrate solution kept at a pH of 3. Small samples of each compound were then tested for emanating power in the following manner. The sample was placed in a short length of 1/4" polyethylene tubing which was then closed at each end with hypodermic stoppers. The sample was irradiated for two minutes in the McMaster reactor rabbit. After a 15 minute waiting period, the sample carrier was connected to the helium gas flow apparatus by means of hypodermic connectors. The fission-product gases were swept by the helium flow from the sample into a charcoal cold trap. The counting rate of Kr^{88} in the trap was determined after a period of 15 hours. The relative amounts of uranium in each sample were determined by chemically separating and counting the Pd^{109} fission product activity from the sample. The emanating efficiencies given in Table III are normalized to the emanating efficiency of compound No. 3, hydrous zirconium oxide. An absolute emanating power of $95 \pm 5\%$ was obtained for Xe^{140} emanation from this material in an experiment which is described below. The assumption has been made that the emanating power of this material is the same for both Xe^{140}

* Available from Bio-Rad Research Laboratories, Richmond, Calif.

and Kr^{88}.

The Emanating Power of Hydrous Zirconium Oxide for Xe^{140}

The emanating sample of hydrous zirconium oxide crystals was made by dissolving 1 mg. of enriched (9% U^{235}) uranyl nitrate in 10 ml of water. The pH of the solution was adjusted to a value of 3 by adding NH_4OH. 50 mgs of the exchange crystals were added to the solution which was then heated almost to boiling. The pH of the solution was increased gradually to a value of 5 while stirring. After stirring for half an hour the mixture was centrifuged and the supernatant liquid discarded. The compound was then dried at 110°C.

For the emanating-power experiment, the sample was wrapped in a cylinder of filter paper with a thickness of 15 mg/cm^2 which is greater than the fission-product recoil range in this material. During the irradiation the sample was supported in the centre of an evacuated quartz glass container 20 cm long and 3 cm in diameter. The sample was irradiated for 120 seconds, giving a total of 5 x 10^{11} uranium fissions in the emanating material. After a cooling period of 30 minutes the sample was removed from the container. The barium fission-product activity was then separated chemically from the sample. The tube walls were flushed with HNO_3 and the barium activity separated from the solution. The 40 hour La^{140} activity was allowed to grow in for several days from the decay of the 12.8 day Ba^{140} parent activity in both fractions. The ratio of Ba^{140} collected on the container walls as compared with the Ba^{140} separated from the source was then determined by counting the respective La^{140} activities. Wahl et al (30) refer to this ratio as $G(Ba^{140})$. They obtain a value of

0.79 ± 0.01 for this ratio for a uranyl stearate emanator. The stearate was assumed to have an emanating power of 100% for Xe^{140}. The value obtained for $G(Ba^{140})$ in the present experiment was 0.75 ± 0.05 which would then correspond to an emanating power of 95% for the hydrous zirconium oxide crystals.

The Effects of Radiation on the Emanating Power of Hydrous Zirconium Oxide

Time did not permit the testing of materials other than the hydrous zirconium oxide emanator for the effects of radiation on the emanating power of the material. Since the hydrous zirconium oxide seemed to be the most promising emanator, it was of interest to study the ability of this compound to retain its emanating efficiency under irradiation.

The sample was placed in the standard gas-sweeping equipment (described in section 2.2) and irradiations were carried out in a thermal neutron flux of approximately 10^{13} $n/cm^2/sec$. Irradiations of this sample of less than ten minutes duration were carried out at frequent intervals over a period of several months. From time to time during this period the change in emanating power of the sample was monitored as follows. The sample was irradiated for 20 seconds and the fission gases released were swept from the sample by dry helium carrier gas and trapped. The over-all activity of the fission-gases released per unit irradiation time was determined by monitoring the emanated gas activity. The results of these quantitative measurements are plotted as a function of sample irradiation in Figure 2. It may be seen that the emanating power of this material varies exponentially with the radiation exposure. The "mean lifetime" of

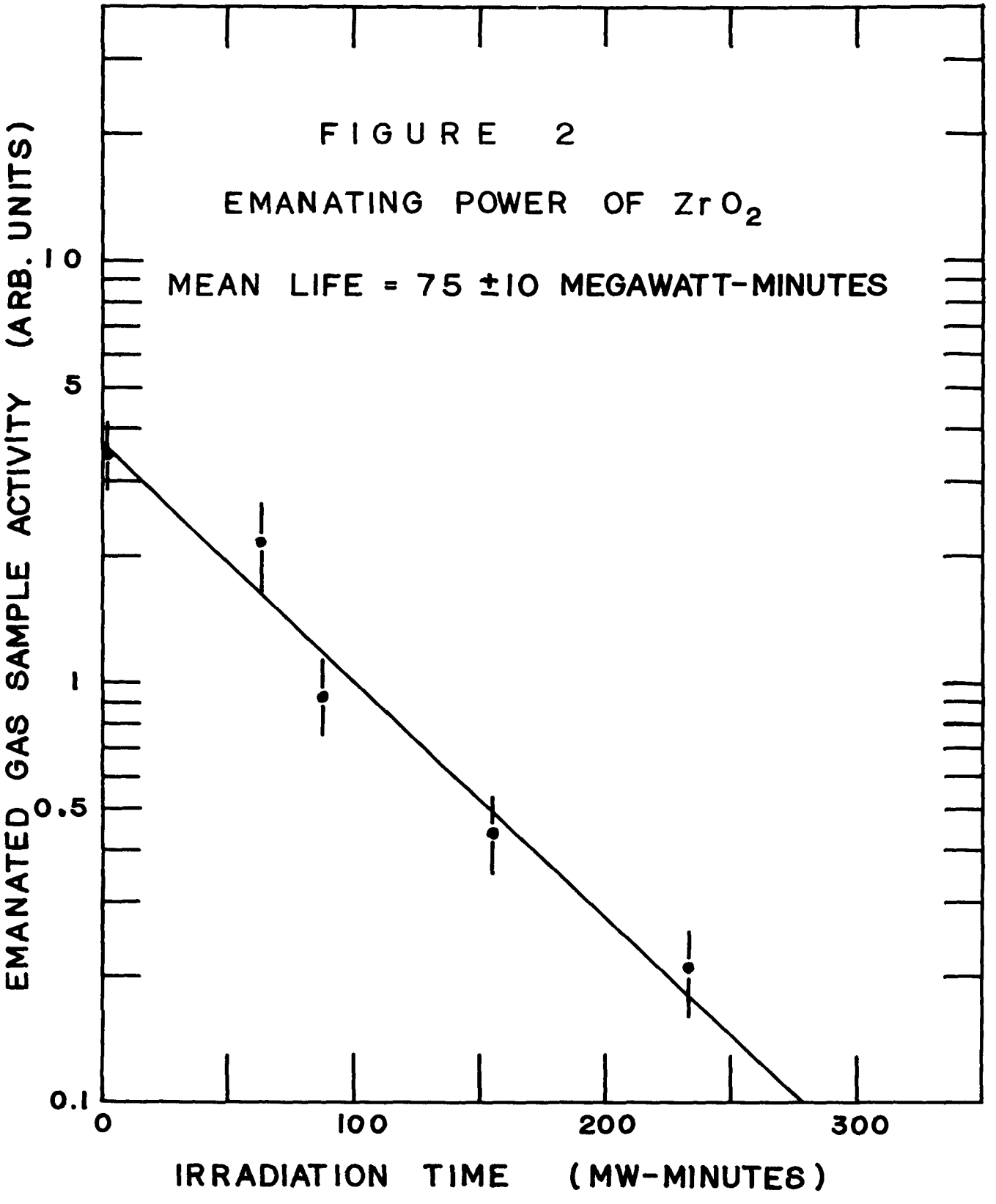
FIGURE 2
EMANATING POWER OF ZrO_2
MEAN LIFE = 75 ±10 MEGAWATT-MINUTES
EMANATED GAS SAMPLE ACTIVITY (ARB. UNITS)
10
5
1
0.5
0.1
0
100
200
300
IRRADIATION TIME (MW-MINUTES)

the emanating power of the source under these experimental conditions is 75 $\pm$ 10 megawatt-minutes. When exposed to the same reactor flux the "mean lifetime" of enriched uranium stearate (if it is possible to define such a quantity for the stearate) was estimated to be less than ten megawatt minutes.

The various arguments given above indicate that hydrous zirconium oxide has the highest emanating power of the compounds tested and that this material retained its emanating property over moderate irradiation periods. In addition zirconium also has the desirable property of a low neutron capture cross-section, and hence this compound was chosen for use as the fission-product gas emanator in the gas-sweeping facility.

2.2 The Gas-Sweeping Apparatus

The fission-product gases are considerably more amenable to separation from the gross fission-product activity than are the other fission-products since the removal of these gases from an emanating fission source may be accomplished simply by flowing a stream of carrier gas through the source. Injection of the carrier gas may be carried out easily from a location remote from the fissile material, thus avoiding exposure of the experimenter to the greater than 80% of fission-product radiation which does not originate from the fission-gas activity. The gas-sweeping facility used in this work was mounted semi-permanently in a core grid position of the McMaster reactor. The reactor pool water provided an adequate biological shield from the source which was located in the lower end of the facility.

A pictorial lay-out of the apparatus is shown in Figure 3.

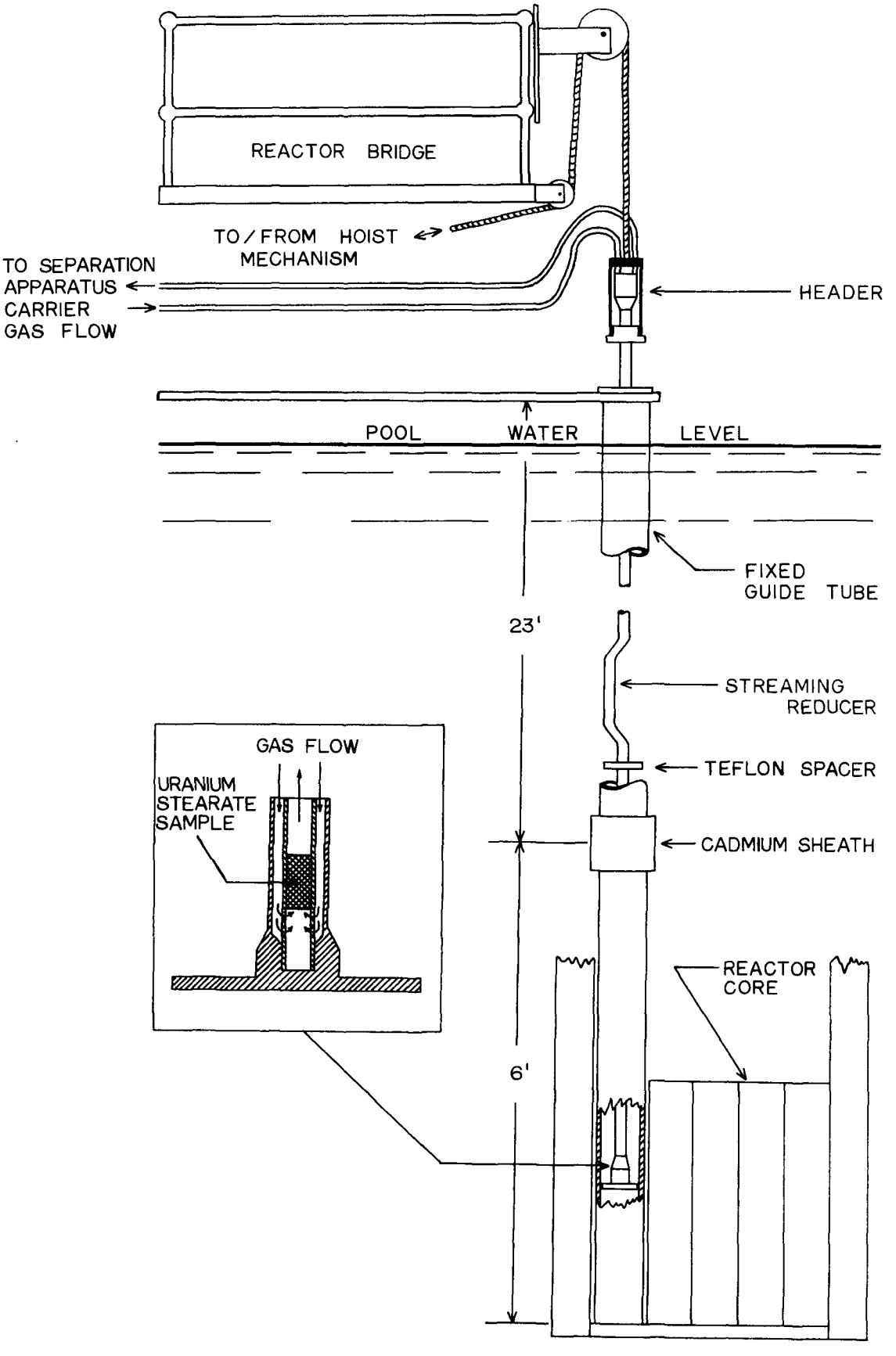

FIGURE 3

IRRADIATION APPARATUS

A 2-3/4" I.D. guide tube extends from the reactor grid position to the upper support which is fastened to the reactor control rod drive plate. A double-walled aluminum tube which forms the source carrier is free to travel vertically in the guide tube. The outer wall of the carrier is 3/4" aluminum tubing. The inner wall in the upper section of the carrier is 1/8" polyethylene tubing; the lower five feet of the inner wall is 1/4" aluminum tubing because of possible radiation damage to polyethylene in the reactor flux region. The over-all length of the carrier is 26 feet. Near the lower end it is bent in order to prevent neutron streaming. The carrier is supported in position by 1/16" aircraft cable which is wound on a motor driven drum.

The source is mounted in the lower extremity of the inner tube of the carrier. Holes in the tube wall directly below the source allow sweeping gas which is forced down the annular space to flow through the source and up through the header which is welded to the top of the carrier. Further sweeping-gas connections to the separation apparatus which is situated beside the reactor pool are made with polyethylene tubing and quick-disconnect couplings.

When the carrier is in the "up" position, the fission-gas source is at a location six feet above the reactor grid plate, well out of the reactor flux. When the source is at this location it is also shielded by a cadmium sheath which is wrapped around the guide tube and serves as a neutron absorber. The carrier "down" position may be adjusted so that the source may be irradiated in any desired neutron flux up to the maximum available in that grid position (approx-

imately 10^{13} n/cm^2/sec.). The irradiation cycle, since it is controlled by limit switches and a timer, is completely automatic, although the length of the irradiation may be manually controlled. Switching and drive mechanisms for the carrier are mounted on the reactor bridge.

The carrier is inserted into the flux region by means of a gravity drop. Near the desired irradiation location a magnetic brake is turned on to slow the speed of the carrier fall. The carrier is finally stopped at the irradiation position by means of a solenoid-operated clutch. When the irradiation period has elapsed the carrier is withdrawn to the "up" position by the motor-driven cable hoist. The total time of either insertion or withdrawal is approximately 4 seconds.

2.3 The Separation of Trace Quantities of Xenon and Krypton

By means of an emanating fission-gas source placed in the gas-sweeping facility it is possible to obtain sources of the fission-gases diluted in a suitable carrier gas. Separation of the xenon or the krypton fraction from the rare-gas mixture is the only sample preparation problem remaining before accurate measurements may be made on the radiations from these isotopes.

Classical distillation methods such as those described in a review by Momyer (31) for rare-gas separations are rather slow and cumbersome. Added to this is the complication that xenon and/or krypton carrier must be added to the trace quantities of these rare gases in order to circumvent the vagaries of trace-gas behaviour of larger quantities of these gases.

Gas chromatographic methods have proven to be very effective in the separation of trace quantities of these gases. The tracer mixture is usually swept through the chromatographic column by a light rare-gas carrier such as helium. Introduction of the mixture into the column is accomplished in the form of a short burst of the mixture into the flowing carrier stream. The lighter trace gas, krypton, emerges from the column in a short, well defined band followed at a later time by the xenon fraction which is dispersed into a much broader band. Koch and Grandy (32) used a charcoal column at room temperature to effect a good xenon-krypton separation in a few tens of minutes. Ockenden and Tomlinson (27) also used a charcoal column at room temperature in which the charcoal was dispersed as a fine powder on the surface of glass wool. They obtained xenon-krypton separation in a matter of ten to fifteen seconds.

The technique developed for the present work is essentially a low-temperature gas chromatrographic technique. In the production of contamination-free fractions of either of the fission-product gases, a small burst of xenon and krypton fission-product tracer in helium carrier gas is swept through a clean, empty length of tubing which is refrigerated in a low temperature coolant. The temperature of the coolant may vary from $90^{\circ}K$ (liquid oxygen) to $77^{\circ}K$ (liquid nitrogen). Table IV lists approximate vapor pressures of both xenon and krypton at these temperatures. It is obvious that the temperatures involved are much below the temperature at which chemically measurable quantities of these gases would condense.

TABLE IV

Vapor Pressures of Xenon and Krypton

Rare Gas	Temperature (^{o}K)	Vapor Pressure (mmHg)
Xenon	165	760
	105	1
	90	.06
	77	.0004
Krypton	121	760
	90	20
	77	2
	74	1

The tubing which is normally used is 6 millimetre I.D. pyrex glass. The length of tubing which makes up the column may be varied, depending on the separation desired, but a length of 50 centimetres was found to be sufficient in most cases. If the column is held at liquid oxygen temperature, essentially no xenon-krypton separation is effected in such a short column. At the temperature of freshly prepared liquid air a typical chromatographic xenon-krypton separation is obtained; the krypton fraction emerges from the column after a short time in a sharply peaked distribution and, after a further time interval the xenon fraction follows, but in a much broader distribution. An example of a typical separation is shown in Figure 4, where the counting rate at the exhaust end of the column is plotted as a function of time. Furthermore, if the separation process

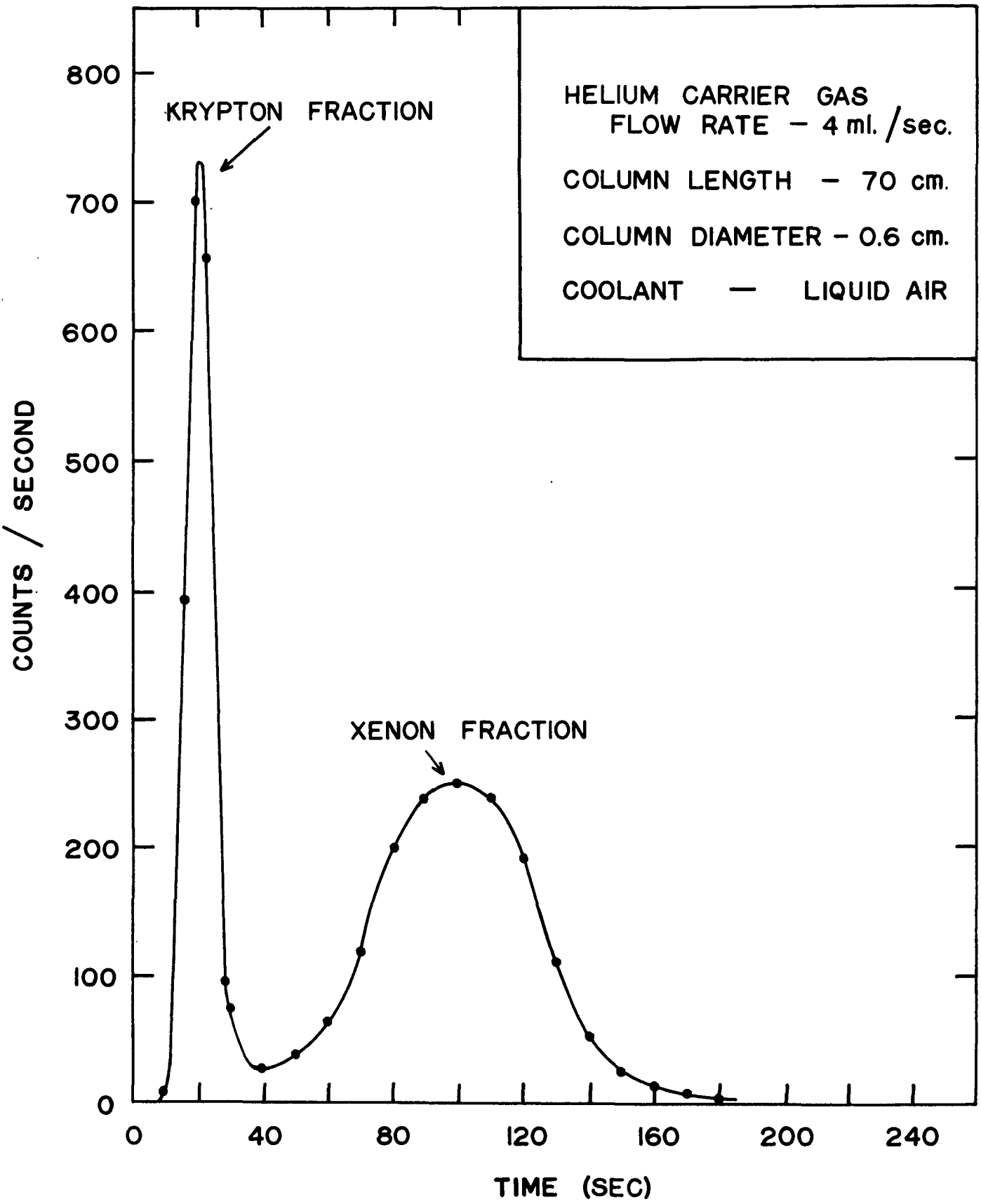

FISSION-GAS ELUTION CURVE

FIGURE 4

is carried out at liquid nitrogen temperatures, the delay in emergence of the krypton fraction is approximately the same as before. However, the xenon fraction remains in the column almost indefinitely.

The separation process was also carried out using columns of metals such as copper or aluminum. The chromatographic separation in this case seemed to occur at slightly higher temperatures. This is thought to be due to the higher conductivity of the metals used as opposed to pyrex glass; this would, under the dynamic conditions of the experiment, bring the inner walls of the metal tubing to a temperature closer to that of the coolant than would the pyrex glass tubing.

One advantage which this technique has over standard chromatographic methods lies in the very effective control that may be exercised on the speed of the separation process. For example, one may wish to effect a clean separation in a very few seconds. Normally, increasing the carrier gas flow rate would smear the two tracer functions into one another, causing contamination of both gas fractions. With this technique however, and operating at liquid nitrogen temperatures, the flow rate may be varied over a wide range without greatly affecting the quality of the separation.

The xenon fraction may be removed from the column after the emergence of the krypton fraction simply by removing the coolant from the column. In room atmosphere the column very quickly rises in temperature the few degrees necessary to completely release the xenon from the column walls. It has been found through experience,

that this condensation-type separation is preferable to a chromatographic separation at slightly higher temperatures, since faster and cleaner separations are obtained.

To reduce the possible contamination of the xenon fraction by any remaining krypton during the preparation of xenon samples, two of the condensation-type separations have been performed in series. In this case the krypton fraction emerging from the first column is vented to exhaust. The xenon fraction may then be brought out by removing the coolant, and diverted into a second column where the separation process is repeated. A diagram for a flow system for a double series-type separation appears in Figure 5. Double separations have been performed at speeds at which the xenon fraction was released from the second column 30 seconds after the entry of the rare gas mixture into the first column.

By a comparison of the activity in the krypton fraction emerging from column number two to that emerging from column one, an estimate has been obtained of possible krypton contamination in the xenon fraction. When operating at moderate flow rates it has been impossible to detect krypton activity emerging from the second column which was greater than the general background. The ratio of krypton activity emerging from column one as compared to background activity was approximately 300:1. This indicates that krypton contamination in the xenon fraction after a double separation would be less than $10^{-3}\%$ of the original krypton in the mixture. Similar arguments would be valid for series-type purifications of the krypton fraction.

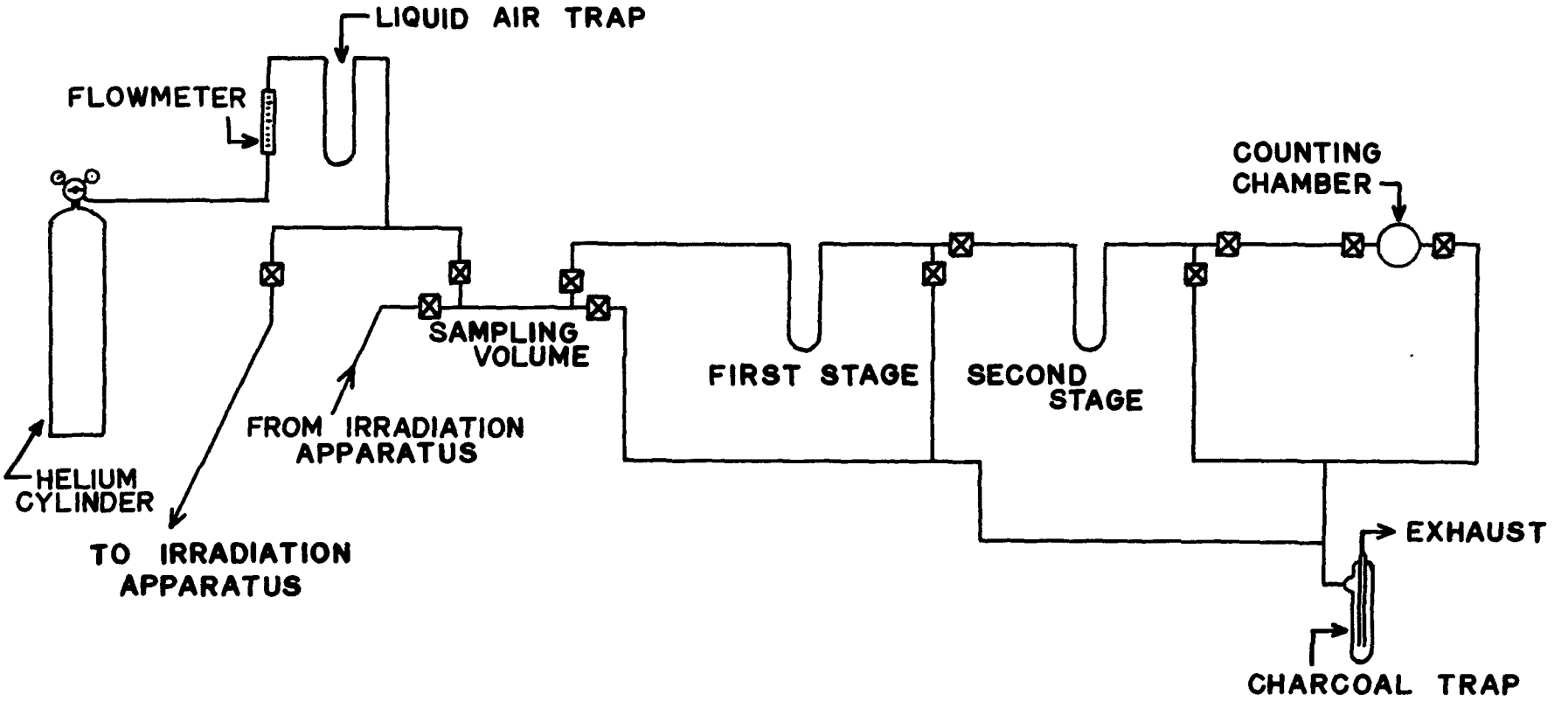

RARE-GAS SEPARATION APPARATUS

FIGURE 5

The Properties of Trace Quantities of the Rare Gases

It is well known that in chemical reactions of many kinds trace quantities of any element may behave in a differing and often an erratic manner from larger quantities of the same element in a similar environment. This statement is true when applied to adsorption processes involving the rare gases. The method described above for the separation of the rare gases depends entirely upon the behaviour of microscopic quantities of these gases. The technique would therefore not be applicable to separation of larger quantities of the gases.

Quantities of xenon or krypton which have been separated by this technique have been no greater than 10^{11} atoms/ml when diluted in the helium carrier gas. The helium carrier gas was passed through a liquid air trap before introduction into the gas flow apparatus. There should therefore be no contribution from natural xenon or krypton in the carrier. The rare gas fission-products in the mixture should give rise to partial pressures of the order of 10^{-5} mm of mercury. It may be seen from Table IV that these pressures are well below the actual vapor pressures which would exist above solid xenon or krypton at the temperatures of the separation column. There is no possibility of actual condensation of the tracer gases under these conditions. The process must therefore be dependent upon the chemical phenomenom of adsorption. The chromatographic separations of xenon and krypton carried out in charcoal columns (references (32) and (27)) also depend upon adsorption, but at a relatively much higher temperature. The relationship between these processes and the present technique is shown in the following paragraphs.

The practicability of separating any two gases by the gas chromatographic technique is dependent upon (a) the ratio of surface to volume of the column adsorbent and (b) the temperature of the system. The dependence on these quantities is due to the fact that the impinging of a molecule of gas on the adsorbent surface (provided the surface is not covered by a mono-molecular layer of that gas) may be considered a condensation-evaporation process. The probability of evaporation of the molecule following 'condensation' is an exponential function of time. Loeb (33) refers to the average dwell time of the molecule on the surface as the "verweilzeit"(delay time). The verweilzeit at a given temperature for a particular surface will vary for different types of gases. Since the rare gas atoms have closed-shell structures, the verweilzeit at a given temperature will mainly be dependent upon the atomic weight, being longest for radon, followed by xenon, krypton, argon, neon and helium in that order. The verweilzeit will also be a strong function of temperature. The number of times a molecule strikes the adsorbing surface in passing through a column is dependent upon the surface-to-volume ratio. The average time of hold-up of molecules of a trace quantity of gas in passing through a chromatographic column will therefore be dependent to a great extent upon the product of:

(i) The ratio of total adsorbing surface area to the column volume and

(ii) The verweilzeit of the particular kind of molecule on the adsorbing surface at that particular temperature.

As contrasted to a charcoal chromatographic column at room temperature which has a very large surface-to-volume ratio and a very small verweilzeit, the new technique involves a very small surface/volume ratio which is balanced by an extremely large verweilzeit due to the very low temperature of the column. The new technique is expected to give much cleaner rare-gas fractions than packed-column separations because of the absence of complicating factors (such as 'eddy diffusion' as described by Keulemans (34)) which give rise to contamination due to "tailing" in packed chromatographic columns.

2.4 The Travelling Charged-Wire Counting Chamber

Many of the short-lived fission-gas isotopes have radioactive progeny with half-lives of the same order of magnitude as the parent gas isotope. In studying the decay of the gaseous nuclide, the amount of activity resulting from the growing-in of such descendants will be found to vary considerably throughout the length of the experiment. Indeed, if the daughter isotope has a half-life which is greater than that of the parent isotope, then equilibrium will not be attained between the two decay rates. This is the case with 14.0 minute Xe^{138} which has a shorter half-life than the 32 minute Cs^{138} daughter isotope. Corrections are therefore very difficult to make in accounting for the contaminating activity.

The solution which was desired for this problem was to remove continuously the contaminating activity from the counting-chamber volume.

Snell and Pleasonton (35) have shown that the beta-decay of

the xenon isotope, Xe^{133}, may leave the Cs^{133} daughter atom in any one of a number of ionized states which have charges ranging up to a maximum of + 22. Since beta-decay of any atom will always leave the daughter atom with a minimum charge of + 1, the ion may be attracted to a collecting surface by means of an electro-static field. The existence of more highly charged states tends to enhance the mobility of these particular ions in a field.

In the present work, care was taken that the helium carrier used in the manipulation of the xenon tracer was dry and clean. This would tend to increase the lifetime of ions produced by beta-decay in the gas by decreasing the possibility of chemical combination with contaminating gases such as oxygen. The likelihood of being able to collect the ion on a negatively charged electrode would thus be increased.

Nassiff and Seelman-Eggebert (36) used a static charge-precipitation method to remove Cs^{138} from the gaseous mixtures of Xe^{137} and Xe^{138} in order to determine the beta-energies of the gas nuclides. This was accomplished by placing the negative electrode in such a position that the beta-ray detector was shielded from the ensuing beta-radiation of the Cs^{138} atoms which were attracted to the electrode. For the study of gas nuclide gamma-radiations, such a system is not adequate, as the difficulties of shielding gamma-ray detectors from the contaminating radiation are much greater. Furthermore, the back-scattering and annihilation contributions which tend to degrade the quality of gamma-ray spectra are amplified by the presence of any quantity of heavy shielding.

The apparatus which was used in the present investigation utilizes a charged wire as the negative electrode. The wire is continuously drawn through the radio-active gas sample, thereby removing the daughter isotopes which are attracted to the wire to a remote location which is well shielded from the radiation detectors. The wire is 0.030 inch tinned copper. The wire speed may be varied, by gearing of the winding motor, from a speed of four feet per minute to a maximum of thirteen feet per minute.

Two models of the counting chamber were constructed. For the first model, since it was to be used in half-life measurements, special precautions were taken to avoid chamber leakage, a small amount of which would have a strong effect on the half-life results. Special differential pressure seals were used where the wire travels through the chamber walls. The counting chamber is a brass cylinder two inches long, with an inside diameter of three inches. The chamber windows are 0.001 inch brass sheet. Welded to both sides of the chamber are cylindrical arms eight inches in length with inside diameter one-half inch. The travelling wire enters and leaves the chamber through the differential pressure seals in the outer extremities of these arms. Therefore, no contact between wire and chamber is made within 9-1/2 inches of the centre of the counting chamber. The detectors are easily shielded from the fraction of radioactive material which is deposited on the seal as the wire leaves the chamber. The wire is at ground potential while the chamber is maintained at a positive voltage. A plot of the chamber efficiency, as a function of applied voltage, for removing xenon daughter isotope contamination is

shown in Figure 6. The chamber efficiency is defined to be:

$$\frac{R_{12} - R_2}{R_{12}} \times 100\ (\%)$$

Here, R_{12} = total daughter activity collected on both the chamber walls and the charged wire. R_2 = daughter activity collected on the chamber walls.

A second model of the charged-wire chamber was designed and constructed for the present work by Mr. L. V. Johnson (37). This model is of much lighter construction and has a much smaller active gas volume than the initial model. Single seals of neoprene rubber which are leak-proof to a good degree are used at the chamber wire entrance and exit. The chamber is constructed as a tube, 2 inches long by 1/2-inch diameter, with .001 inch brass walls. The total volume is 1/3 cubic inches. The chamber is mounted vertically so that detectors may be positioned at any desired location in a horizontal plane about the source. The radio-active gas source is introduced by means of a hypodermic needle through a rubber stopper in the gas inlet. The general layout of the chamber and detectors is shown in Figure 7. The efficiency characteristics of this chamber for the removal of xenon daughter isotopes from the decaying gas are remarkably similar to the characteristics of the original model.

This chamber, since it is smaller, is much closer to the point source approximation usually used for calculation of gamma-ray intensities in NaI(Tℓ) detectors. Also, the absence of much heavy shielding material near the chamber diminishes gamma-ray back-scattering problems. This model was therefore used for all the gamma-and beta-ray spectro-

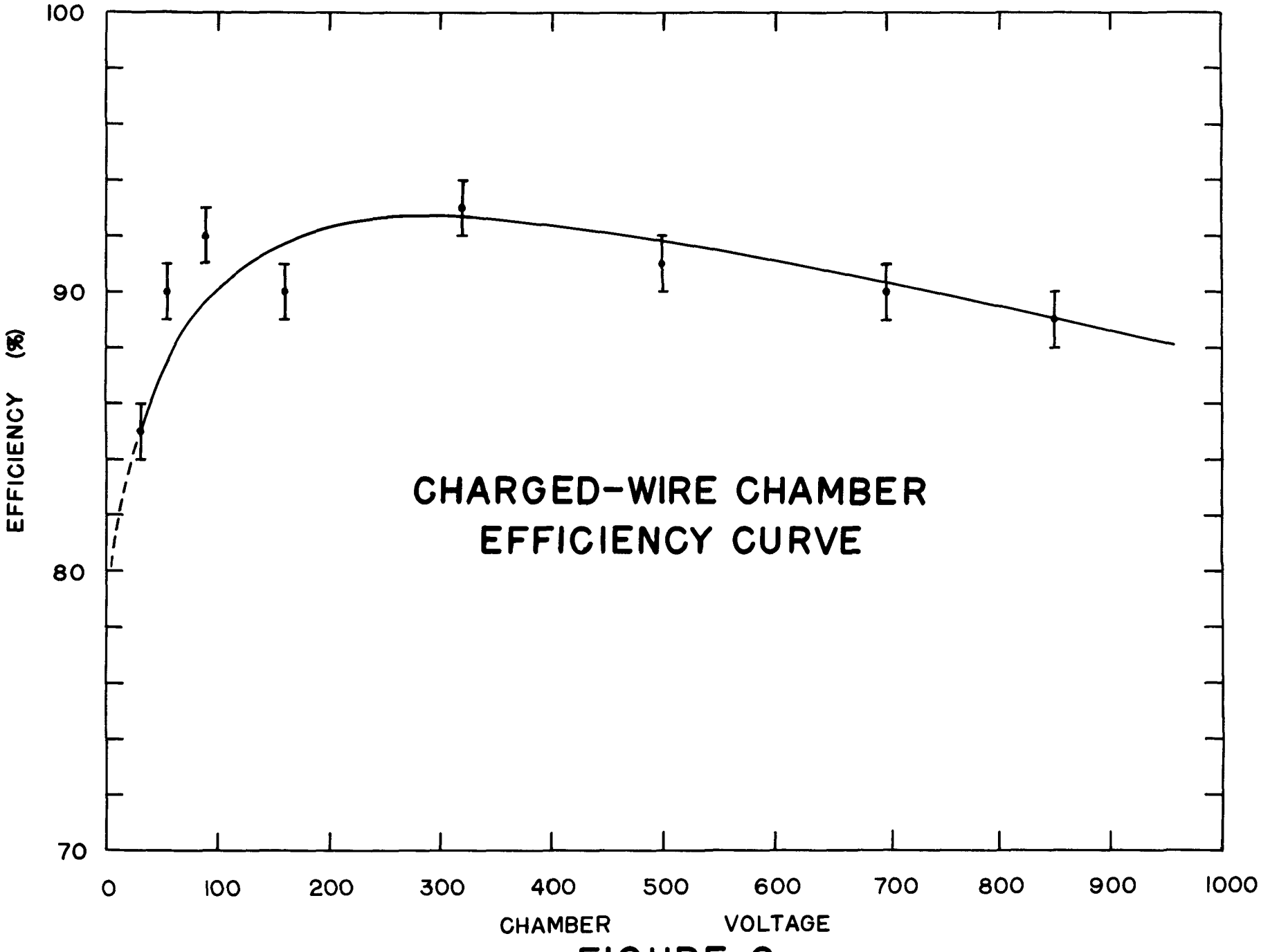
100
90
80
70
EFFICIENCY (%)
0
100
200
300
400
500
600
700
800
900
1000
CHAMBER VOLTAGE
CHARGED-WIRE CHAMBER
EFFICIENCY CURVE

FIGURE 6

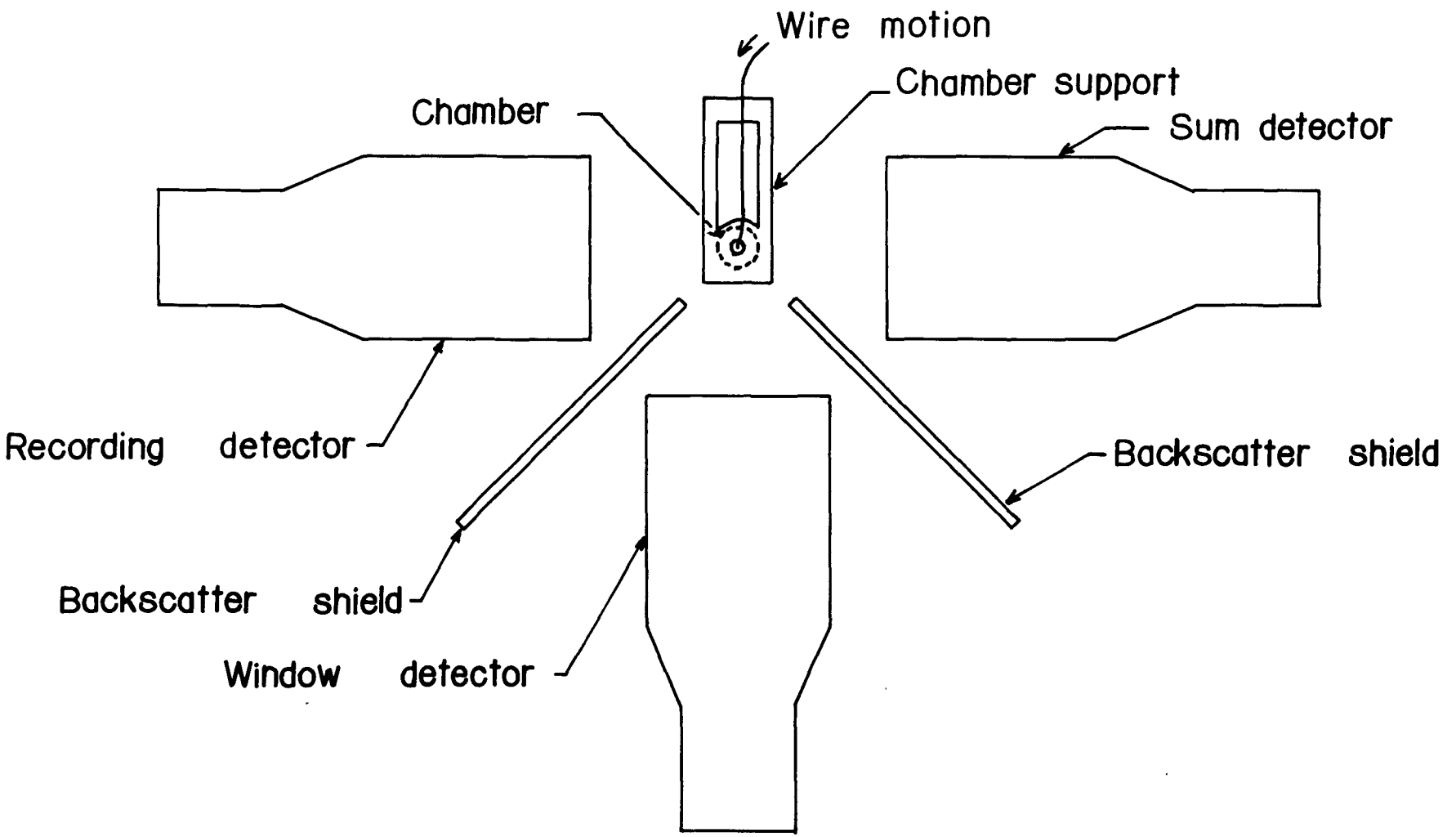

FIGURE 7.

PLAN VIEW OF CHARGED-WIRE CHAMBER AND DETECTORS.

scopy measurements. For the study of beta-radiation a window of 0.25 mil mylar metallized on one side with gold was used on the counting chamber.

2.5 Transportation of Rare Gas Samples to the Counting Apparatus

The placement of the pulse height analyzing system, to be described in Chapter III, was such that no direct connections could be made from the gas separation apparatus to the counting chamber. Therefore a simple means of transferring the xenon samples to the counting chamber was required.

The gas holder is an eight-inch coil of 1/8" O.D. copper tubing. On each end is fitted a rubber hypodermic stopper. Connection is made to the gas separation apparatus by means of hypodermic needles. The copper coil is cooled quickly in a liquid air bath. Before the rubber seals begin to freeze, the xenon source is flushed into the coil where it condenses on the walls. The hypodermic needles are then withdrawn and the coil removed from the bath. The sample may then easily be transferred to the counting location for introduction into the counting chamber.

2.6 Preparation of Xe^{138} Samples

In the preparation of xenon samples for the study of the decay properties of Xe^{138} it is necessary to ensure that there is a minimum of other contaminating species. The removal of the krypton fraction from the fission-gas mixture and the continuous removal of daughter isotopes from the decaying gaseous isotopes have been discussed. However, there is a variety of xenon isotopes produced in fission, which, of course, may not be separated chemically from the desired Xe^{138} activity.

It is possible to discriminate against the xenon isotopes which contaminate the sample by selecting the optimum irradiation time as well as by allowing the sample to decay an optimum time before beginning the analysis. The isobaric decay chains which provide a reference in the preparation of Xe^{138} samples are listed in Table V.

TABLE V

Xenon Decay Chains

$$I^{140} \xrightarrow[\beta^-]{\text{Short}} Xe^{140} \xrightarrow[\beta^-]{13.7\ \text{sec}} Cs^{140} \xrightarrow[\beta^-]{63.6\ \text{sec}} Ba^{140} \xrightarrow[\beta^-]{12.8\ \text{day}} La^{140}$$

$$I^{139} \xrightarrow[\beta^-]{2.7\ \text{sec}} Xe^{139} \xrightarrow[\beta^-]{41.2\ \text{sec}} Cs^{139} \xrightarrow[\beta^-]{9.05\ \text{min}} Ba^{139} \xrightarrow[\beta^-]{83\ \text{mins.}} La^{139}$$

$$I^{138} \xrightarrow[\beta^-]{6\ \text{sec}} Xe^{138} \xrightarrow[\beta^-]{13.9\ \text{min}} Cs^{138} \xrightarrow[\beta^-]{32.3\ \text{min}} Ba^{138}$$

$$I^{137} \xrightarrow[\beta^-]{24.4\ \text{sec}} Xe^{137} \xrightarrow[\beta^-]{3.82\ \text{min}} Cs^{137} \xrightarrow[\beta^-]{30\ \text{yr.}} Ba^{137}$$

$$I^{135} \xrightarrow{6.7\ \text{hr}} \begin{cases} \xrightarrow[\beta^-]{30\%} Xe^{135*} \\ \xrightarrow[\beta^-]{70\%} Xe^{135} \end{cases} \qquad Xe^{135*} \xrightarrow{\gamma\ 15.3\ \text{min}} Xe^{135} \xrightarrow[\beta^-]{9.13\ \text{hr}} Cs^{135}$$

The following procedure was used to prepare the Xe^{138} samples. The fission source was irradiated for the length of time, up to 100 seconds, necessary to produce the desired Xe^{138} activity and then allowed to cool for 10 seconds. At this time the fission-gases were flushed from the source since the most favorable ratio of Xe^{138} activity as compared with longer-lived xenon isotopes has been obtained through the decay of the 6 second I^{138} parent isotope. The xenon-krypton separation was then carried out. The sample was allowed to

cool for 35 minutes to reduce the contamination from Xe^{137} activity to less than 1% of the remaining activity. This cooling time also virtually eliminated through decay the other shorter-lived xenon isotopes. At this time the sample was ready for study.

Due to the low fission-yield of Xe^{135} (primary yield of 0.2%) as compared to the cumulative yield of Xe^{138} (approximately 6%) which was obtained in this manner, and also because of the longer half-life of Xe^{135}, contamination of Xe^{135} in the final sample was approximately 0.005 micro-curies per micro-curie of Xe^{138}.

Very little time was allowed for fission-product iodine to decay to xenon daughter activity before the rare-gases were flushed from the fission-gas source. Therefore it would be expected that contamination in the sample would be small from meta-stable Xe^{135} which would accumulate from the I^{135} decay. However, a greater contribution from Xe^{135*} activity in the sample was found than could be accounted for by the growth from the I^{135} parent. This suggests that Xe^{135*} is formed directly in fission, although this has not previously been confirmed in the literature . The half-life of Xe^{135*} is almost identical to the Xe^{138} half-life; there was therefore no possibility of eliminating this contamination from the Xe^{138} samples. The Xe^{135*} contribution to the spectra obtained is discussed in section 3.3 .

The activities which were used were of the order of 0.5 micro-curies for study of the beta radiations. Activities of the order of 15 uc were used for gamma-gamma coincidence measurements and samples of up to 50 uc were used for solid state detector measurements.

CHAPTER III

MEASUREMENT TECHNIQUES AND EXPERIMENTAL RESULTS

3.1 The Half-Life of Xe^{138}

There has been considerable disagreement among the reported half-lives for Xe^{138} (see Table VI). Previous half-life determinations have been carried out by indirect measurement, except for the results reported by Clarke and Thode (23). Since it was often necessary to make small corrections to the Xe^{138} scintillation spectroscopy measurements due to the in-growth of Cs^{138}, it was essential to have accurate values for the half-lives of these two isotopes. Experiments were therefore undertaken to determine these half-lives, by both direct and indirect measurements, if possible.

3.1.1 Cs^{138} Half-Life Measurements

The Cs^{138} samples were obtained through the decay of the Xe^{138} parent isotope. The fission-gas mixture was produced in a 20 second irradiation. The xenon-krypton separation was carried out and the xenon fraction retained. After a cooling period of 15 minutes, the remaining xenon activity was flushed into a chamber where the cesium daughter activity was collected on a metal foil by "charge precipitation". Following a 15 minute decay period the residual gas activity was flushed out and the cesium sample removed for counting. Contamination by cesium activities other than Cs^{138} was negligible.

The decay-curve was obtained by counting beta radiations in the range 0.5 to 4 MeV with a 2" D. x 2" plastic scintillation detector. The counts were scaled and recorded automatically at

intervals of 200 seconds by means of a Hamner scaler-timer and print-out unit.

A typical Cs^{138} decay curve is shown in Figure 8. The least-squares curve which was fitted to these data is also shown. The decay-curves were analyzed by means of the parabolic method, as discussed in Appendix I, which was programmed in Fortran IV for the 7040 computer. Also shown are the differential residuals. The systematic fluctuations which may be observed in these residuals are believed to be due to background fluctuations in the reactor building, where these measurements were taken.

Since there have been a number of determinations of the Cs^{138} half-life in the past, only two measurements were made in the present work. The mean of these two measurements is compared in Table Vb, with good agreement, to published values for the Cs^{138} half-life.

TABLE Vb

Cs^{138} Half Life Measurements

Researcher	Cs^{138} Half-Life Observed
R. M. Bartholomew (38)	32.2 min.
M. E. Bunker et al (39)	32.1 min.
G. N. Glasoe and J. Steigman (21)	32.0 min.
H. B. Evans et al (40)	32.9 min.
Present work	32.3 min. $\pm$ 0.3

The error suggested for this measurement is only an estimate, since systematic errors in the data would probably overshadow purely statistical deviations.

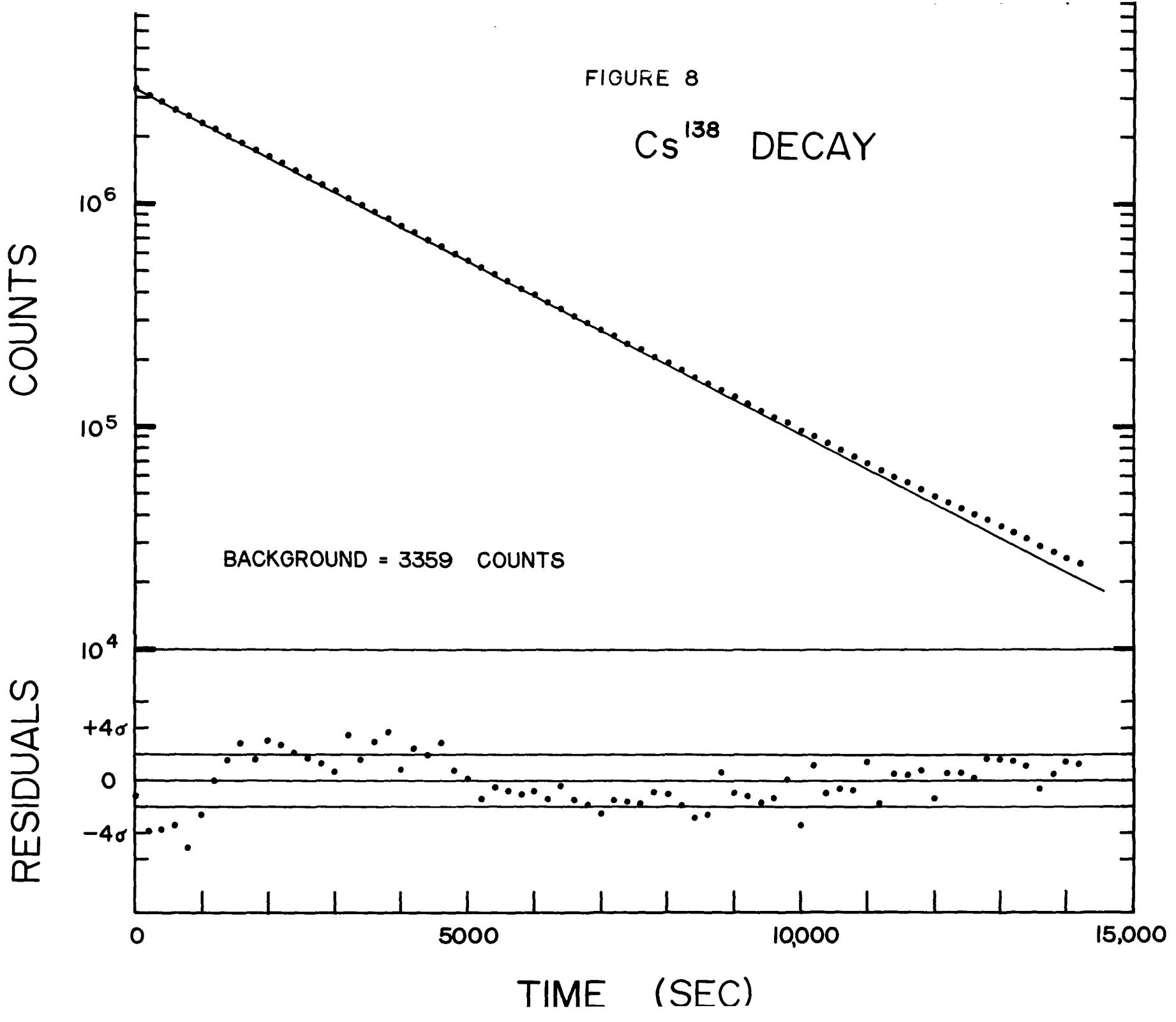
FIGURE 8
Cs 138 DECAY
COUNTS
10^6
10^5
BACKGROUND = 3359 COUNTS
10^4
RESIDUALS
+4σ
0
-4σ
0
5000
10,000
15,000
TIME (SEC)

3.1.2 Xe^{138} Indirect Half-Life Determination

Indirect determinations of the Xe^{138} half-life were carried out in a manner somewhat similar to the method used by Dillard et al (41) in the indirect measurement of the half-lives of the shorter-lived fission-gases. These researchers used a long flow-tube in which a charged wire was stretched longitudinally. After flowing rare-gas fission-products continuously down the tube for some time and collecting the daughter isotopes on the wire, the wire was removed and sectioned. By obtaining the counting-rate contribution of each daughter isotope on the wire as a function of distance from the input end of the tube, values were obtained for the rare-gas parent half-lives.

In the present experiment, the first model of the charged wire chamber (see section 2.4) was used as a containing vessel for the Xe^{138} activity. A beta counter was placed beside the charged wire in a position which was well shielded from the chamber. The rare-gas sample was prepared by a 50 second irradiation. After separating out the krypton fraction, the xenon fraction was allowed to cool only 15 minutes before being flushed into the counting chamber. The sample still contained an appreciable fraction of Xe^{137} activity, but the activity of the Cs^{137} daughter collecting on the wire would be negligible. The wire was allowed to remain stationary for a short period while the Cs^{138} daughter activity from the decay of the parent isotope collected on the wire. The wire was then passed through the chamber and stopped when the radioactive section was directly in front of the counter. A count was recorded of the cesium activity on the wire. At the same time,

more Cs^{138} activity had been collected on the wire which was then within the chamber. This section of wire was also withdrawn and counted. The process of collecting cesium activity on the wire and counting this activity was repeated a number of times at intervals of 200 seconds thereby obtaining a decay curve for the Xe^{138} activity. A check was maintained for sample purity by measuring the gamma-ray spectrum of the residual cesium activity to ensure that only Cs^{138} radiations were present.

A typical decay curve obtained from an indirect half-life determination on Xe^{138} is shown in Figure 9. The results of the measurements are shown in Table VI.

3.1.3 Direct Half-Life Determination on Xe^{138}

The sample preparation procedure for the direct half-life measurements was much the same as before. However, the sample was allowed to decay 35 minutes before injection and counting in the charged-wire chamber. The decay-curve was obtained by measuring the beta activity of the sample from 0.6 to 4.0 MeV by means of a plastic scintillator. The counts were recorded in 100 second increments. With the beta threshold set this high there was no possibility of recording conversion electrons from the 525 keV M4 transition in the 15 minute Xe^{135*} activity. A small back-ground contribution from Xe^{135} was assumed to be a constant for the length of this experiment.

The decay curves were fitted by the parabolic method for the Xe^{138} half-life and the Cs^{138} daughter activity half-life was assigned the value found in the former experiment. A typical decay curve obtained by the direct measurement technique is shown in Figure 10. The

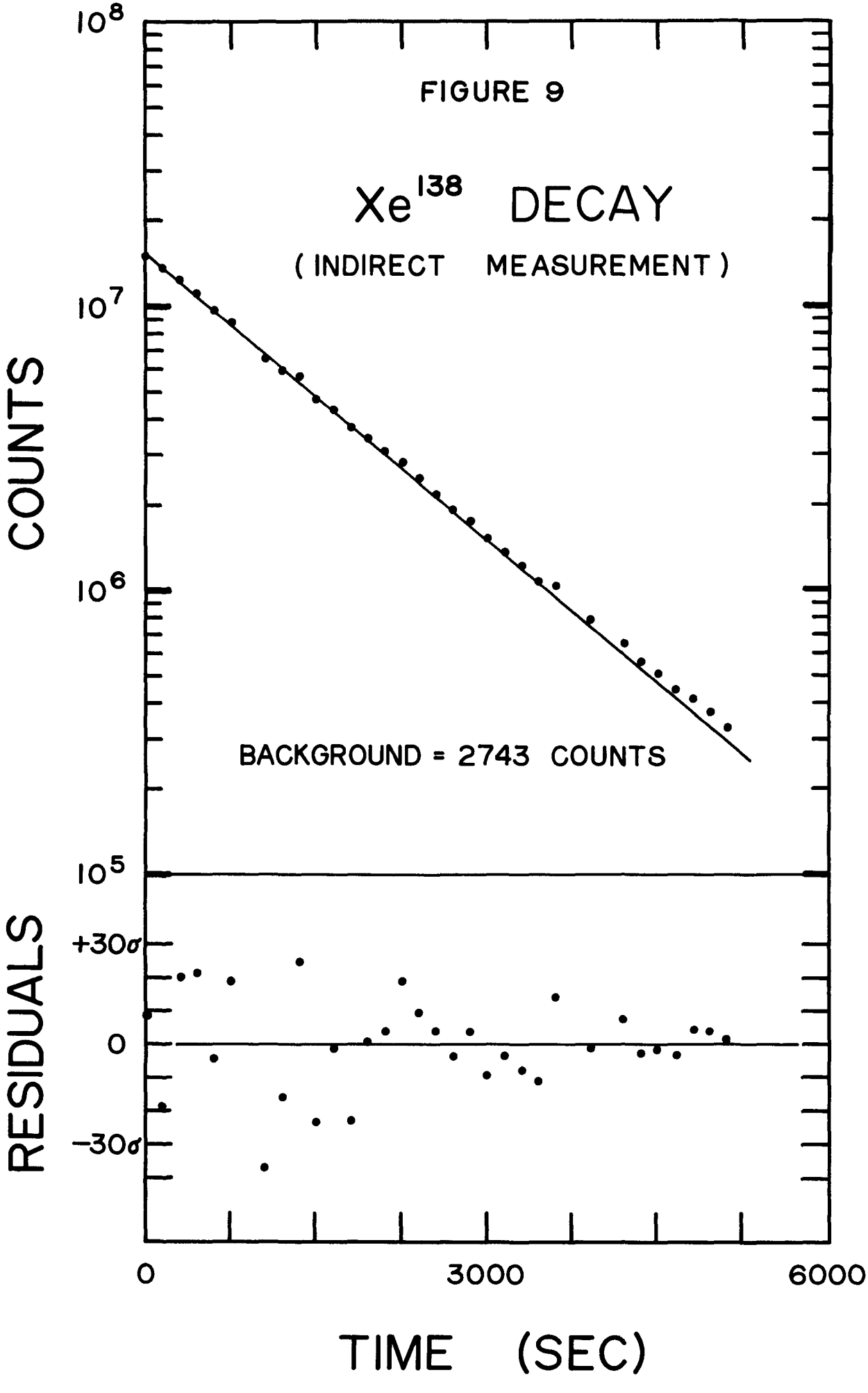
FIGURE 9
Xe138 DECAY
(INDIRECT MEASUREMENT)
BACKGROUND = 2743 COUNTS
COUNTS
RESIDUALS
10^8
10^7
10^6
10^5
+30σ
0
-30σ
0
3000
6000
TIME (SEC)

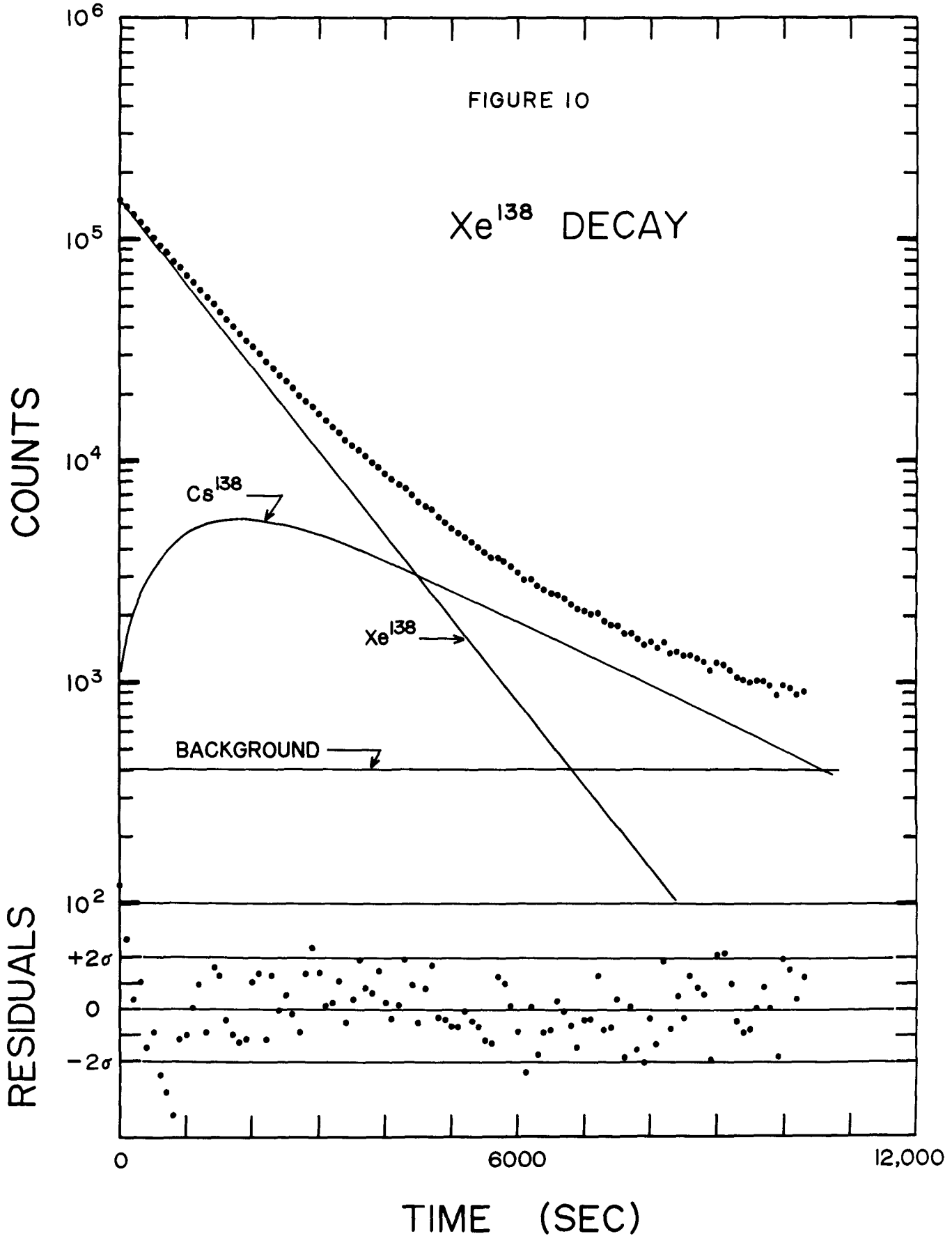
FIGURE 10
Xe138 DECAY
COUNTS
10^6
10^5
10^4
10^3
10^2
Cs138
Xe138
BACKGROUND
RESIDUALS
+2σ
0
-2σ
0
6000
12,000
TIME (SEC)

resulting half-lives are shown in Table VI.

TABLE VI

Xe^{138} Half-Life Determinations

1. Indirect Measurements

Half-life	Error
14.1 min.	± 0.8
15.0 min.	± 0.8
15.0 min.	± 0.8
Mean 14.7 min.	± 0.5

2. Direct Measurements

Half-life	Error
13.9 min.	± 1.1
13.4 min.	± 1.1
14.2 min.	± 1.1
12.8 min.	± 1.1
Mean 13.6 min.	± 0.6

Mean of indirect and direct measurements

$= 14.1 \pm 0.4$

Researcher	Xe^{138} Half-life Measured
Glasoe and Steigman (21)	17 min.
Clarke and Thode (23)	14.0 ± 0.2 min.
Hermann and Patzelt (24)	14.0 ± 0.5 min.
Present work	14.1 ± 0.4 min.

The errors in the values measured in these experiments were estimated. Because of systematic deviations which may be seen in

the decay curves of Figures 9 and 10, the least-squares error was much too small to account for the deviations observed in the various experiments.

3.2 Solid-State Detector Measurements of Cs^{138} Gamma-Radiations

In order to obtain precise measurements of gamma-ray energies by pulse-height analysis, it is necessary to define accurately the energy versus pulse-height relationship for the spectra to be analyzed. This relationship may be determined, in the case of solid-state detector measurements, with an accuracy which is limited mainly by the precision with which the gamma-ray standard energies have been defined. The calibration is usually carried out by means of the mixed-source technique whereby the gamma-ray standard sources are placed with the gamma-source for which the energies are to be determined. The gamma-spectrum for the mixture is recorded with the pulse-height analyzing system. The unknown gamma-ray energies may then be calculated by interpolation from the standard lines which appear in the spectrum. The high degree of linearity and the excellent resolution obtainable with the solid-state detector allow very accurate energy determinations to be made in this manner.

No attempt was made to continuously remove the contaminating Cs^{138} daughter activity from the Xe^{138} gamma-sources while the solid state measurements were being made. The resulting spectra always showed the more intense Cs^{138} lines. These lines were therefore used as calibration lines in the Xe^{138} spectrum, thus avoiding the complexity which would have resulted from the addition of other gamma standards. The Cs^{138} gamma energies have not, in the past, been

determined with the accuracy appropriate to solid-state detector measurements (to errors of less than 1 keV, as required in the present case). Therefore, separate experiments were carried out with a solid-state detector, using the mixed-source technique with well-known gamma standards, in order to measure the Cs^{138} line energies with the desired accuracy.

The detector was a lithium-drifted germanium "wrap-around" detector as described by Fiedler et al (42). The active volume of the detector was 12 cc. The detector was used in conjunction with a Tennelec Model 100C low-noise preamplifier and a Tennelec TC-200 pulse amplifier. The single-clipped pulse output was fed into a Nuclear Data ND 150 1024 channel pulse-height analyzer.

The gamma-ray standards which were used for the Cs^{138} gamma-energy determination are listed in Table VII.

TABLE VII

Standards Used in Cs^{138} Gamma-Energy Determinations

Nuclide	Line Energy (keV)		Reference
Pb $k_{\alpha 1}$ X-ray	75.0 ± 0.05		(43)
Hg^{203}	279.1		(44)
Na^{22}(β^+ annihilation)	511.0 ± 0.05		(43)
Cs^{137}	661.6		(45)
Na^{24}	1368.53 ± 0.04		(43)
Na^{24}	2753.9 ± 0.1		(43)
Na^{24}	2242.9 ± 0.1	1st escape	
Na^{24}	1731.9 ± 0.1	2nd escape	

Two separate spectra were recorded, one at low gain and one at high gain in order to obtain good measurements of both the high- and low-energy lines. Two measurements were therefore obtained for most of the gamma-ray energies. The final results were weighted averages of these determinations. A further check was available on the Cs^{138} energy measurements through the use of gamma-cascades occurring in the decay of the more highly excited levels. The accuracy of closure of the energy balance obtained by summing the gamma-rays participating in the cascades allowed greater confidence in the final energy determination. The decay scheme of Cs^{138} as proposed by Bunker et al (39) indicated agreement with these measurements. Table VIII shows the final results of the Cs^{138} gamma-energy determinations. The two revisions which were necessary due to energy balance requirements are also indicated. Included in the table are the energy levels determined by these results according to the decay scheme proposed by Bunker et al.

TABLE VIII

Solid-State Energy Determinations of the Cs^{138} Gamma Radiations

Revised Energy (keV)	Error	Revision Due to Energy Balance Requirements	Energy (Bunker et al)
139.3	± 1.0	-	138.9
192.9	± 1.0	-	193.1
226.9	± 1.0	-	228.9
408.7	± 0.9	-	410.6
462.4	± 1.0	-	462.6

Revised Energy (keV)	Error	Revision Due to Energy Balance Requirements	Energy (Bunker et al)
547.6	± 1.0	+ 1.0	550
871.0	± 1.5	- 3.0	870
1010.2	± 0.7	-	1010
1435.4	± 1.0	-	1426
2218.7	± 0.7	-	2210
2639.5	± 1.5	-	2630
3368	± 3.0	-	3340

- - - - - - - - - - - - - - -

Excited Levels in the Cs^{138} Nucleus,
According to above Energy Measurements
and Decay Scheme Proposed by Bunker et al (39)

Level Energy (keV)	Error
1435.4	± 1.0
1897.8	± 1.4
2218.7	± 0.7
2306.4	± 1.8
2445.6	± 1.0
2639.0	± 1.2
3368.0	± 3

3.3 Solid-State Detector Measurements of the Xe^{138} Gamma Radiations

The lithium-drifted germanium detector measurements of the Xe^{138} gamma spectrum were obtained with the same counting system used for the Cs^{138} measurements (section 3.2).

Sources of approximately 100 μc of Xe^{138} activity were used. The sources were allowed to decay 30 minutes before recording the spectra, so that the contamination due to shorter-lived xenon isotopes became negligible. The remaining xenon activity was flushed into a small charcoal cold trap which was then removed from the gas-flow system for recording of the Xe^{138} spectrum. Since the Xe^{138} gamma-rays range in energy from 150 - 2400 keV, spectra were obtained in two separate experiments, first at low and then at high amplifier gain. The detailed analysis of both the high and low energy gamma-spectrum was therefore simplified.

Gamma spectra from these experiments are shown in Figures 11 and 12.* The numbered photo-peaks refer to gamma-rays for which energy and intensity measurements are listed in Table IX. The intensities were obtained from a photo-fraction curve measured for this detector by Fiedler et al (42). In some cases revisions of the intensities of the strong gamma-transitions were made by a comparison with sodium-iodide detector results, which are discussed in the following section.

The spectra which were obtained are composites of both the Xe^{138} and the Cs^{138} gamma spectra. In order to positively differentiate between these contributions, three consecutive spectra were obtained in each case. The first spectrum was recorded immediately after the Xe^{138} was flushed into the trap and a second spectrum was

* Double pair escape peaks are labelled with 'photo-peak number, D' in these figures.

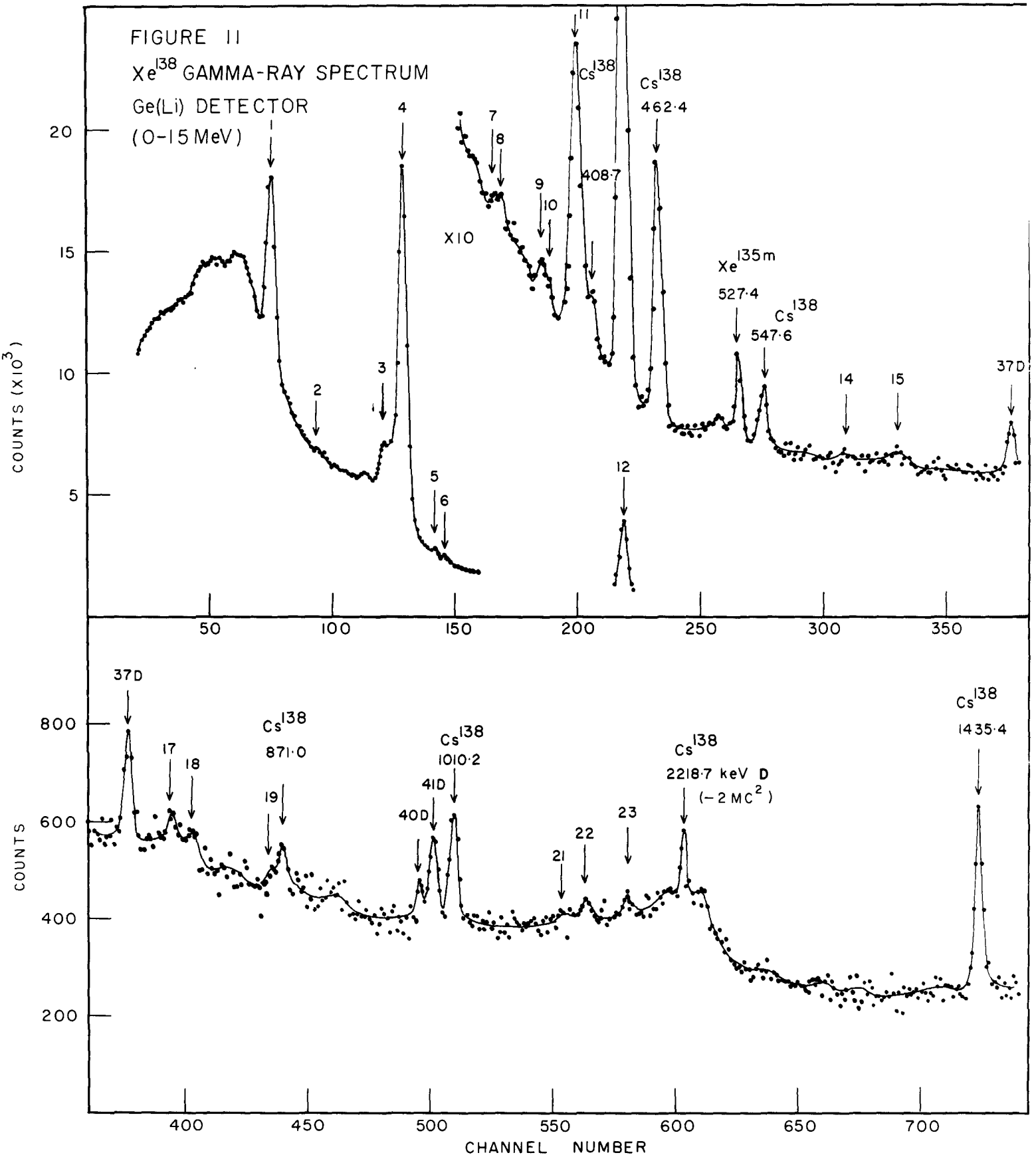
FIGURE 11
Xe138 GAMMA-RAY SPECTRUM
Ge(Li) DETECTOR
(0-15 MeV)
COUNTS (X10³)
X10
Cs138
462·4
408·7
Xe135m
527·4
Cs138
547·6
37D
Cs138
871·0
Cs138
1010·2
41D
40D
Cs138
2218·7 keV D
(-2MC²)
Cs138
1435·4
COUNTS
CHANNEL NUMBER

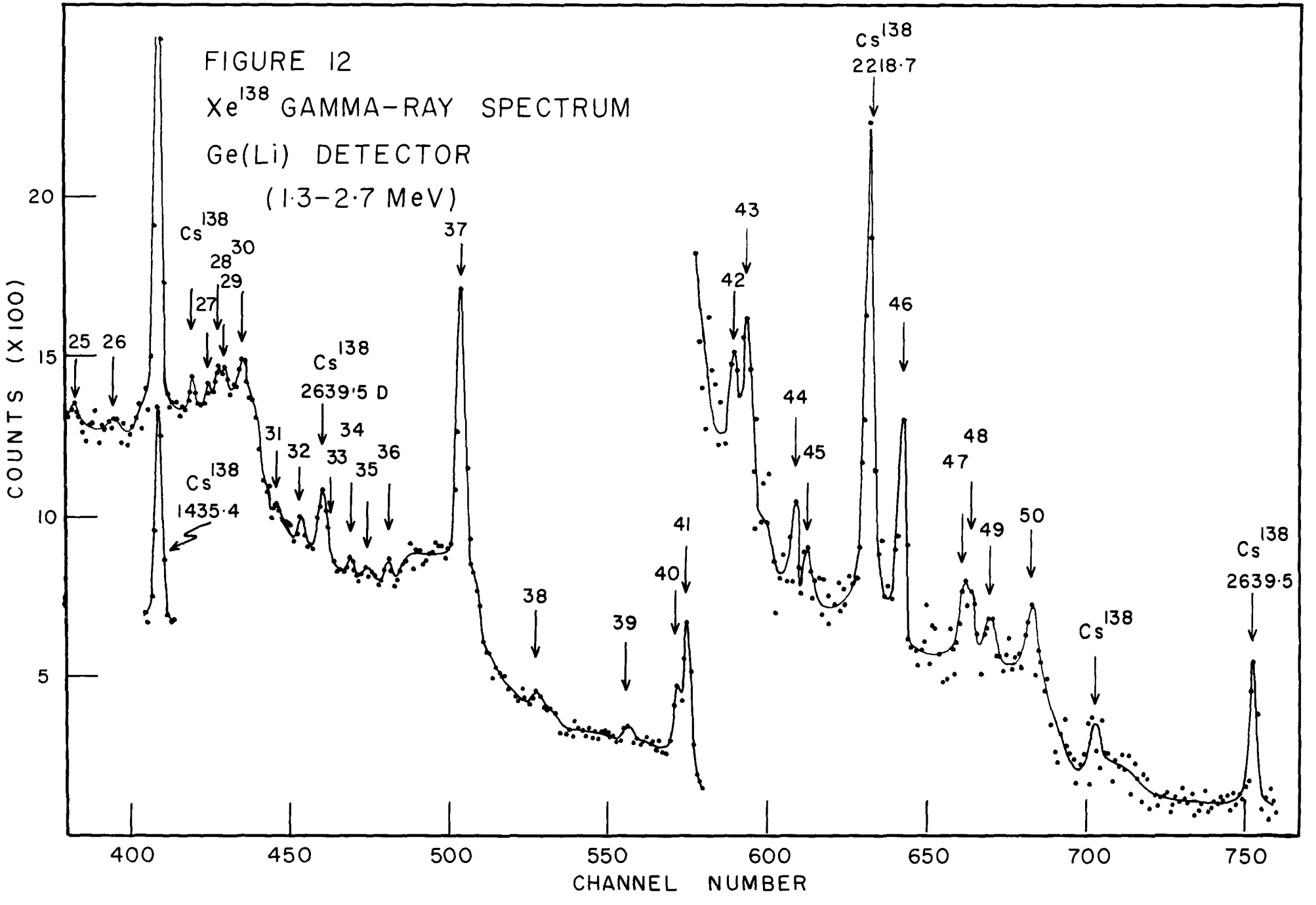
FIGURE 12
Xe138 GAMMA-RAY SPECTRUM
Ge(Li) DETECTOR
(1·3–2·7 MeV)
COUNTS (X100)
CHANNEL NUMBER
Cs138 2218·7
Cs138 2639·5 D
Cs138 1435·4
Cs138 2639·5
Cs138
25
26
27
28
29
30
31
32
33
34
35
36
37
38
39
40
41
42
43
44
45
46
47
48
49
50
20
15
10
5
400
450
500
550
600
650
700
750

TABLE IX

Xe^{138} Gamma-Ray Energies and Intensities

Line No.	Energy (keV)	Estimated Error(keV)	Intensity
1	153	2	17.9
2	187	3	0.5
3	241	2.5	6.7
4	257	1.5	100.0
5	282	3	1.1
6	290	3	1.2
7	330	3	0.8
8	336	3	1.1
9	369	4	2.3
10	375	4	0.8
11	397	1.5	20.0
12	434	1.5	56.0
13	594	3	1.4
14	613	3	1.1
15	655	3	1.7
16	695	3	2.5
17	781	3	2.5
18	800	3	2.0
19	865	5	1.7
20	945	3	2.7
21	1098	4	2.3
22	1115	4	4.1
23	1150	3	4.9
24	1298	3	3.7
25	1344	3	1.6
26	1386	5	1.5
27	1487	3	3.8

(continued next page)

TABLE IX (Continued)

Xe^{138} Gamma-Ray Energies and Intensities

Line No.	Energy (keV)	Estimated Error (keV)	Intensity
28	1500	4	6.0
29	1510	4	
30	1530	3	4.0
31	1571	3	3.3
32	1590	3	3.5
33	1620	5	1.5
34	1635	5	1.5
35	1650	3	3.0
36	1687	3	3.5
37	1769	2	52.5
38	1850	4	3.2
39	1950	4	1.9
40	2005	3	9.2
41	2015	2	38.0
42	2069	5	1.2
43	2082	4	3.7
44	2135	5	1.7
45	2146	5	1.3
46	2254	3	6.0
47	2319	5	3.4
48	2329	5	
49	2350	4	1.5
50	2395	4	2.1

taken twenty minutes later. The charcoal trap was then heated and the remaining xenon fraction flushed to exhaust. The spectrum which was then recorded consisted of only the Cs^{138} lines. The photo-peak which appears at 526 keV is tentatively assigned to meta-stable Xe^{135}. The energy of this transition has been measured by Alvager (46) to be 527.4 ± 0.8 keV.

3.4 NaI(Tl) Scintillation Detector Analysis of the Xe^{138} Singles Spectrum

For all NaI detector measurements the source was placed in the charged-wire chamber (see section 2.4). The Nuclear Data ND-150 1024 channel analyzer was used for the singles analysis. In order to correct for random and coincident sums in the spectrum, two 3" x 3" NaI detectors were used, placed at right angles 10 cm from the sample chamber. A 1/8" thick lead sheet between the detectors served as a backscatter shield.

The singles, coincident sum, and random sum spectra were routed to three 256 channel quadrants in the analyzer by means of logic signals from a Cosmic coincidence system. The circuit outline for this experiment is shown in Figure 13.

The spectrum was recorded for ten mimutes immediately following the introduction of the sample into the chamber. A decay-curve was obtained so that corrections could be applied to the spectrum for Cs^{138} contamination. Since a minimum of Cs^{138} contamination was desired , there was insufficient time following the introduction of the sample into the chamber to set up the Spectrastat high voltage stabilizers before starting the analysis. For this experiment, therefore, the source was placed near the detectors for approximately

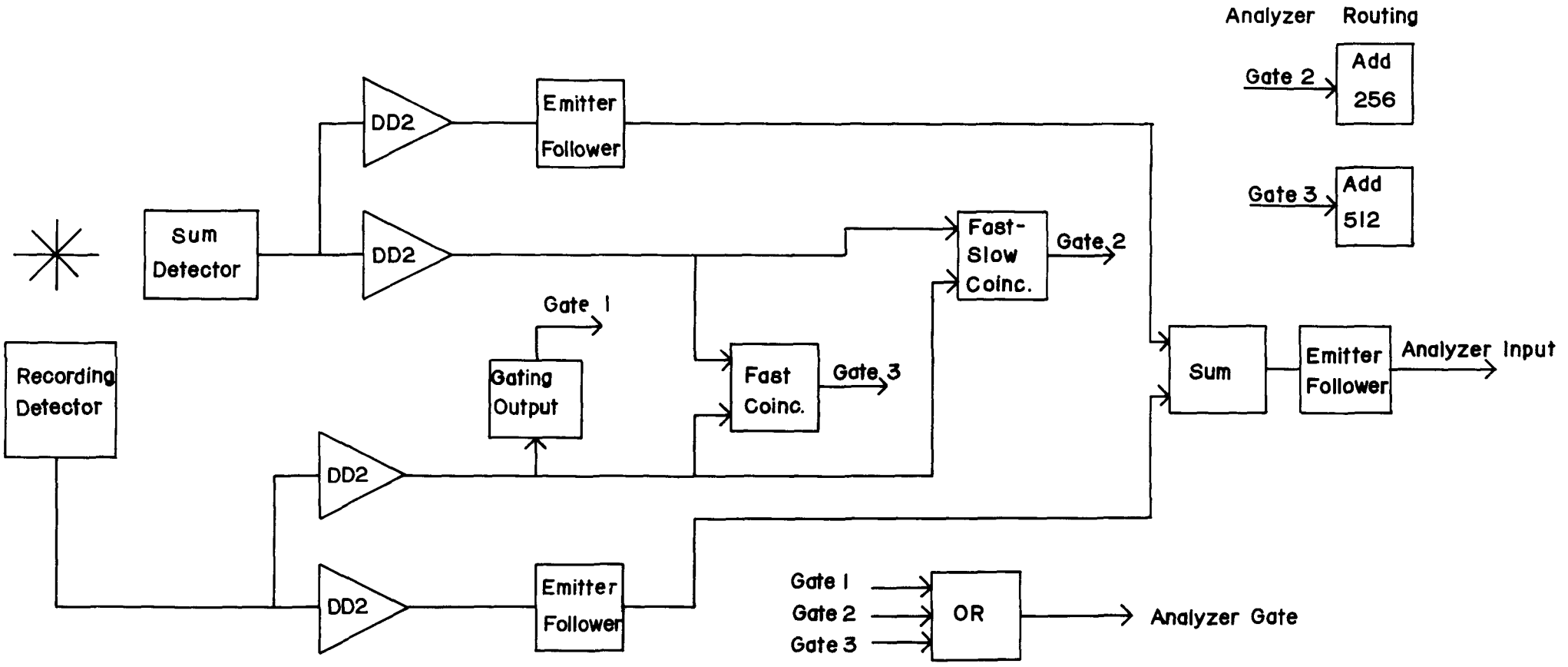

FIGURE 13.

GAMMA SINGLES ANALYSIS SYSTEM.

ten minutes prior to the experiment to minimize short-term drift in detector gain by allowing the detectors to "settle down" at the high counting rate. A Cs^{138} spectrum was obtained from the activity remaining after the residual xenon had been flushed from the chamber.

The data was corrected for summing, Cs^{138} contamination, and room background. The data analysis was performed by the line-fitting program (see Appendix II). The analyzed spectrum is shown in Figure 14. The existence of many of the weak intermediate and high energy lines indicated from the lithium-drifted detector results was impossible to show because of the relatively poor resolution of the NaI detector at these energies. However, the more intense lines and most of the low energy lines as determined are in good agreement with the solid state results. The line energies and intensities from the NaI singles results are shown in Table X. It should be noted that these results are for comparison purposes only, since the results shown in Table IX are the finally adopted values. The line energies shown in Table X were obtained by the line-fitting program which used the 2010 keV line (doublet) and the 257 keV line (doublet) as internal calibrations. The energy determinations shown for these lines do not approach in accuracy the results from the solid-state detector analysis. However,it is of interest to know the limitations of the NaI measurements. The large residuals shown in Figure 14 which appear below 200 keV are probably due to bremsstrahlung contributions in this region. The systematic trends in the residual in the region 1700 - 2100 keV are due both to inaccuracies in the line-shapes, and also

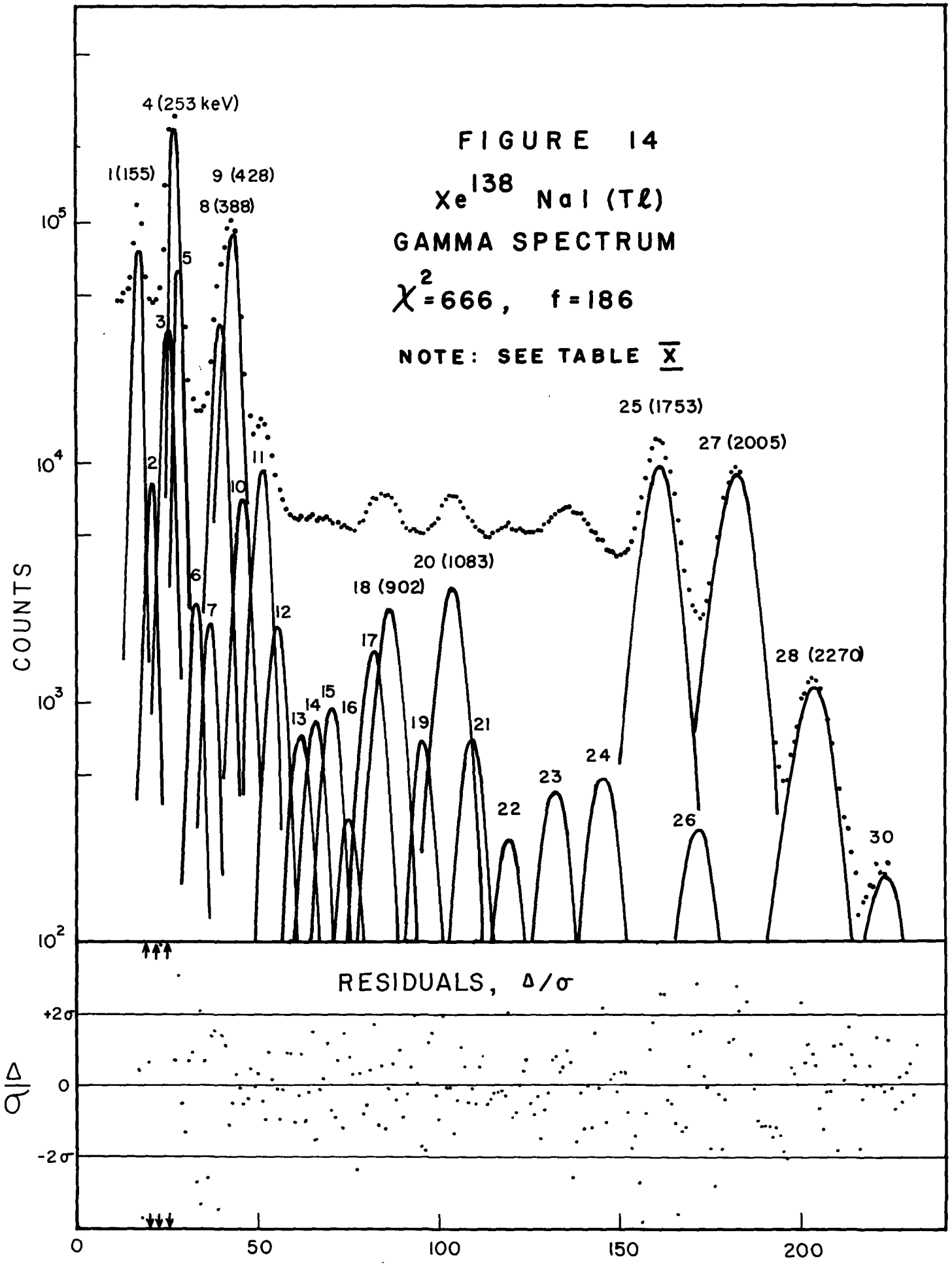
FIGURE 14
Xe 138 NaI (Tℓ)
GAMMA SPECTRUM
χ² = 666, f = 186
NOTE: SEE TABLE X
4 (253 keV)
1 (155)
9 (428)
8 (388)
25 (1753)
27 (2005)
20 (1083)
18 (902)
28 (2270)
COUNTS
RESIDUALS, Δ/σ
+2σ
0
-2σ
|Δ/σ|
0
50
100
150
200

TABLE X

Xe^{138} Gamma-Ray Energies and Intensities From Analysis of NaI Detector Spectrum

(Line Intensities are Corrected for Counter Efficiency)

Note: The line numbers refer only to lines found in the NaI results of Figure 14.

Line No.	Energy	Intensity	Comment
1	155	20.3	
2	188	2.9	
3	239	14.9	
4	253	100.0	
5	285	2.9	
6	316	1.3	
7	358	1.3	
8	388	25.9	
9	428	69.6	
10	455	6.0	Cs^{138}
11	516	9.5	Xe^{135*}
12	558	2.4	Cs^{138}
13	621	1.0	
14	675	1.3	
15	723	1.6	
16	769	0.6	
17	856	3.5	
18	902	5.6	

(continued next page)

TABLE X (Continued)

Xe^{138} Gamma-Ray Energies and Intensities From Analysis of NaI Detector Spectrum

(Line Intensities are Corrected for Counter Efficiency)

Note: The line numbers refer only to lines found in the NaI results of Figure 14.

Line No.	Energy	Intensity	Comment
19	994	1.8	Cs^{138}
20	1083	9.5	
21	1152	2.4	
22	1265	1.0	
23	1413	1.8	Cs^{138}
24	1565	2.5	
25	1753	56.8	
26	1885	1.9	
27	2005	61.3	
28	2269	9.7	
29	2363	0.8	
30	2500	1.9	

to the omission of a number of the weaker lines from the analysis in this region.

3.4.1 Analysis of the NaI Coincident-Sum Spectrum

The sum contributions in the NaI detector results were recorded so that the singles spectra could be corrected for these effects. However, the coincident-sum spectrum also contains information which is useful in determining the nuclear level structure. The coincident-sums were therefore recorded separately from the gross gamma-gamma sum contribution, making these results available for further analysis. Kennett et al (47) have given a detailed analysis of the spectral contributions to be expected from both time-correlated (gamma-gamma cascade) events and from randomly correlated events. The contributions from both coincident and random summing in the Xe^{138} spectrum are shown in Figure 15 . The average counting rate in this experiment was 11,000 counts/sec. Table XI lists the coincident-sum energies which were obtained from the analysis of these data.

TABLE XI

Xe^{138} Gamma-Gamma Coincident-Sum Energies

Sum Peak Energy (keV)	Comment
280	Weak
400	Intense
570	Possibly Cs^{138}
750	" "
1000	Cs^{138}
1450	Cs^{138}
1770	Weak
2000	Intense
2250	Intense

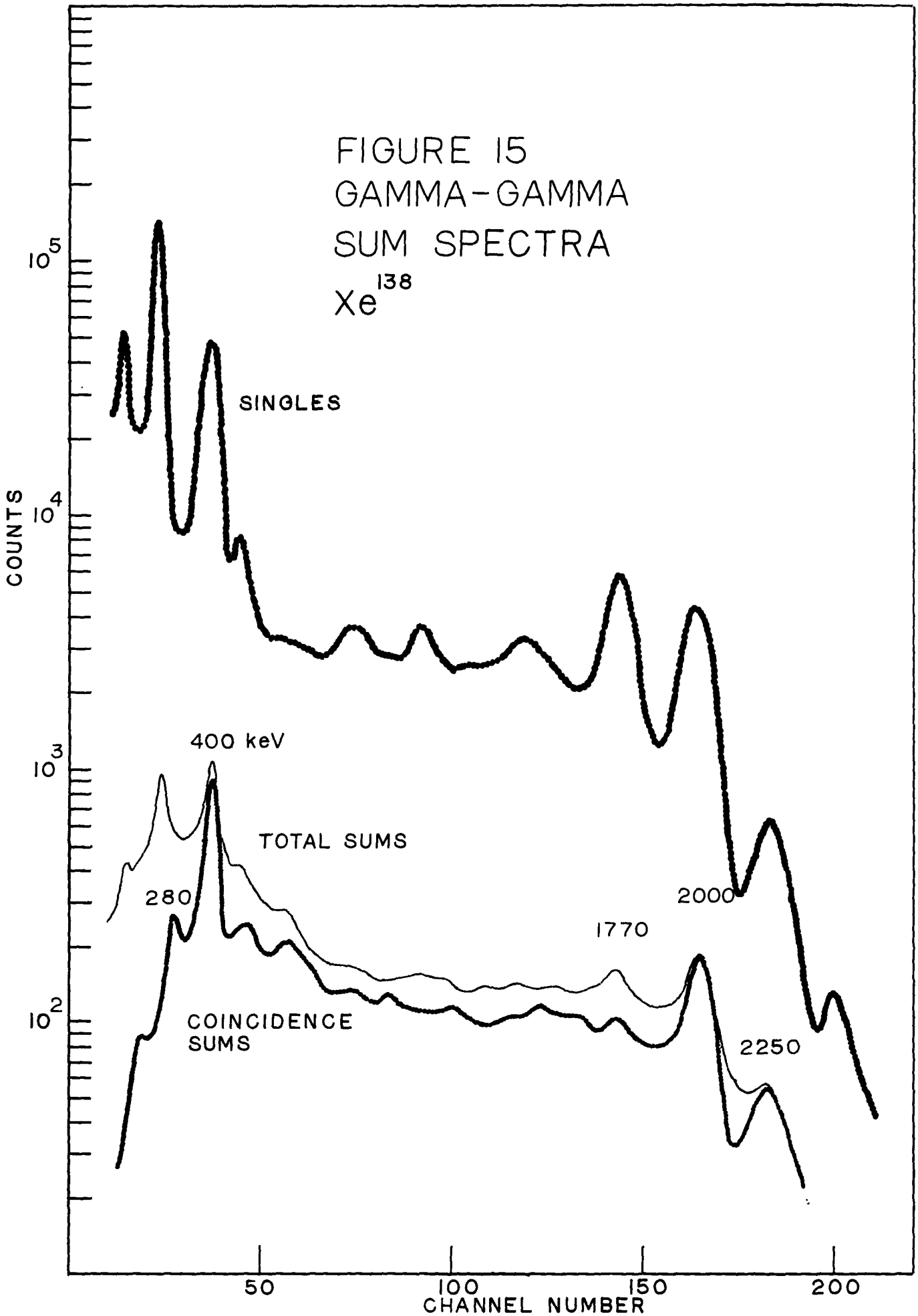
FIGURE 15
GAMMA-GAMMA
SUM SPECTRA
Xe 138
SINGLES
400 keV
TOTAL SUMS
280
2000
1770
COINCIDENCE
SUMS
2250
COUNTS
10 5
10 4
10 3
10 2
50
100
150
200
CHANNEL NUMBER

3.5 Xe^{138} Gamma-Gamma Coincidence Measurements

The ND-150 analyzer was used for a large portion of the coincidence measurements, in conjunction with a Cosmic coincidence unit, three 3" x 3" NaI detectors and five transistorized DD2 amplifiers. The three-crystal arrangement was used to correct for summing in the coincidence spectra. Random summing in the coincidence runs was of particular importance because of the high counting rates (15,000 - 20,000/sec) in these runs. The arrangement of the detector system in relation to the charged-wire chamber is shown in Figure 7. The resolving time of the fast coincident circuits was 50 nsec. The spectra were routed to the four 256-channel groups in the analyzer as follows:

Group 1. Singles were recorded in this location for a small fraction (2%) of the duration of the experiment. This was accomplished by a programmer which switched in gating pulses derived from the recording detector output for brief periods at intervals of 30 seconds during the experiment. The singles spectra were used in the data analysis for energy calibration, and were useful also as a check on sample purity.

Group 2. Coincidence spectrum.

Group 3. Chance spectrum.

Group 4. Random-and coincident-sum spectrum.

A schematic diagram of the detection and analysis system is shown in Figure 16. In order to demonstrate the capabilities of this system in coincidence measurements, the spectrum in coincidence with the 1475 keV line in Br^{82} was analyzed. The resulting spectra are shown in Figure 17. There were also small contributions in the

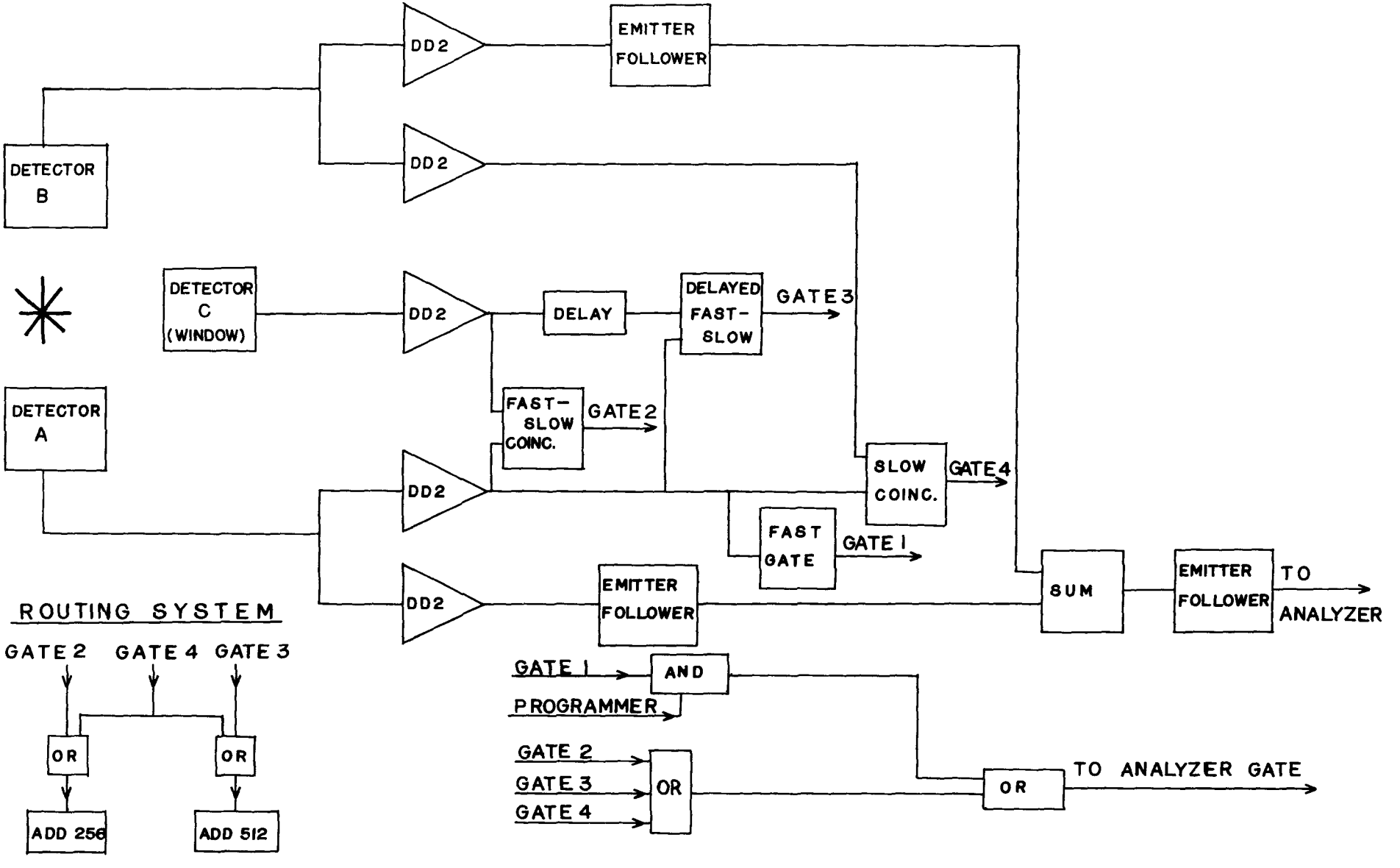

FIGURE 16

COINCIDENCE SYSTEM

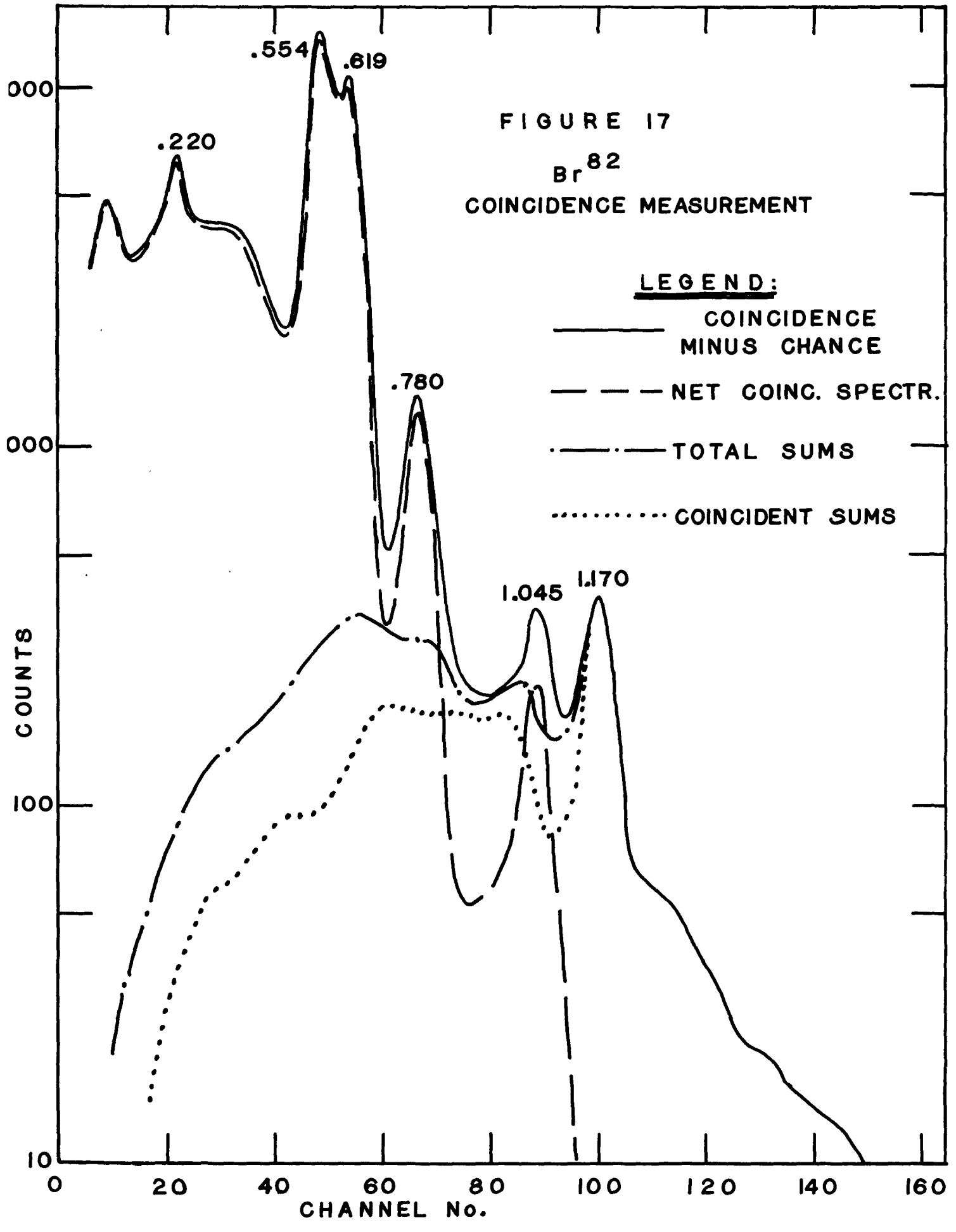
.554
.619
.220
.780
1.045
1.170
000
000
100
10
COUNTS
0
20
40
60
80
100
120
140
160
CHANNEL No.
FIGURE 17
Br 82
COINCIDENCE MEASUREMENT
LEGEND:
COINCIDENCE MINUS CHANCE
NET COINC. SPECTR.
TOTAL SUMS
COINCIDENT SUMS

coincidence "window" which were due to the 1317 keV and the 1650 keV lines. The results obtained are in agreement with measurements summarized in the Nuclear Data Sheets (48), modified by the work of Kennett et al (49).

A series of coincidence measurements were carried out on the Xe^{138} gamma-radiations, with coincidence windows set on each of the more intense gamma-rays in turn. The experimental procedure was as follows:-

1) The sample was produced in a 15 second irradiation and the xenon fraction separated out. Following a cooling period of 30 minutes, the sample was injected into the charged wire chamber.

2) The amplifier gains, coincidence windows, etc., had been set up previous to the sample injection. However, a few minor adjustments were usually necessary before beginning the run.

3) Analysis was started 3 to 4 minutes after sample injection. Coincidence, chance, and window events were scaled. The analysis was stopped after 14 minutes.

4) Two 256 channel groups were typed out and recorded on perforated tape.

5) The coincidence window and the window detector singles were recorded.

The remaining data was then read out. The data on perforated tape could be converted directly to cards for computer analysis.

An example of the results obtained is shown in Figure 18 which shows the spectrum in coincidence with the 241-257 keV

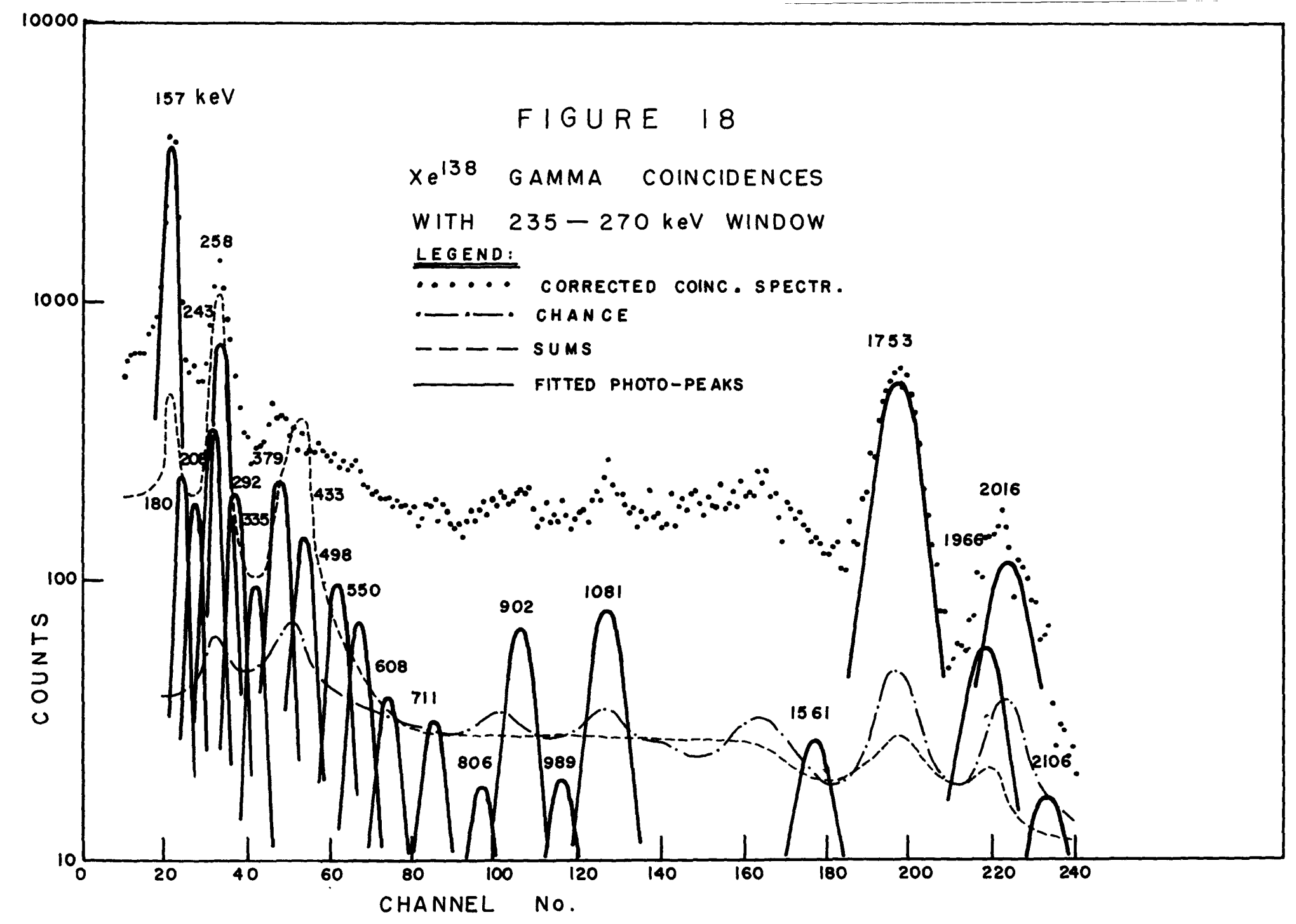
FIGURE 18
Xe138 GAMMA COINCIDENCES
WITH 235 — 270 keV WINDOW
LEGEND:
CORRECTED COINC. SPECTR.
CHANCE
SUMS
FITTED PHOTO-PEAKS
157 keV
258
243
206
180
379
292
335
433
498
550
608
711
806
902
989
1081
1561
1753
1966
2016
2106
COUNTS
CHANNEL No.
10000
1000
100
10
0
20
40
60
80
100
120
140
160
180
200
220
240

doublet and also the summing and chance contributions. Figures 19 to 22 show some of the coincidence spectra obtained by gating with the other intense lines in the spectrum. A total of more than 25 coincidence measurements was made in this fashion. However, the abundance of low intensity gamma-rays indicated that the analysis of these spectra for unique gamma-gamma coincidence assignments might better be handled by least-squares techniques (see section 3.6). In order to obtain more accurate and meaningful results by these techniques, more coincidence experiments were necessary. Therefore, four two-dimensional γ-γ coincidence runs were carried out with the ND-160 analyzer and a two-detector arrangement. The analyzer configuration for these experiments was 16 x 256, with the full Xe^{138} coincidence spectra being recorded in the 256 channel groups. The coincidence spectra were gated by a 15 channel window which was set on appropriate spectrum energies. The source activity was somewhat lower for these runs than in the previous coincidence measurements, because no corrections could be applied for random summing. However, the chance rate was monitored and an appropriate fraction of the singles spectrum subtracted from each coincidence spectrum before the data were analyzed. The singles spectra were recorded during the run in the first channel group on each axis with the aid of an electronic programming device described by Kennett (50).

The reduction of the coincidence data involved the analysis of over 70 coincidence spectra. This was accomplished by the use of the line-fitting program described in Appendix III. 39 lines appeared in these coincidence measurements. The actual gamma-gamma

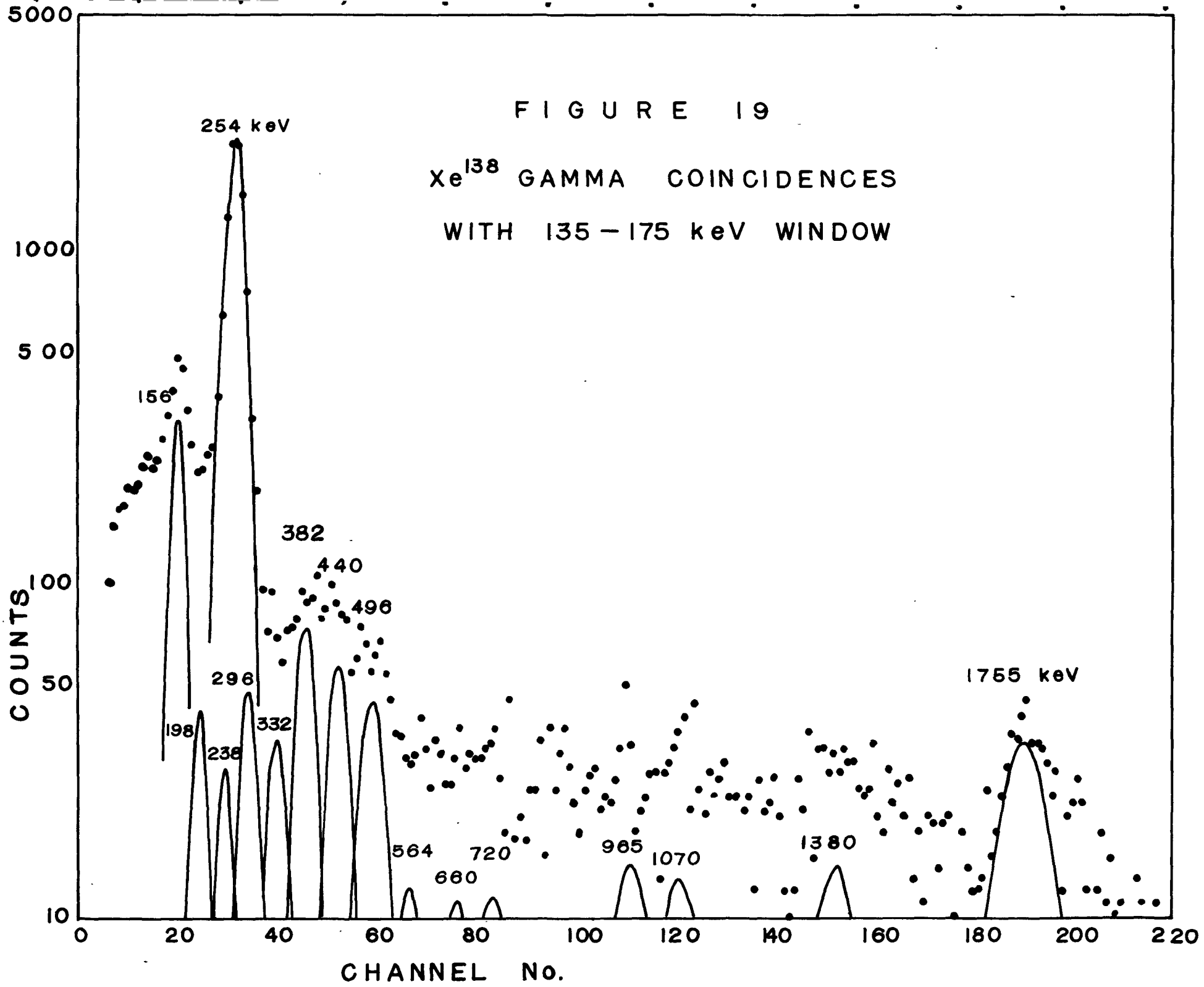
FIGURE 19
Xe138 GAMMA COINCIDENCES
WITH 135 – 175 keV WINDOW
254 keV
156
382
440
496
296
198
238
332
564
660
720
965
1070
1380
1755 keV
COUNTS
CHANNEL No.
5000
1000
500
100
50
10
0
20
40
60
80
100
120
140
160
180
200
220

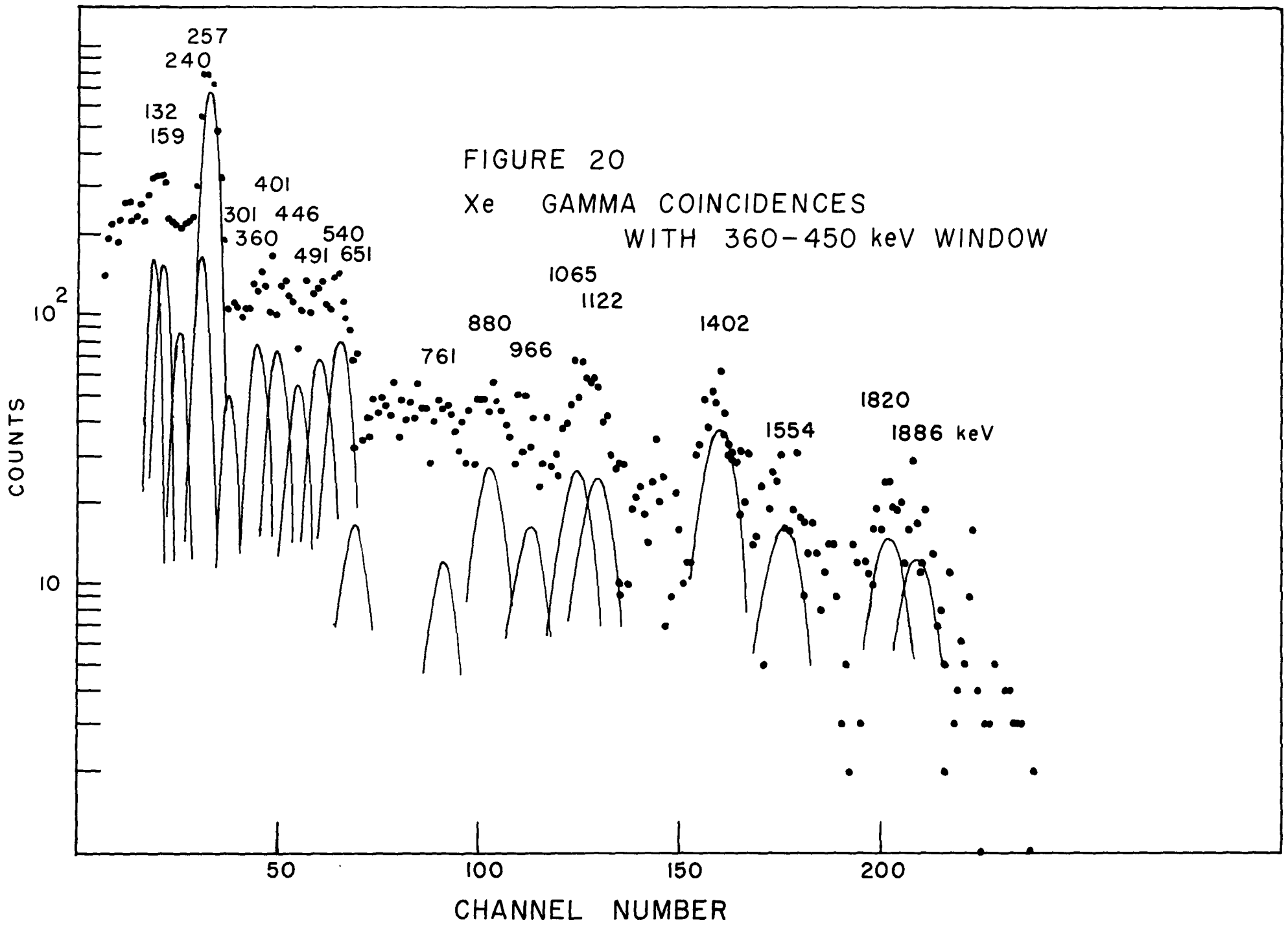

FIGURE 20

Xe GAMMA COINCIDENCES WITH 360–450 keV WINDOW

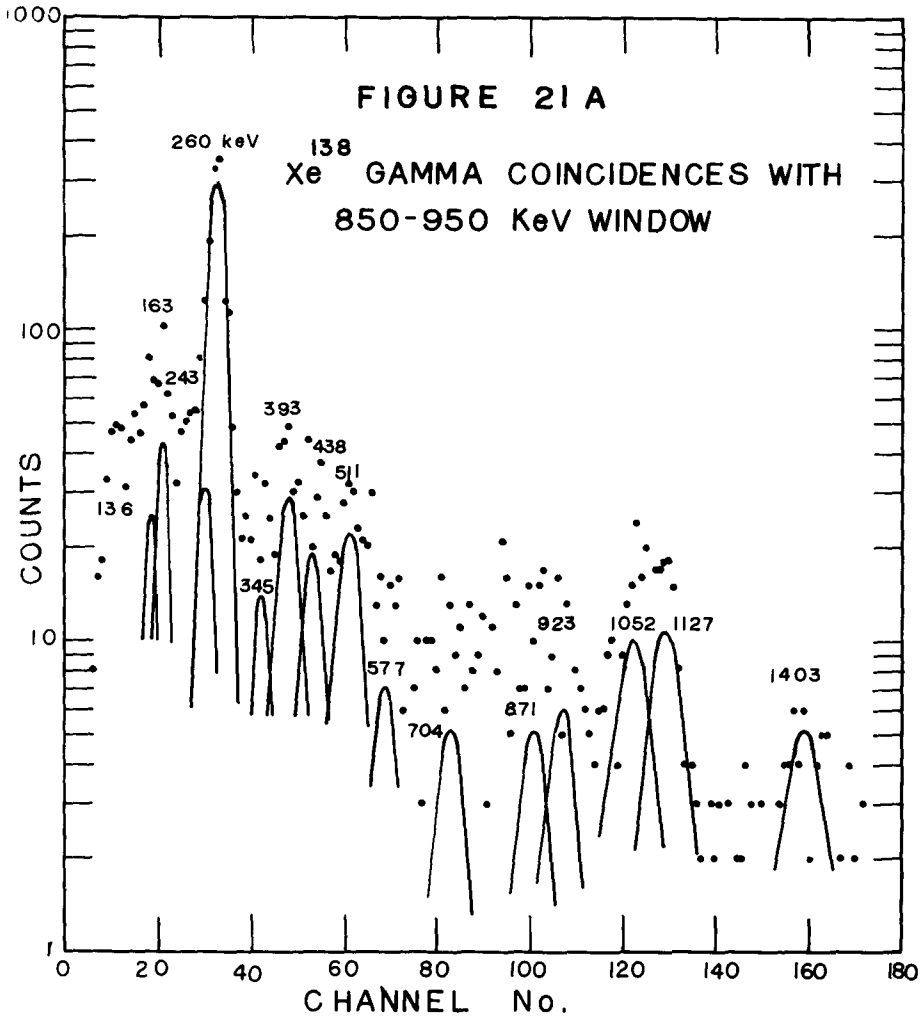
FIGURE 21 A
^{138}Xe GAMMA COINCIDENCES WITH
850-950 KeV WINDOW
260 keV
163
243
136
393
438
511
345
577
704
871
923
1052
1127
1403
COUNTS
CHANNEL No.
1000
100
10
1
0
20
40
60
80
100
120
140
160
180

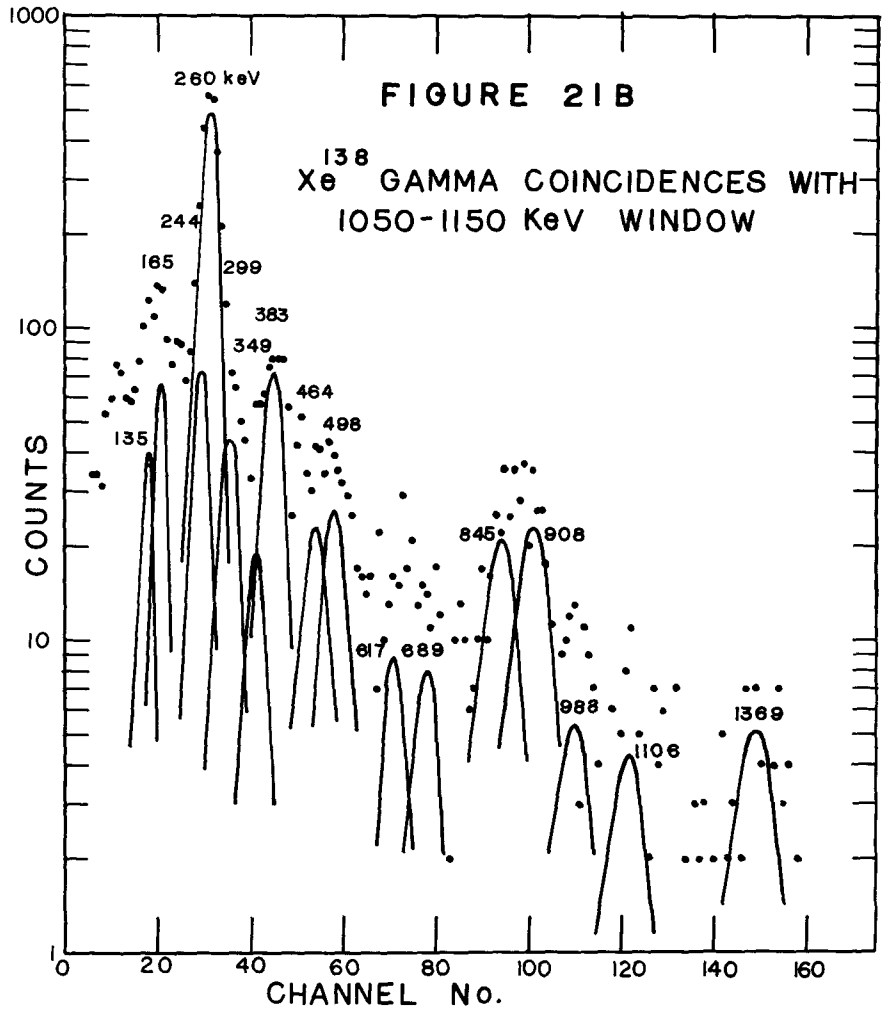
FIGURE 21 B
^{138}Xe GAMMA COINCIDENCES WITH
1050-1150 KeV WINDOW
260 keV
244
165
299
383
349
464
498
135
845
908
617
689
988
1106
1369
COUNTS
CHANNEL No.
1000
100
10
1
0
20
40
60
80
100
120
140
160

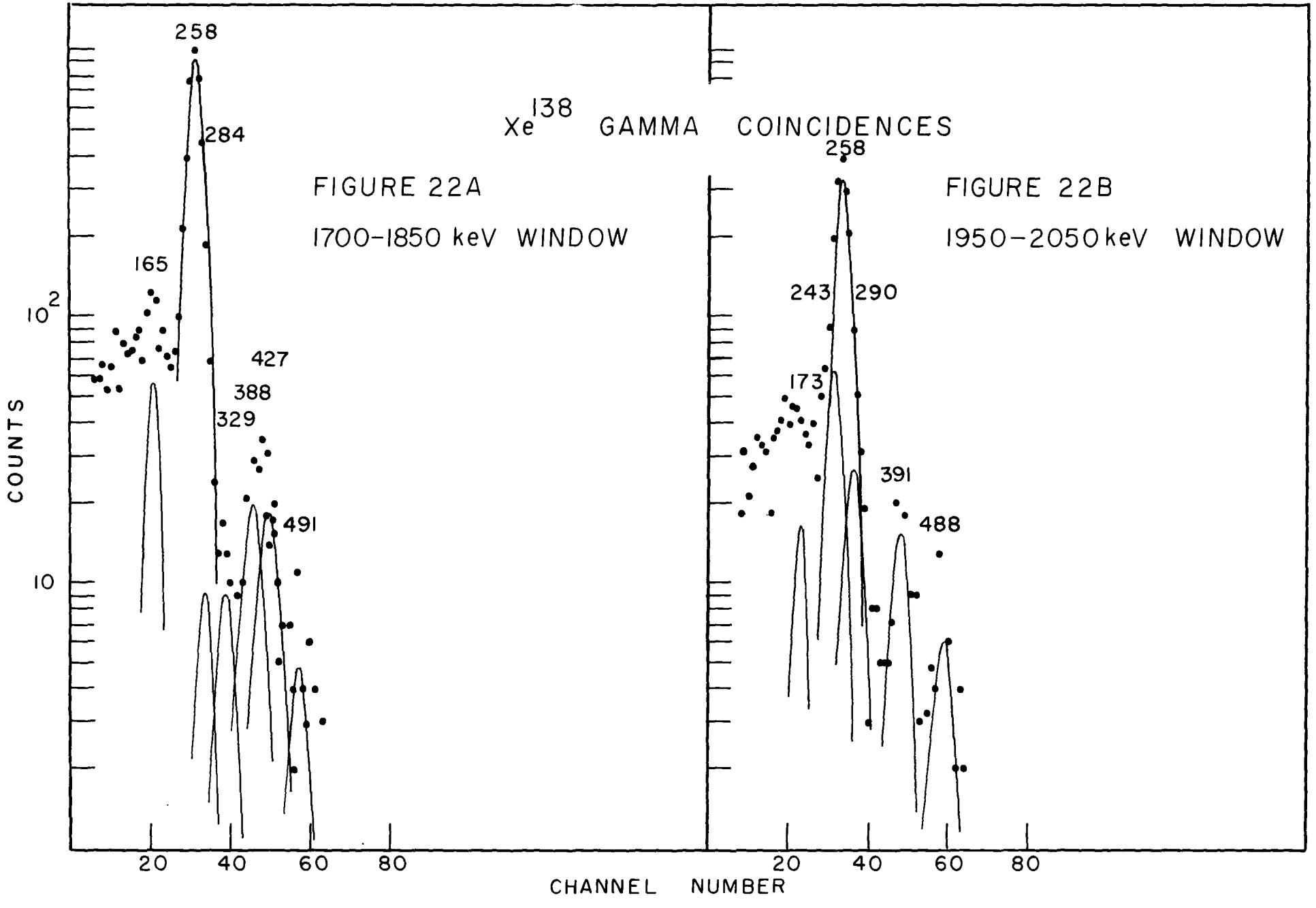
Xe 138 GAMMA COINCIDENCES
FIGURE 22A
1700-1850 keV WINDOW
FIGURE 22B
1950-2050 keV WINDOW
258
284
165
427
388
329
491
258
243
290
173
391
488
COUNTS
10^2
10
20
40
60
80
CHANNEL NUMBER

coincidence results were derived from the intensity of each line which appeared in each spectrum by means of a coincidence-quotient least-squares analysis which is described in the following section.

3.5.1 Least-Squares Coincidence-Quotient Analysis

The information which is obtained from the reduction of coincidence data may easily be utilized if the fraction of events appearing in the coincidence gating window is due mainly to one gamma-ray. It is evident that, if this is the case, then the intensity of lines in the resulting coincidence spectrum is related to gamma-gamma cascades in which the gating gamma-ray participates. However, if low intensity gamma-rays appear in the gating window along with large Compton contributions due to intense higher energy lines, then the coincidence of the weak gamma-rays with lines appearing in the coincidence spectrum is difficult to establish. This is indeed the case with gamma-coincidence measurements on the Xe^{138} decay. However, this difficulty may be overcome to a certain extent by utilizing information from all the coincidence runs in a least-squares fit to the intensity of particular lines found in the coincidence spectra. The parameters which are determined are referred to as the coincidence-quotients between particular coincident pairs. The least-squares fit for these parameters is an extension of the technique used by Johnson and O'Kelley (51).

We set up the equation

$$n_{ik} = \epsilon_i e^{-u_i d} c_k \sum_j a_{jk} q_{ji} \qquad (3.5.1.a)$$

Where:

n_{ik} is the intensity of the i-th line appearing in the k-th

coincidence measurement,

ϵ_i is the absolute detection efficiency for the i-th line,

$e^{-u_i d}$ corrects for absorption in the source and beta absorber

c_k is the number of counts falling in the coincidence window during the k-th run

a_{jk} is the fraction of the window rate in the k-th run due to the j-th line, referred to as the gating fraction,

q_{ji} is the coincidence quotient between the j-th line and the i-th line.

The gating fractions a_{jk}, are determined through the analysis of a singles spectrum and by careful determination of coincidence window locations in the pulse-height spectrum in each case. The appearance of non-zero values for the parameters q_{ij}, for $i = j$, may indicate either the existence of a coincident doublet or chance coincidences of the j-th line with itself. For the sake of simplicity, angular correlations between coincident gamma-rays are neglected in this discussion, because for this nucleus these correlations have not been established.

Physically speaking, equation (3.5.1.a) indicates that if an excited state populates/decays by the emission of the i-th gamma-ray, then q_{ji} is the probability that the level will decay/populate by the emission of the j-th gamma-ray. This statement is true only for cascade pairs. By re-arranging (3.5.1.a) we have

$$\sum_j a_{jk} q_{ji} - \frac{n_{ik}}{\epsilon_i e^{-u_i d} c_k} = 0$$

If the i-th line appears in ℓ coincidence runs, then we may determine by least squares q_{ji} for a maximum of $(\ell-1)$ lines j. The

least-squares equation is

$$\sum_k w_k \left(a_{jk} q_{ji} - b_{ik} \right)^2 = \min$$

Where w_k is the weighting, and

$$b_{ik} = n_{ik} \Big/ \sigma_i e^{-u_i d} c_k$$

The q_{ji} may therefore be determined by linear least-squares.

Weighting

It is very difficult to weight the data accurately since in this case the independent variables a_{jk} are subject to error. This error arises from two sources: from the line intensity measurements, and from the determination of gating window positions in the pulse-height spectrum. The error in line intensities is available from the least-squares analysis of the singles spectrum. The error in window position is usually small for runs in which the window covers a relatively large region of the spectrum. However, in the fine mesh encountered in two-dimensional spectrum analysis the error in estimating the "window" position is appreciable. The procedure followed in the present work was to assume an initial weighting w_{ik}, where

$$\frac{1}{w_{ik}} = \delta^2 \left(b_{ik} \right)$$

The q_{ji} were then calculated. Since the a_{jk} are subject to error, the calculated value of the q_{ji} will serve to determine a better approximation to the weighting as follows:

$$\frac{1}{w_{ik}} = \delta_{ik}^2 = \delta^2(b_{ik}) + \sum_j \delta^2(a_{jk}) \cdot \left(\frac{\partial b_{ik}}{\partial a_{jk}} \right)^2$$

$$= \delta^2(b_{ik}) + \sum_j \delta^2(a_{jk}) \cdot (q_{ji})^2$$

The (n + 1)th approximation to the weighting is

$$\frac{1}{(w_{ik})_{n+1}} = \left(\delta^2_{ik}\right)_{n+1} = \delta^2(b_{ik}) + \sum_j \delta^2(a_{jk}) \cdot (q_{ji})^2_n$$

The least-squares fit is repeated in each case until $X^2_{n+1} \longrightarrow X^2_n$.

Calculations

It is preferable to fit all the lines which may possibly be in cascade with the line of interest, unless certain cascades have been ruled out by other information. The initial model which is assumed is therefore usually incorrect. However, certain lines which are obviously not in coincidence with the line of interest may be dropped from succeeding calculations. In the present work, the computer program was written in such a way that, after the first calculation, all lines with q_{ji} less than zero were dropped from consideration; then all with $\delta(q_{ji})$ greater than $4.0\ q_{ji}$, and so on, until only those $q_{ji} > \delta(q_{ji})$ remained in the final calculation.

Results

The results were not expected to be sufficiently accurate for lines of low intensity; consequently estimates of the level populations could not be made. However, values obtained in many cases were used as indications of gamma-gamma cascades. Tables XIIA and XIIB show the coincidence quotients obtained which were greater than the calculated errors for these values. The error results are also shown for the coincidence quotients of the strong lines. If these values are to be used in the calculation of beta-

TABLE XIIA

COINCIDENCE QUOTIENTS

Gating Line (NaI) keV	Includes Lines	COINCIDENT LINE										
		153 (1)	187 (2)	241 (3)	257 (4)	285 (5,6)	320 (7,8)	397 (11)	610 (13,14)	655 (15)	695 (16)	781 (17,18)
153	1			.05	.73 ± .07	.02	.01					
187	2				1.0 ± .45				.40			
241	3											
257	4	.156±.007	.009			.01	.007		.012		.16	.006
285	4,6											
320	7,8	1.1±.2										
360	9,10											
397	11					.02	.01					
434	12											
620	13,14											
675	15,16								.28			
720	16,17							.22 ± .05				
770	17,18			.01	.17 ± .08				.10			
860	19			.04	.65 ± .20			.46 ± .22		.33		
900	19,20							.17 ± .08	.22			
1080	21			.07	1.08± .40			1.78 ± .35	1.5	.86		
1150	22,23											
1265	24-26		.27									
1565	28-36		.02									
1769	37			.055	.891±.052	.045						
1885	38,39											
2005	40-45			.285	1.57±.25	.176						
2270	45-48											
2365	49											

TABLE XIIB

COINCIDENCE QUOTIENTS

Gating Line Na(keV)	Includes Lines	COINCIDENT LINE									
		865 (19)	945 (20)	1098 (21)	1298 (24)	1487 (27)	1530 (28-30)	1590 (30-33)	1769 (37)	1850 (38)	2005 (40,41)
153	1	.015		.03				.06		.08	
187	2										
241	3										
257	4		.02	.03	.03		.02		.44 ± .03		.157 ± .008
285	5,6								1.4 ± 1.2		
320	7,8								2.2 ± 2.0		
360	9, 10							.74			.87 ± .30
397	11		.02			.22				.12	
434	12			.03				.02			
620	13,14										
675	15,16				.15						
720	16,17	.12	.20								
770	17,18										
860	19	.40									
900	19,20	.18		.81							
1080	21	2.4									
1150	22,23										
1265	24-26										
1565	28-36										
1769	37										
1885	38,39										
2005	40-45										
2270	45-48										
2365	49										

branching to a particular level, then when only double cascades are involved,

$$r_{\ell m} = \frac{n_{\beta_\ell}}{n_m} = 1 - \sum_i q_{mi} + \sum_{j \neq m} \left(\frac{n_j}{n_m} \sum_i q_{ji} \right)$$

Here, the β branching r_{ℓ_m}, to the ℓ-th level is related to the intensity of the m-th gamma-ray. The values of n_m and n_j are the intensities of the appropriate gamma-rays, and n_{β_ℓ} is the intensity of the beta transition to the ℓ-th level. The application of the coincidence-quotient calculations to the decay scheme analysis is discussed further in Chapter IV.

3.5.2 X-ray Coincidence Analysis

Figure 23 shows the low energy gamma-spectrum of Xe^{138}. The x-rays are seen to have a moderately high intensity compared with the two intense gamma-lines shown. The calculated K x-ray intensity relative to the 257 keV line is 6.5%, assuming a 20% x-ray absorption loss in the chamber walls.

Experimentally one may determine conversion coefficients of selected gamma-rays by carrying out coincidence experiments to determine the gamma-rays which are coincident with the x-rays. If the decay scheme is known accurately, then gamma-rays which are shown to be in coincidence with x-rays from the conversion process are also in cascade with gamma-rays which depopulate the same levels as the corresponding conversion electrons. By determining the intensity of the x-ray-gamma coincidences, the conversion coefficients may be calculated.

In the present case the assumption was made that the x-rays arose entirely from conversion of the intense 153 and 257 keV gamma-

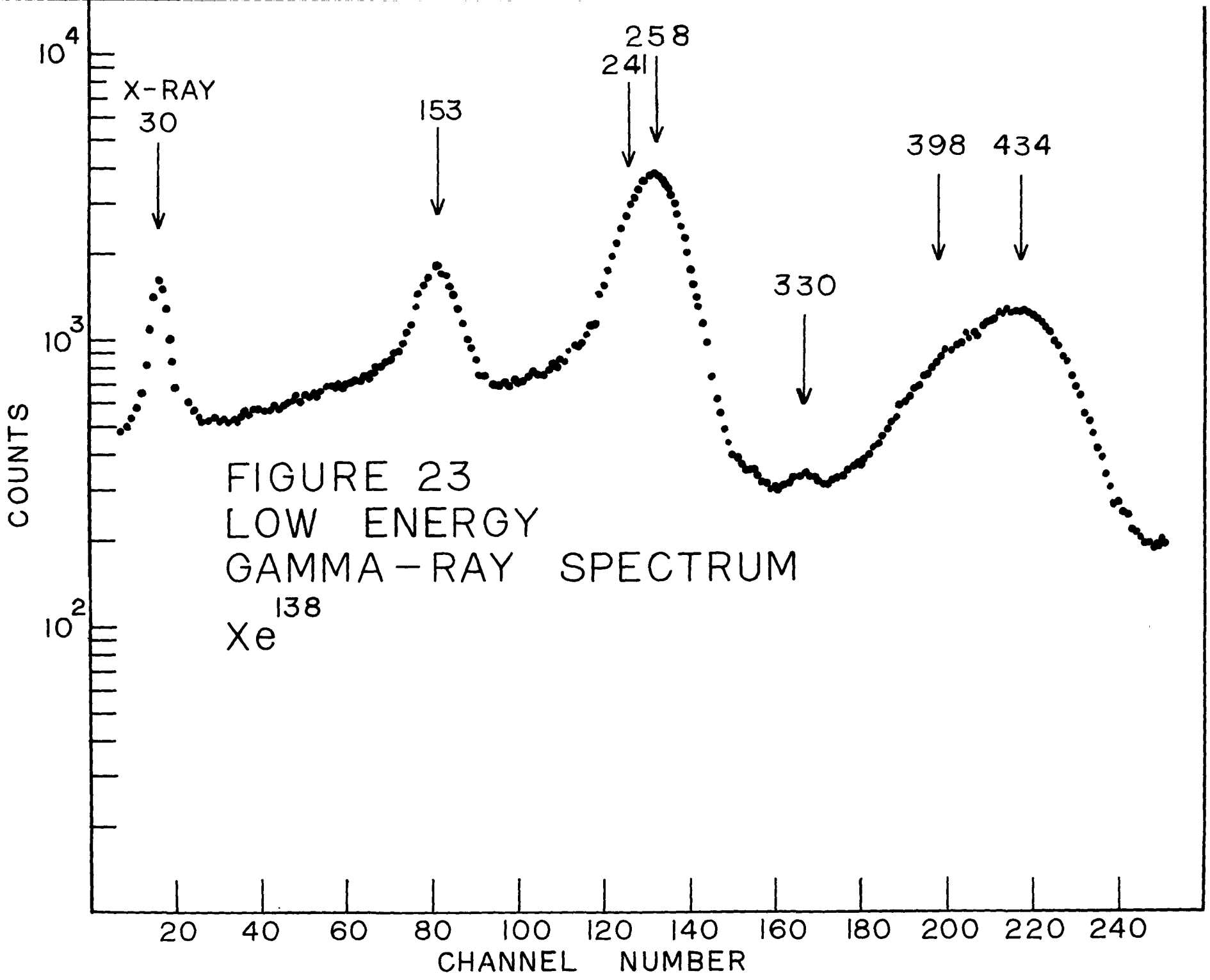

FIGURE 23
LOW ENERGY
GAMMA-RAY SPECTRUM
Xe^{138}

rays. The decay-scheme analysis showed that the 257 keV level, which decays by emission of the 257 keV gamma-ray, is populated directly by the 153 keV gamma. The beta-ray branching to this level is 8.6%. The gamma-spectrum in coincidence with the x-ray was analyzed as well as a spectrum in coincidence with the continuum slightly above the x-ray in energy. The resulting intensities of the 153 kev and 257 keV gamma-rays in these spectra gave conversion coefficients for these transitions as follows.

Conversion Coefficients From X-ray Intensities

Transition energy (kev)	α_K
153	$0.11 \begin{smallmatrix} + 0.1 \\ - 0.05 \end{smallmatrix}$
257	$0.045 \begin{smallmatrix} + 0.01 \\ - 0.02 \end{smallmatrix}$

The vacancy in the K-electron shell following the emission of a K-conversion electron is filled by the transition of an L-electron into the K-shell. The binding energy difference $(B_K - B_L)$ in this transition may be given up either by the emission of a K x-ray or an Auger electron. The competition between these two processes is described by the K fluorescence yield, which is defined as the number of K x-ray quanta emitted per vacancy in the K-shell. The above conversion coefficients have been corrected for a fluorescent yield of 0.87 for cesium, as reported by Broyles et al (52). The calculated value of α_K for the 257 keV transition was confirmed by x-ray coincidence measurements on the 1769 keV transition which is also in direct cascade with the 257 keV gamma-ray.

3.6 Beta Singles Analysis

The beta-ray measurements were carried out with a 2" x 2" NE102 plastic scintillator. The detector was placed 3 cm from the charged-wire chamber. The sample chamber window for the beta measurements was 0.25 mil mylar metallized on one side with gold. Prior to the Xe^{138} measurements the detector was tested for gain stability with a Cl^{38} beta source over a counting-rate range of 500 to 3000 counts per second. The detector was found to be stable against counting-rate shifts to within the accuracy of the Fermi-plot end-point determination. The standard beta-sources used for energy scale determinations in the Xe^{138} runs were Y^{90}, Sr^{90}, Y^{91} and Rh^{106}.

A Fermi-plot of a correlated Xe^{138} beta spectrum is shown in Figure 25. It is seen from this plot that the beta spectrum of this isotope has a rather high proportion of low-energy transitions. This may also have been predicted from the singles gamma spectrum of Figure 14 which shows several intense high-energy gamma-transitions. These facts indicate that complications may be expected to arise in the analysis of the beta spectrum due to distortions in the spectrum from the following factors:

1) The occurrence of Compton scattering events in the scintillator due to high-energy gamma rays will lend appreciable contributions to the spectrum.

2) Random beta-summing will be a major problem at the rates required ($\sim$ 2000/sec) in the Xe^{138} experiments because even low intensity summing is not masked in this case by the high energy beta groups.

The correction for gamma-ray Compton background was made for each run simply by repeating the run, but with a 3/8" aluminum beta absorber between source and detector. The counting rates were normalized by means of a gamma-detector which was used to monitor the gamma singles rate.

The random summing contribution could not be minimized by reducing the source activity since it was necessary to record the data in a period not exceeding 15 minutes, due to the Cs^{138} contamination problem. The Cs^{138} beta spectrum shows a moderately intense beta transition of 3.4 MeV. The end-point of the Xe^{138} beta-spectrum was measured to be 2.4 MeV by Nassif and Seelman-Eggebert (25). Careful corrections were therefore necessary to account for the in-growing Cs^{138} beta activity. To account for both the random summing and the Cs^{138} contributions, the beta spectrum was recorded as a function of time. A total of eight spectra were recorded in 4.5 minute periods, (with 0.5 minutes read-out time) beginning immediately after sample injection into the charged-wire chamber. A decay curve of the gross counting rate was also obtained. The Cs^{138} beta spectrum was obtained by counting the activity remaining after the residual xenon activity had been flushed from the chamber. Each of the 'time spectra' was corrected for room background and Cs^{138} contamination. The corrected spectra were then fitted by linear least-squares, channel by channel, to a decay curve with 14 minute and 7 minute components. The 7 minute component is due to the random summing contribution which decays with this 'half-life'. Since random summing is proportional to the square of the counting rate, we have

$$N_{R.S.}(t) \alpha \left(N_o e^{-\lambda t}\right)^2$$

where $N_o e^{-\lambda t}$ is the Xe^{138} counting rate.

Thus,

$$N_{R.S.} \alpha N_o^2 e^{-2\lambda t}$$

$$= N' e^{-\lambda_{R.S.} t}$$

where

$$\lambda_{R.S.} = 2\lambda$$

giving

$$t_{1/2}\ (R.S.) = 1/2\ t_{1/2}\ (Xe^{138})$$

The intensity of both the Xe^{138} and the random summing contribution is shown in Figure 24. A further correction was necessary for gamma background. This was obtained by repeating the run with the beta-absorber in place and carrying out a time-analysis, as above, for the Xe^{138} gamma background contribution. The reduction of the beta spectra data was carried out with the aid of techniques described by Slavinskas et al (53). A Fermi-plot of the corrected Xe^{138} spectrum is shown in Figure 25. The end-point of this spectrum was determined to be 2800 $\pm$ 80 keV. The spectrum was analyzed to obtain the three highest-energy beta groups, β_1-β_3. The end-point energies of these groups and their intensities relative to the total intensity is shown in Table XIII.

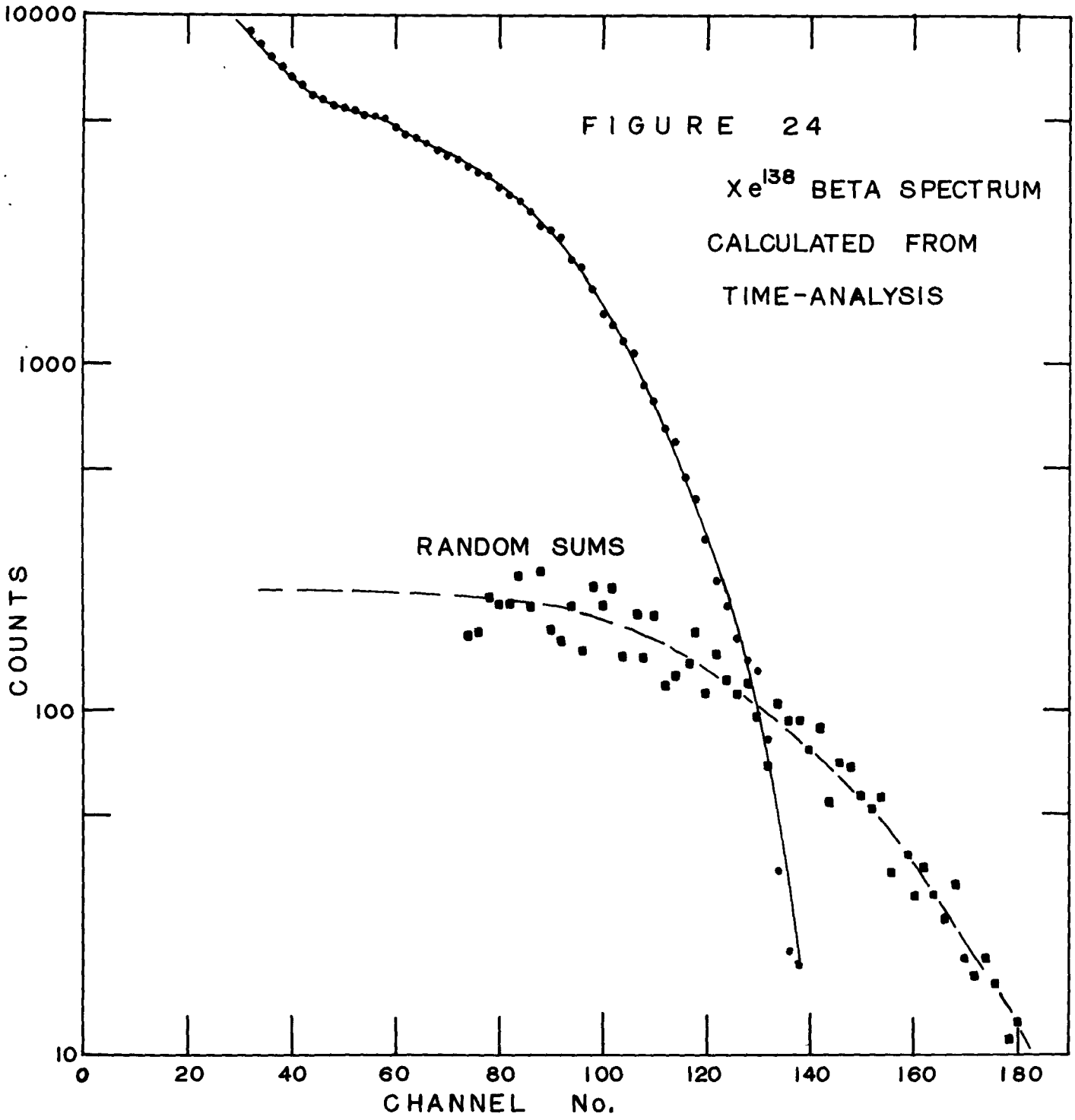

FIGURE 24

Xe^{138} BETA SPECTRUM

CALCULATED FROM

TIME-ANALYSIS

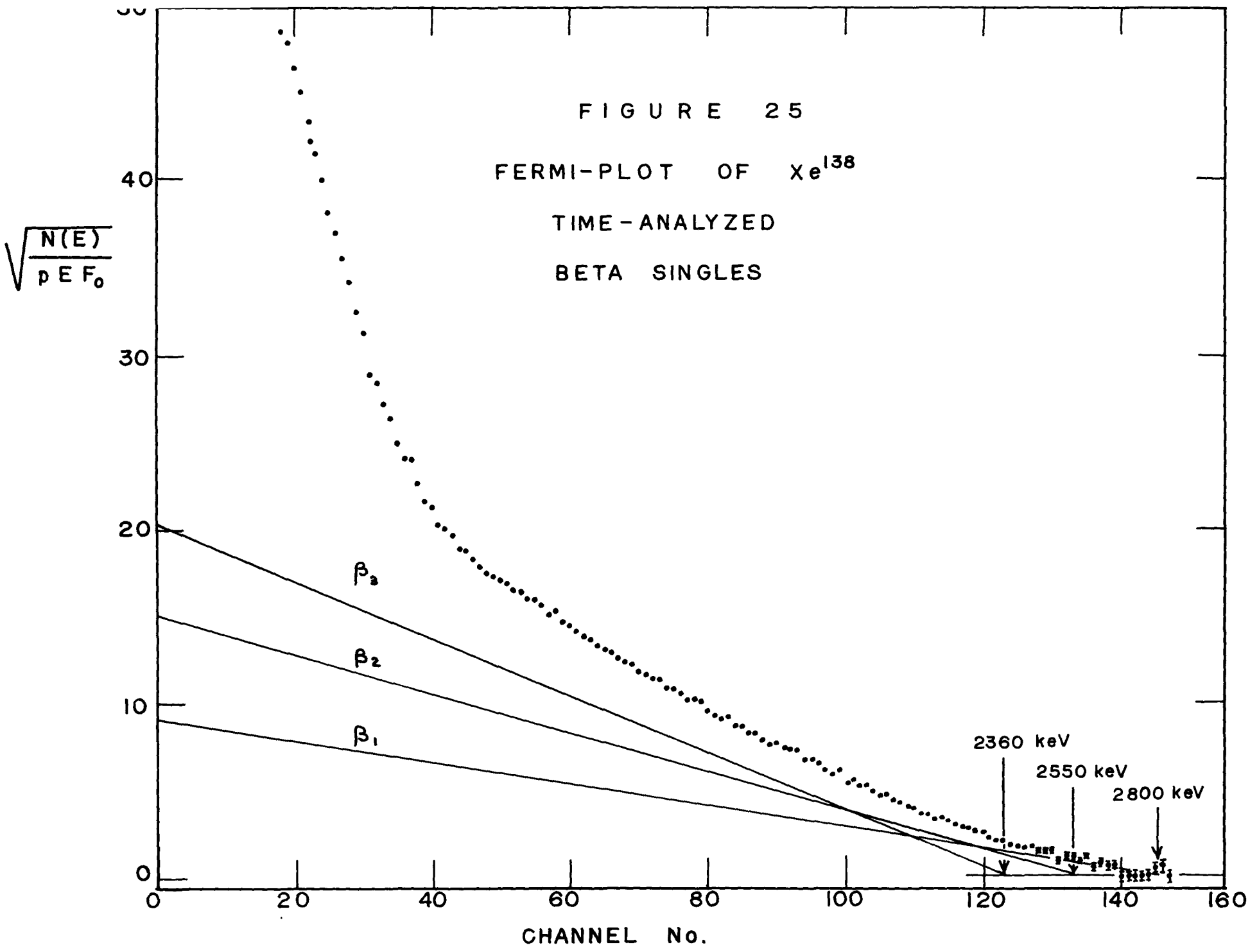
FIGURE 25
FERMI-PLOT OF Xe^{138}
TIME-ANALYZED
BETA SINGLES
$\sqrt{\frac{N(E)}{pEF_0}}$
40
30
20
10
0
β_3
β_2
β_1
2360 keV
2550 keV
2800 keV
0
20
40
60
80
100
120
140
160
CHANNEL No.

TABLE XIII

High Energy Beta Transitions
in Xe^{138}

Group	Intensity Relative to Total β Rate	End-Point (keV)
β_1	6%	2800 ± 80
β_2	13%	2550 ± 80
β_3	22%	2360 ± 50

The low relative intensities and the close spacing of the high-energy transitions does not permit accurate Fermi-analysis of these groups. Therefore the adopted values for these transitions as quoted in Chapter IV are based mainly on the gamma analysis, with the beta-analysis serving only as a check.

The β_1 group indicates a possible unique shape for this transition; however, no definite statement can be made on this point due to the same reasons as outlined above.

3.7 Beta-Gamma Coincidence Measurements

Two-dimensional beta-gamma coincidence measurements were carried out with the plastic scintillator and a 3" x 3" NaI detector. The ND-160 analyzer was used in a 32 x 128 channel configuration. The beta spectra in coincidence with the 32 gamma-"windows" were recorded in the 128 channel groups. Two coincidence experiments were performed, one with the 32 channel gamma-ray window extending from zero to 1000 keV, and a second with the window extending from 1000 to 2600 keV. The beta-energy scale was

determined following the run by recording the Y^{90}, Y^{91} and Sr^{90} standards, and a pulser was also used as a check on the zero-energy channel determination. The gamma background was determined and the spectra corrected for this contamination as before (see section 3.6). The predominant gating of gamma-rays giving rise to each coincident beta spectrum of interest are listed in Table XIV along with the energies and relative intensities determined for the highest-energy beta groups in each case. The intensities quoted are relevant only as comparisons among beta groups for each particular coincidence measurement. The Fermi-plots of these spectra appear in Figures 26 to 29.

TABLE XIV

BETA-GAMMA COINCIDENCE RESULTS

Gating Gamma-Rays (kev)	Beta Group (keV)	Intensity
153	2530	100
	2050	20
257,241	2600	100
	930	75
397,434	2480	100
	1300	5
800-950	1800	30
	1000	100
1050-1150	1350	25
	840	100
1769	860	100
2005-2015	900	100
	780	75

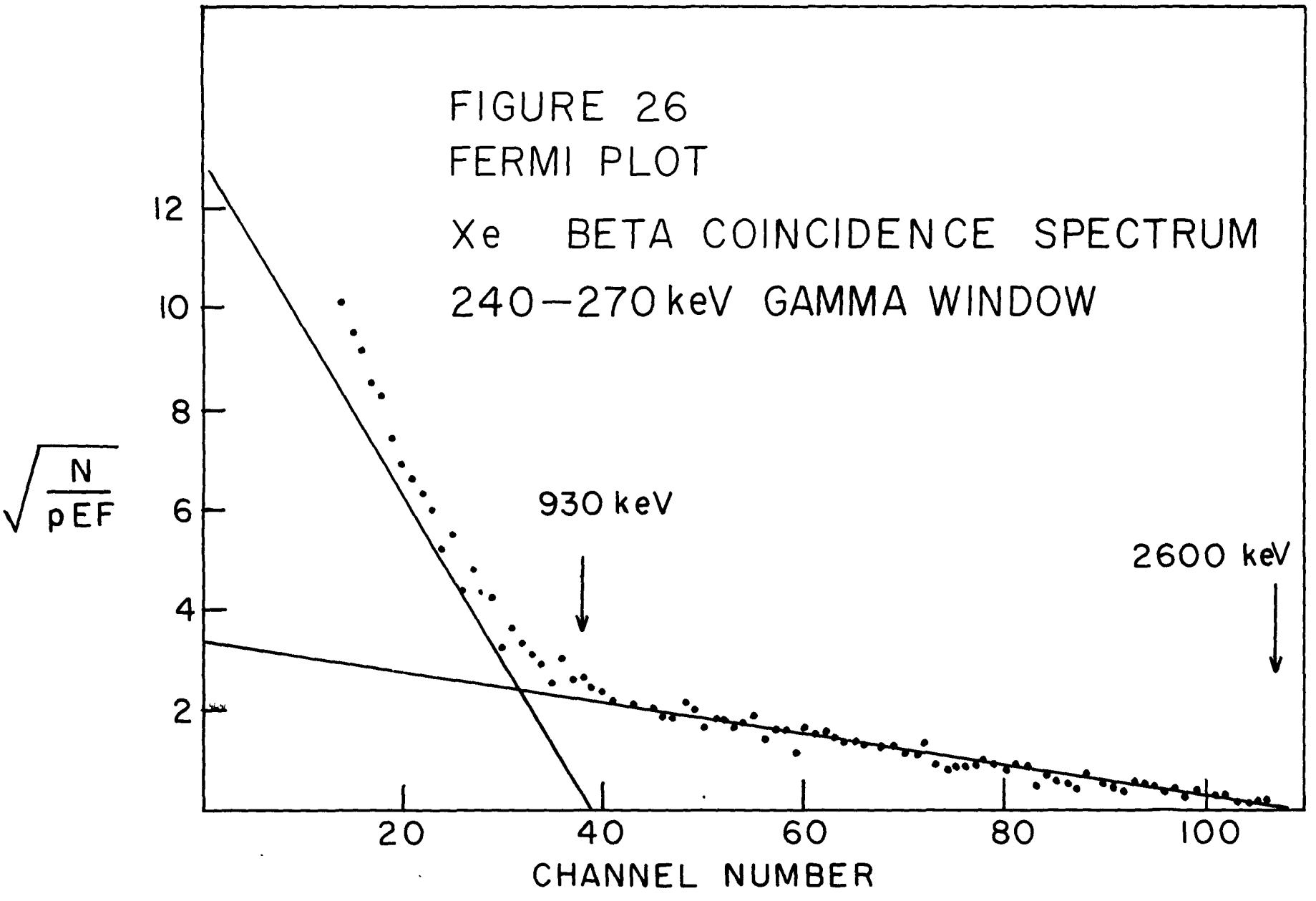
FIGURE 26
FERMI PLOT
Xe BETA COINCIDENCE SPECTRUM
240–270 keV GAMMA WINDOW
$\sqrt{\frac{N}{pEF}}$
12
10
8
6
4
2
930 keV
2600 keV
20
40
60
80
100
CHANNEL NUMBER

FIGURE 27

FERMI PLOT OF BETA COINCIDENCE SPECTRUM

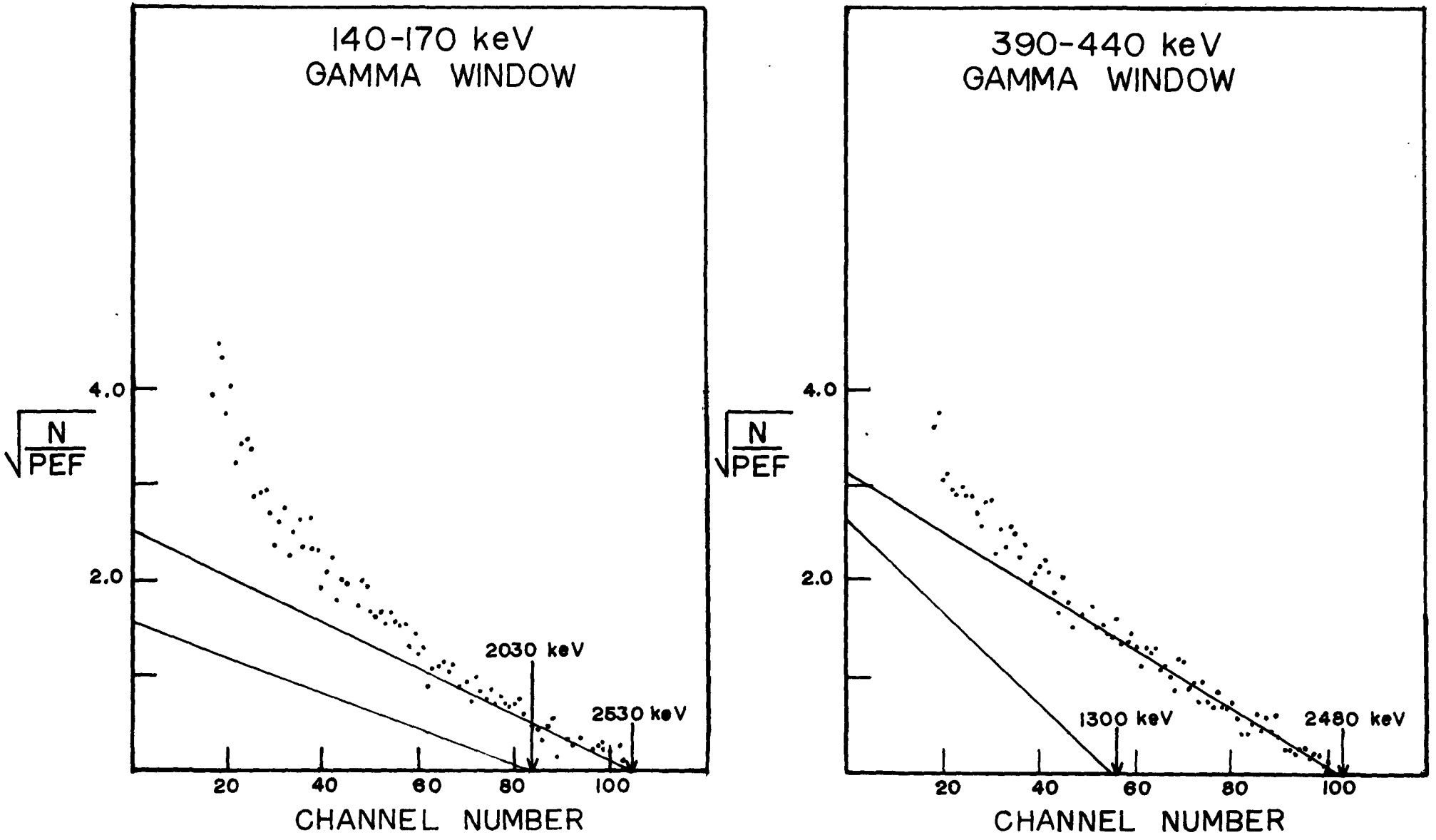

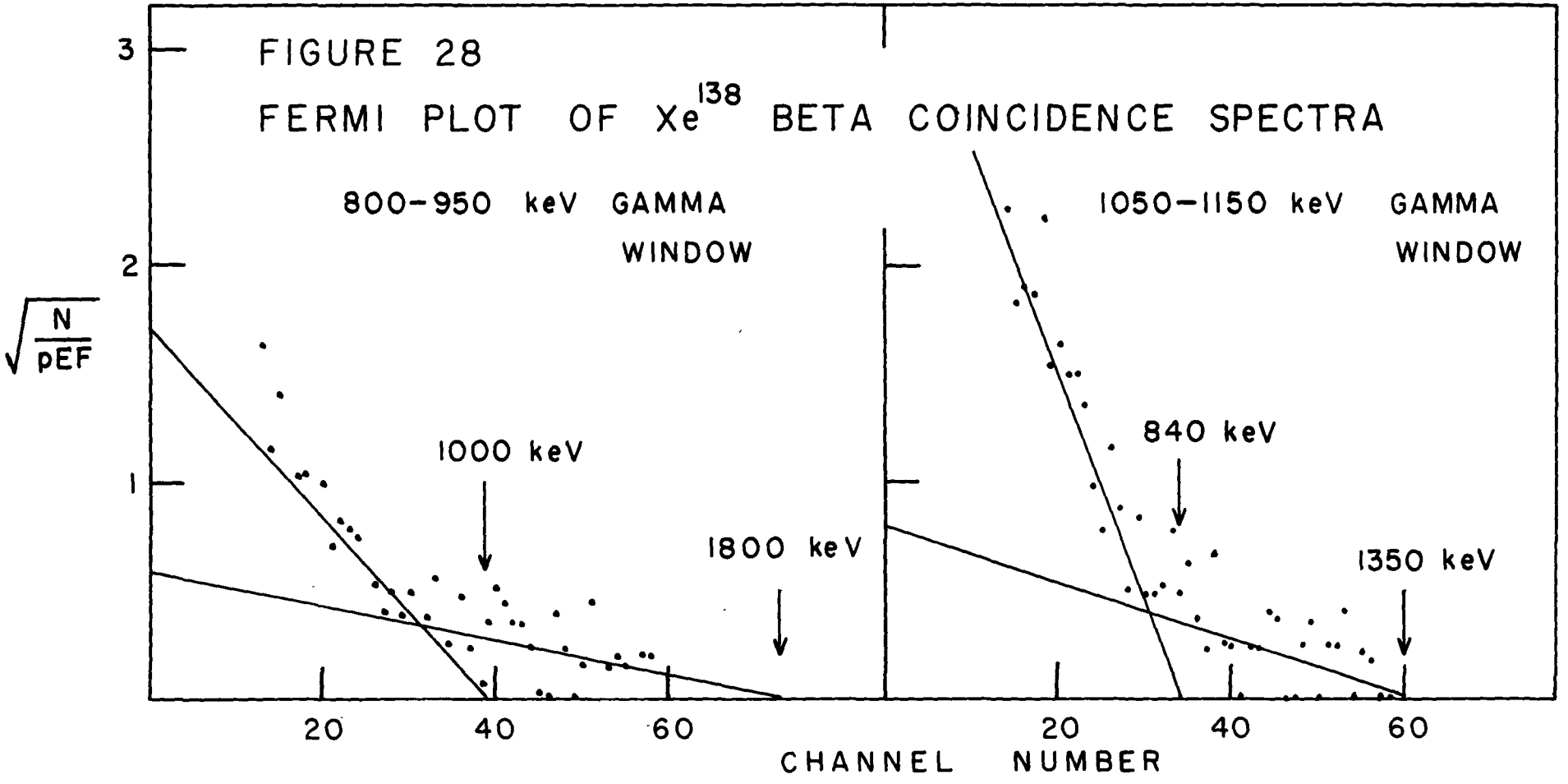
FIGURE 28
FERMI PLOT OF Xe^{138} BETA COINCIDENCE SPECTRA
800-950 keV GAMMA WINDOW
1050-1150 keV GAMMA WINDOW
$\sqrt{\frac{N}{pEF}}$
3
2
1
1000 keV
1800 keV
840 keV
1350 keV
20
40
60
CHANNEL NUMBER

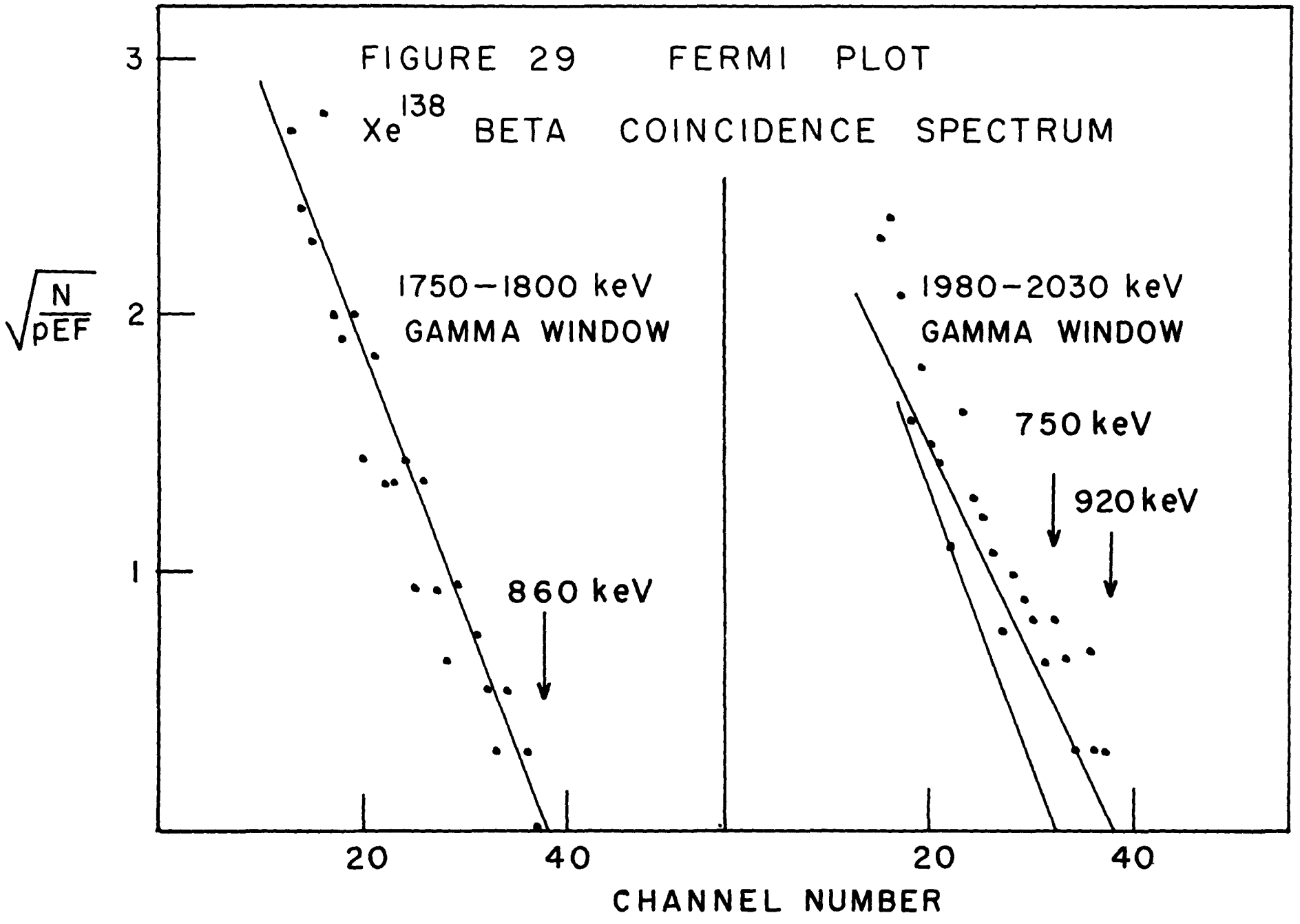
FIGURE 29 FERMI PLOT
Xe^{138} BETA COINCIDENCE SPECTRUM
$\sqrt{\frac{N}{pEF}}$
3
2
1
1750–1800 keV
GAMMA WINDOW
860 keV
1980–2030 keV
GAMMA WINDOW
750 keV
920 keV
20
40
20
40
CHANNEL NUMBER

CHAPTER IV

DISCUSSION OF RESULTS

The decay scheme which is consistent with the experimental results described in the foregoing chapter is shown in Figure 30. The notation used in this illustration is consistent with the notation used in the Nuclear Data Sheets (48). Each beta group is labelled with the transition energy in keV, the percentage branching, and the $\log_{10}$ ft value, respectively. The excited nuclear levels which could not be definitely established from the available information are indicated by dashed lines. The gamma transitions are labelled with identifying numbers which refer to the listing for these transitions in Table IX, P. 46.

Before discussing in greater detail the level structure of the Cs^{138} nucleus a few general remarks should be made on the method of correlating the data from the various measurements. The singles beta measurements were useful in determining the over-all trend of the beta branching and were also used in determining the relative energies of the three highest-energy groups for comparison with the low energy gamma results. The Q-value indicated by the beta measurements and the proposed decay scheme is 2800 $\pm$ 80 keV. The large error assignment is necessary because the intensity of the β_1 transition is of the same order as the β_2 and β_3 intensities and because these transitions are closely grouped in energy. Seeger (54) predicts a Q_β-value of 3500 keV for this nucleus. However, the Way-Wood (48) estimate is 2800. The absorption measurements of Nassif and Seelman-Eggebert (25) gave a beta end-point energy of 2400 keV. It is not expected that they would have seen the low intensity β_1 transition, so that their results are in relatively good

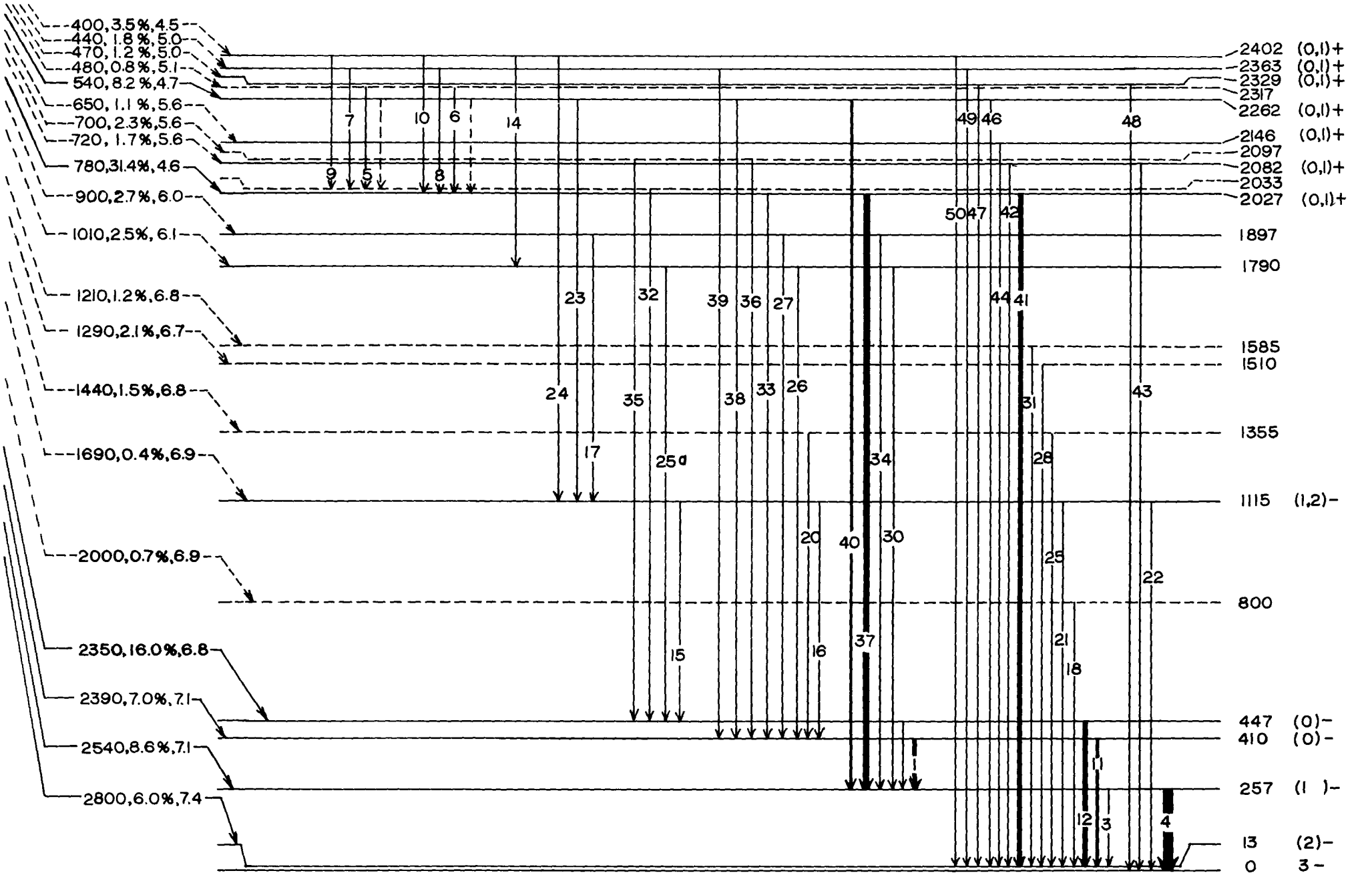

FIGURE 30. XE-138 DECAY SCHEME.

Cs^{138} Levels (keV)

agreement with the present work. The branching indicated for the three high-energy groups from the singles measurement suggests that these groups populate the 13 keV, 257 keV and the (410-447) keV levels respectively (a ground-state beta decay is ruled out in the following discussion).

The beta-gamma coincidence measurements were useful in determining the proper sequence of the more intense gamma-rays in the level scheme. These results confirmed the existence of the two intense beta groups which populate the 2262 keV and 2027 keV levels.

The accurate gamma-energy measurements obtained with the lithium-drifted germanium detector were extremely useful in constructing the level scheme. In many cases, because of the obviously complex level structure of this nucleus, complete reliance on the energy and intensity measurements obtained in this fashion was necessary in order to fit many of the weaker gamma transitions into the scheme. The errors quoted for these determinations in Table IX are in most instances conservative, since the energy balances obtained from these measurements were usually considerably better than the errors would indicate.

The least-squares coincidence-quotient analysis, since it made use of all the available gamma-gamma coincidence data, was of great value in establishing certain cascades including those originating at high energies which populate the 2027 keV level. The values obtained for the coincidence-quotients where weak transitions were involved were subject to large errors, but even the indication of the coincidence in itself was of value in the decay scheme analysis. The coincidence-quotient analysis for the 257 keV transition is expected to be relatively accurate because of the high intensity of this gamma-ray. The analysis of strong transitions in coinci-

dence with this line, according to the values noted in Tables XIIA and XIIB, indicates a beta population of this level relative to the 257 keV line intensity of 20 ± 5 beta transitions per 100 gamma transitions. This is in excellent agreement with the gamma-ray intensity measurements.

The measurements of Langer et al (55) and Bunker et al (39) on the Cs^{138} decay properties indicate that this nucleus does not beta-decay to the Ba^{138} 0^+ ground state, but that there is beta-branching with log ft of 7.6 to the first excited 2+ state. This allows the two possibilities for the Cs^{138} ground-state spin of either 3- or 4- for a first-forbidden beta-decay. Measurements carried out in collaboration with the atomic beams group at this university have definitely ruled out the spin 4 assignment. According to Cohen (18), the low-lying shell model states available for the odd neutron in this nucleus should have odd parity. The lowest-energy neutron state above the N = 82 shell is the $f_{7/2}$ state. The odd proton in the ground-state configuration should be in either the $g_{7/2}$ or $d_{5/2}$ state. There are no low-lying negative parity states above the Z = 50 shell. It is therefore expected that the low energy band of levels as well as the ground state in the Cs^{138} nucleus will exhibit a negative parity. The log ft values for the observed beta decays from the Xe^{138} 0+ ground-state to these levels are in the range 6.8 to 7.4, which also tends to confirm the negative parity assignment.

The highest-energy beta group must decay to the 13 keV level since a beta-transition from Xe^{138} to the Cs^{138} ground state would be 3rd forbidden. The 13 keV level was inferred from energy balances among the intense low energy gamma transitions. The 241 keV transition does not fit well in the location indicated but this may be due to a systematic error

in the 153 keV line energy determination. As stated before, the three high-energy beta groups seen in the singles analysis must decay to at least 3 of the four low-energy states. The spin assignment of the 13 keV level is uncertain, although there is an indication of the unique shape in the β_1 singles transition. Practically all other observed levels in the nucleus decay by gamma-transitions to this level, and high energy transitions from the 2082 keV and 2329 keV levels appear to populate both the 13 keV level and the ground-state. The 13 keV level therefore has a probable spin assignment of 2-.

The 257 keV transition has a multipolarity of either M1 or E2 according to the measured α_K of 0.045 for this transition. The values of α_K quoted by Sliv and Band (8) which are relevant to the 257 keV and 153 keV transitions are listed in Table XV.

TABLE XV

K X-ray Conversion Coefficients

(Values obtained from Sliv and Band (6))

Transition Energy (keV)	Type of Transition	α_K
153	M1	.23
	E1	.058
	M2	1.56
	E2	.31
257	M1	.058
	E1	.014
	M2	.273
	E2	.059

The 153 keV transition exhibits an α_K of $0.11^{+0.10}_{-0.05}$. The uncertainty in this measurement is due largely to the lack of coincidences of this gamma-ray with strong transitions other than the 257 keV gamma-ray which could be used to corroborate the x-ray coincidence measurements. The assignment for this transition is seen from Table XV to be either E1 or M1, but the E1 transition is ruled out by the positive parity requirement. The above multipolarity assignments are in agreement with the measurements of Ovechkin and Demidovich (28). The 257 keV level is populated by a beta-group with log ft of 7.1. Since this state decays strongly to the groundstate a tentative spin assignment of 1 is indicated.

The 410 keV state decays strongly to the 13 keV state and a possible 410 keV transition to the ground-state does not occur or is masked in the solid-state spectrum by a gamma-ray from Cs^{138} of this energy. The log ft for beta decay to this level is 7.1. The indicated spin assignment is 0.

The 447 keV level is similar to the 410 keV level in that it is not observed to decay to the ground state and populates strongly the first excited state. The beta group decaying to this level is seen to have a log ft of 6.8. This state may also have a spin of zero. The beta branching to this level, as to all other levels in the scheme except the 13 keV first state, was calculated from the gamma-ray intensities.

It is interesting to compare the low-energy level structure of Cs^{138} with the La^{140} levels (48). The first four excited levels of these nuclei are shown below.

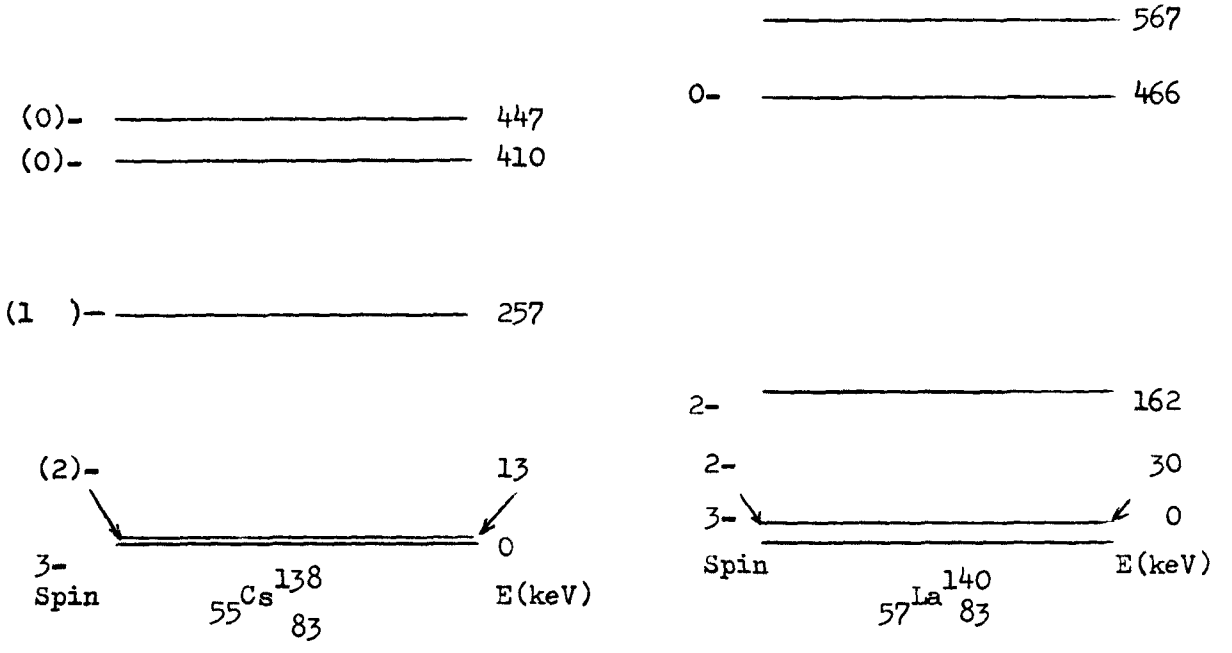

The $_{83}La^{140}_{57}$ nucleus is similar to the $_{83}CS^{138}_{55}$ nucleus in that it has only two more protons which are probably in the same shell, according to shell-model assignments in Preston (1). The spin assignments for the La^{140} nuclear levels might therefore also be true for the corresponding Cs^{138} levels, according to the foregoing discussions.

The 1115 keV level is probably a negative parity level because the gamma intensity measurements infer very little beta population of this level.

The 2027 and 2262 keV levels are populated by beta groups with log ft values well into the range of allowed transitions. Neither level is observed to decay to the ground state. The positive parity assignments to these levels is therefore strongly indicated. The positive parity assignments indicated for other levels in the high energy band are again based on the log ft values.

The low-energy transitions occurring among levels of the high-energy

level band is indicative of a strong relation among the participating levels, since these levels would otherwise decay almost completely to the low-energy states. In order to obtain the positive parity levels in this region one may consider two possible nuclear configurations. The first possibility is that an octupole phonon may couple with the ground-state configuration to give positive-parity low spin states in the high-energy region. Hansen and Nathan (56) have shown the octupole excitation in the region of the Cs^{138} nucleus to have an energy of approximately 2 MeV. One should expect enhanced E3 transitions from such states and this may explain the existence of the (2135-2146) and the (2069-2082) keV doublets which are believed to decay from the 2146 and 2082 keV levels to the 13 keV level and the ground state respectively. However, the beta-population of such octupole configurations may be expected to be hindered.

A second possibility is that the odd neutron may occupy the $i_{13/2}$ level. This would provide a positive parity by coupling to the positive parity proton which would lie in either the $d_{5/2}$ or $g_{7/2}$ state. However, the minimum spin of such a coupled pair would be 3. This discrepancy could be removed by breaking a proton pair and coupling the three unpaired protons to the odd neutron. The excitation energy requirements of this scheme appear to be large. The $i_{13/2}$ configuration lies approximately 3 MeV above the $f_{7/2}$ neutron state (18), and the proton pairing energy, according to Pal and Mitra (57), is 1.6 MeV. However, it is difficult to estimate the energies which would be involved in the actual odd-odd configuration.

APPENDIX I

THE MATHEMATICAL FORMULATION OF DATA REDUCTION BY LEAST SQUARES

I.1 Introduction

The past decade has seen a marked improvement in electronic devices which are utilized in the measurement and recording of nuclear radiation data. This has resulted in a corresponding improvement in the accuracy of these measurements and also in an increase in the speed at which data may be accumulated. Particular examples of such apparatus now being used in nuclear decay scheme analysis would include large-memory multi-parameter analyzers, fast analog-to-digital converters, and electronic gain stabilizers. These devices also make possible the study of short-lived radioisotopes since more highly active samples may be used, allowing data acquisition in a shorter length of time.

The accumulation of data from experiments applied to decay scheme studies may now require much less of the experimenter's time than does the subsequent reduction of data. Older methods of data analysis, for example spectrum-stripping and graphical decay curve analysis, are time consuming; neither do they take fully into account the statistical nature of the data. For these reasons a great deal of effort is being expended by nuclear physicists in developing computer programs to be applied to the analysis of such data.

The method of least-squares has been almost universally applied to

nuclear data reduction by computer. In the present work, least-squares programs were developed and used extensively in the analysis of gamma-ray scintillation spectra and in the reduction of decay-curve data. The following sections outline the least-squares procedures which were used and also some of the limitations inherent in these procedures. The "parabolic" least-squares method is also investigated in detail and specific examples are given to show the applicability of this technique in data reduction.

I.2 The Method of Least-Squares

In general the mathematical model $\underline{S}$, which one desires to fit to experimental data is given in matrix notation by

$$\underline{S} = F(\underline{Y},\underline{B}) \qquad \text{(I.2.a)}$$

If $\underline{S}$ is linear in $\underline{B}$ then (I.2.a) may be written as

$$\underline{S} = \underline{Y}\,\underline{B} \qquad \text{(I.2.b)}$$

Here, $\underline{Y}$ is the design matrix and $\underline{B}$ is the vector of estimates with p components for the p unknown parameters. The method of least-squares requires the minimization of X^2, where

$$X^2 = (\underline{M} - \underline{S})^T \underline{W}(\underline{M}-\underline{S}) = \text{min.} \qquad \text{(I.2.c)}$$

Here, X^2 is the sum of weighted deviations,

$\underline{M}$ is the vector of measurements and

$\underline{W}$ is the (diagonal) weighting matrix.

If the measurements m_i are normally and independently distributed and $\underline{S}$ is linear in $\underline{B}$, then the least-squares estimates $\bar{b}_i$ of the elements of $\underline{B}$ are both maximum likelihood and minimum variance un-

biased estimates. In this case, also, the individual weights w_{ii} are given by

$$w_{ii} = 1/\sigma_i^2$$

Here, σ_i is the standard deviation of the measurement m_i.

For normally distributed m_i the quantity X^2 is the well-known figure of merit "chi-squared". If the number of degrees of freedom f is defined as

$$f = n-p$$

where n is the number of data points, then X^2/f has a mean value of 1 with a standard deviation of $(2/f)^{\frac{1}{2}}$ for normally distributed data.

Minimization of (I.2.c) implies

$$\frac{\partial X^2}{\partial \underline{B}} = 0 \qquad \text{(I.2.d)}$$

Each row of the matrix (I.2.d) is one of the so-called normal equations.

The value of X^2 and $\underline{B}$ which satisfy (I.2.d) will be denoted by $\bar{X}^2$ and $\underline{\bar{B}}$ respectively, where $\underline{\bar{B}}$ is the least squares vector of estimates and $\bar{X}^2$ is the minimum value of X^2.

If $\underline{B}$ enters equation (I.2.a) in a linear fashion, then the solution for $\underline{\bar{B}}$ subject to (I.2.d) is straightforward, resulting in

$$\underline{\bar{B}} = (\underline{Y}^T \underline{\underline{W}} \underline{Y})^{-1} \underline{Y}^T \underline{\underline{W}} \underline{M} \qquad \text{(I.2.e)}$$

For convenience we shall redefine

$$(\underline{Y}^T \underline{\underline{W}} \underline{Y})^{-1} = \underline{C}$$

where $\underline{C}$ is the correlation matrix. The variance of any element of

$\bar{\underline{B}}$ is given by the corresponding diagonal element in $\underline{C}$

$$\text{Var}\,(\bar{b}_j) = c_{jj}$$

The covariance between any two elements of $\bar{\underline{B}}$ is given by

$$\text{Cov}(\bar{b}_j, \bar{b}_i) = c_{ji}.$$

The standard deviations of the $\bar{b}_j$ are

$$(\bar{b}_j) = \left\{ c_{jj} \cdot x^2/f \right\}^{1/2} \qquad \text{(I.2.f)}$$

In a great many applications, such as in the determination of half-lives from decay-curve data, the analysis of Gaussian experimental curves, etc., $\underline{B}$ does not enter (I.2.a) in a linear fashion. Under this condition it is necessary to modify the least-squares procedure. The usual approach to this problem is to expand $\bar{\underline{S}}$, as a function of the parameters which are to be found, in a Taylor series about $\underline{S}$.

Equation (I.2.a) may then be expressed as:

$$\bar{\underline{S}} = \underline{S} + (\bar{\underline{B}} - \underline{B}) \frac{\partial \underline{S}}{\partial \underline{B}} + \frac{1}{2} (\bar{\underline{B}} - \underline{B})^2 \frac{\partial^2 \underline{S}}{\partial \underline{B}^2} + \text{----}$$

If $\left| \bar{\underline{B}} - \underline{B} \right|$ is small enough (that is, if $\underline{B}$ is close enough to the least-squares solution, $\bar{\underline{B}}$) then second and higher-order terms may be neglected. If $\underline{S}$ is linear in $\underline{B}$ then second-and higher-order terms are identically zero and one obtains $\bar{\underline{B}}$ by the use of equation (I.2.e) as before. However, $\underline{B}$ may be made up of a combination of both linear and non-linear components.

For non-linear components β_j one has

$$\bar{s}_j = s_j + \Delta\beta_j \frac{\partial \underline{S}}{\partial \beta_j} \qquad \text{(I.2.g)}$$

This, in effect, adds the new parameter $\Delta\beta_j$ to be determined in a linear fashion. An iterative approach may now be made to the problem. It is necessary, however, to provide initial estimates for all the $\bar{\beta}_j$ which are to be determined. The values for the $\Delta\beta_j$'s are then determined along with the linear parameters b_j. The $\bar{\beta}_j$ are then adjusted by

$$\bar{\beta}_j = \bar{\beta}_{j(n-1)} + \Delta\beta_{j(n)}$$

The entire calculation is carried out repeatedly until all the $\Delta\beta_j$ become negligible. This method is often referred to as the Gauss-Seidel method and is a standard approach in the solution of non-linear least-squares problems. However, the method has certain limitations.

1. It may be noted that, even though the b_j enter equation (I.2.a) in a linear manner, original estimates are required of these parameters if they are present in the expression for the first derivative of any non-linear component (see equation I.2.g). Such linear parameters are then treated in the same fashion as the non-linear parameters.
2. The first derivative of a function may be much more complex than the function itself, and thus more difficult and time-consuming to generate.
3. In certain circumstances, especially with mathematical models which are sets of nearly similar functions, it may be difficult to arrive at reasonable original estimates of the parameters, both linear and non-linear, which are to be found. If the original estimates are poor, the iterative method may either

diverge or converge to an incorrect solution.

In this context it may be noted that there are certain types of problems which have non-unique solutions (i.e. X^2 has more than one minimum). It is impossible to determine the uniqueness of the solution from the iterative method.

When $\underline{S}$ is not linear in at least one of the parameters it generally is not true that X^2 is a chi-squared distribution. The estimates σ_i of the precision of the parameters $\bar{\beta}_i$ are not exact in this case. Further, there is no way of showing that minimum residual in the non-linear model implies maximum likelihood and minimum variance as with the linear treatment. However, according to Moore (R1), it is common practice, in fitting non-linear parameters, to treat X^2 in this case as if it had the same properties as in the linear model, although this is not a mathematically rigorous result.

I.3 The Parabolic Method of Least-Squares

The "parabolic" method of least-squares has in the past received a fair amount of use, for example references (R2, R3, R4). However, the author has found no investigation of the mathematical basis for this method in the current literature.

Since it overcomes a to a certain degree the objections to the Gauss-Seidel technique described above, the method has been carefully investigated. After the development of a satisfactory mathematical model, the method was used successfully in the analysis of decay-curve data and also in the fitting of the Xe^{138} gamma-ray

scintillation spectra. The results of these analyses are given in Chapter III of this thesis.

As a starting point, let us develop further the linear least-squares problem where, as in equation (I,2.b), $\underline{S} = \underline{Y}\,\underline{B}$. Equation (I.2.c) may be written as

$$X^2 = (\underline{M}-\underline{S})^T\underline{W}(\underline{M}-\underline{S})$$

$$= (\underline{M}-\underline{YB})^T\underline{W}(\underline{M}-\underline{YB}) \qquad \text{(I.3.a)}$$

Also, $\bar{X}^2 = (\underline{M}-\underline{Y}\bar{\underline{B}})^T\underline{W}(\underline{M}-\underline{Y}\bar{\underline{B}})$ where $\bar{X}^2$ and $\bar{\underline{B}}$ are defined as before. Now, from (I.2.e),

$$\underline{C}^{-1}\bar{\underline{B}} = \underline{Y}^T\underline{WM}$$

Expanding (I.3.a) we obtain

$$X^2 = \underline{M}^T\underline{WM} - (\underline{C}^{-1}\bar{\underline{B}})^T\underline{B} - \underline{B}^T\underline{C}^{-1}\bar{\underline{B}} + \underline{B}^T\underline{C}^{-1}\underline{B}$$

Similarly

$$\bar{X}^2 = \underline{M}^T\underline{WM} - (\underline{C}^{-1}\bar{\underline{B}})^T\bar{\underline{B}} - \bar{\underline{B}}^T\underline{C}^{-1}\bar{\underline{B}} + \bar{\underline{B}}^T\underline{C}^{-1}\bar{\underline{B}}$$

$$= \underline{M}^T\underline{WM} - (\underline{C}^{-1}\bar{\underline{B}})^T\bar{\underline{B}}$$

Therefore, $X^2 - \bar{X}^2 = (\underline{B}-\bar{\underline{B}})^T\underline{C}^{-1}(\underline{B}-\bar{\underline{B}})$ (I.3.b)

Now it is desired to study the behaviour of equation (I.3.b) as a given element b_m of the vector $\underline{B}$ is varied in a region localized about $\bar{b}_m$.

The $b_j (j \neq m)$ are the dependent variables and, according to Whittaker and Robinson (R5), vary as

$$(b_j - \bar{b}_j) = \frac{c_{mj}}{c_{mm}}(b_m - \bar{b}_m) \qquad \text{(I.3.c)}$$

Here c_{mj} and c_{mm} are as defined before.

Of course, if the covariance c_{mj} were zero then b_j could hardly be classed as a dependent variable. In least-squares calculations involving non-orthogonal functions, however, c_{mj} is not identically zero.

The dependence of $(X^2 - \bar{X}^2)$ on the variable $(b_m - \bar{b}_m)$, may be established in a simple analytical form in the following manner.

For convenience we define new variables $a_i = (b_i - \bar{b}_i)$

Then from (I.3.c)

$$a_j = \frac{c_{mj}}{c_{mm}} a_m \qquad \text{(I.3.d)}$$

and similarly for a_i.

Now $\underline{A}^T \underline{C}^{-1} \underline{A}$, ($\equiv$I.3.b), is of the form

$$\sum_{ij} a_j c^{-1}_{ji} a_i = X^2 - \bar{X}^2$$

Substituting the relationships of equation (I.3.d), we get

$$= \sum_i \sum_j \left\{ \frac{c_{mj}}{c_{mm}} a_m c^{-1}_{ji} \right\} \frac{c_{mi} a_m}{c_{mm}}$$

$$= \sum_i \left\{ \sum_j (c_{mj} c^{-1}_{ji}) c_{mi} \right\} \frac{a_m^2}{c_{mm}^2}$$

$$= \sum_i \delta_{mi} c_{mi} \frac{a_m^2}{c_{mm}^2}$$

Converted back to the original variables, this becomes;

$$X^2 - \bar{X}^2 = (b_m - \bar{b}_m)^2 / c_{mm} \qquad \text{(I.3.e)}$$

Stated literally, equation (I.3.e) shows that, in the region localized about $\bar{b}_m$, X^2 is a parabolic function of $(b_m - \bar{b}_m)$ with the coefficient of the equation being given by the reciprocal of the variance in $\bar{b}_m$; hence the term "parabolic method".

The standard deviation in $\bar{b}_m$ is again given by (I.2.f).

Before any further discussion it is important to note that the analysis thus far has concerned only linear parameters of the least-squares fit. The parameters b_j in equation (I.3.c) behave as dependent variables only by virtue of the condition $\frac{\partial X^2}{\partial b_j} = 0$ (for all $j \neq m$) which is satisfied at each point by carrying out the least-squares fit.

The transition to non-linear least-squares may now be made. It is necessary only to recall equation (I.2.g). This truncated expansion is exact for linear parameters and is a good approximation for non-linear parameters which are in the neighborhood of the least-squares values for these parameters. This condition may be specified by

$$\left| \beta_m - \bar{\beta}_m \right| < \epsilon_m \qquad \text{(I.3.f)}$$

where ϵ will be determined by certain factors including the similarity between various components in the design matrix. The value of ϵ for particular applications described in this appendix will be discussed later.

Differentiation is necessary between the cases of applying the parabolic method to:

1) Any number of linear parameters b_m and only one non-linear parameter β_m, and
2) Any number of linear parameters combined with any number of non-linear parameters.

(i) When there is only one non-linear parameter to be found, then the foregoing analysis is exact and may be immediately

applied to the calculation of β_m by varying the parameter.

The procedure for the calculation is as follows. First, the "normal" equations are set up for the linear parameters. It is necessary only to supply the computer with an estimate of the non-linear parameter. The standard least-squares fit is then carried out and X^2 is calculated. β_m may then be given a new value $\beta_m + \Delta$. The least-squares fit is repeated. If X^2 has increased, the next value of β_m to be used should be $\beta_m - \Delta$ in order to approach a final solution by the minimization of X^2.

Repetition of this process will eventually bring X^2 through a minimum value. If the initial value of β_m was close to the least-squares value $\bar{\beta}_m$ then three calculations are sufficient to accurately determine the location of the minimum.

The parameters $\bar{X}^2$, $\bar{\beta}_m$ and C_{mm} may now be found by fitting equation (I.3.e) to the three points closest to the minimum in the X^2 curve. These results satisfy the least-squares criterion of minimum residual (I.2.d) and therefore $\bar{\beta}_m$ is the least-squares solution for the non-linear parameter.

The parabolic method as applied to the solution for one non-linear parameter is shown graphically in figure A1.

(ii) If it is necessary to solve for more than one-linear parameter, the procedure is much the same as in the foregoing paragraphs. However, it is now necessary to vary each non-linear parameter in turn so as to minimize X^2. A "cycle" of

FIGURE A1.

SOLUTION FOR ONE PARAMETER BY THE PARABOLIC METHOD.

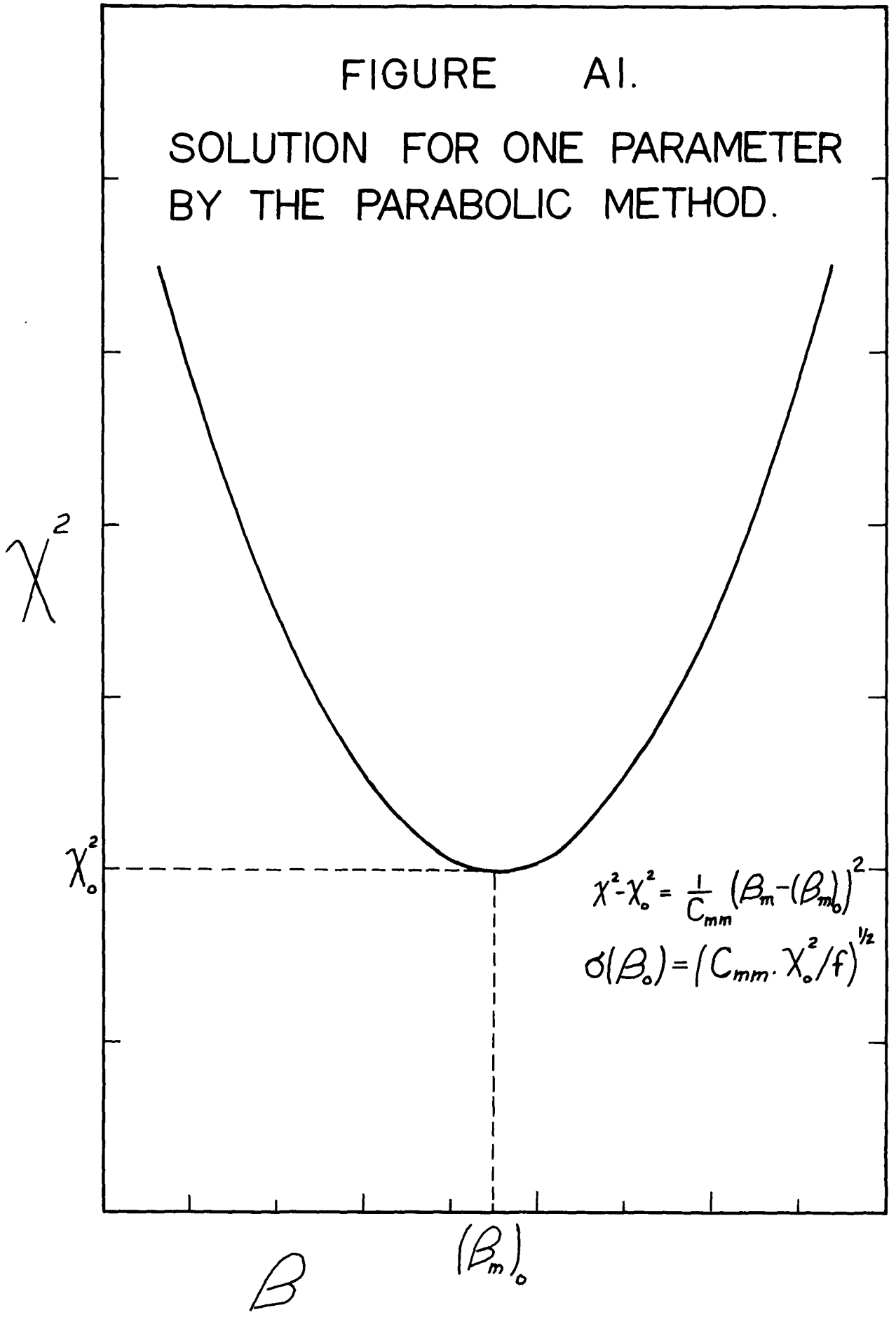

calculations might be defined as minimizing X^2 with respect to each non-linear parameter in turn, ranging from the first parameter β_1 to the k-th parameter where there are a total of k non-linear parameters. The X^2_{min} obtained through varying the m-th parameter in the j-th cycle will be referred to as $X^2_{m,j}$. The resulting value for the corresponding parameter will be referred to as $\beta_{m,j}$. The minimization procedure may have to be carried through several complete cycles, depending upon the accuracy of the original guessed values, before the $\beta_{m,j}$ converge to the least-squares solutions, $\bar{\beta}_m$.

In the case of more than two non-linear parameters, although least-squares solutions are obtained through the above procedure, the error estimates are not obtained according to the parabolic model without excessive calculations. This is due to the fact that non-linear dependent variables are not automatically required to satisfy equation (I.2.d) by the use of the normal equations, as are the linear dependent variables.

However, in the case of two non-linear parameters, the error estimates may be obtained by carrying through four cycles of calculation. For each calculation cycle, the value of each parameter as it is fixed gives a value for X^2_{Min} which is the value obtained by the following minimization of X^2 with respect to the remaining parameter. Four calculation cycles will give three values of X^2 for three values of each parameter. These values may be fitted to obtain the parabolas in a similar fashion as for the case of only one non-

linear parameter.

An extension may be made to the above procedure in the case of more than two non-linear parameters. Although the result is not mathematically correct, it has been found, with some restrictions, to be a good approximation. Let us assume, as before, that there are k non-linear parameters to be determined. Then the general approximation is that if $X^2_{m,j}$ is the minimum value of X^2 obtained by varying the m-th non-linear parameter in the j-th cycle thus obtaining a corresponding value $\beta_{m,j}$ for the parameter, then the values as indicated below should be used in the calculation of the error.

Non-Linear Parameter	Value	Corresponding X^2 Min.
β_1	$\beta_{1,j}$, $j = 1,2,3$	$X^2_{k,j}$, $j = 1,2,3$
$\beta_m (m \neq 1)$	$\beta_{m,j}$, $j = 1,2,3$	$X^2_{m-1,j+1}$, $j = 2,3,4$

In practise it has been found that if the ratio of covariance to variance between any two non-linear parameters (see equation (I.3.c) is less than approximately 20% , then the final error estimate is quite reasonable. The limitations inherent to the method are discussed in section I.4.

I.4 Application of the Parabolic Method to Analysis of Decay-Curve Data and Gamma-Ray Scintillation Spectra

The application of the parabolic method to decay-curve analysis is not difficult. The mathematical model $\underline{S}$ which one desires to fit to the data is of the form;

$$s_j = \sum_{i=1,3,--}^{n} a_{ie}^{-\lambda_i t_j} + \sum_{1=2,4--}^{n+1} a_i (e^{-\lambda_i t_j} - e^{-\lambda_{i-1} t_j})$$

at each data point j.

Here a_i is the intensity of the parent or daughter isotope,

λ_i $(i = 1,3 - ..n)$ is the decay constant of the i-th parent isotope

λ_i $(i = 2,4 ---n + 1)$ is the decay constant of the i-th daughter isotope which grows in from the decay of the (i-1)th parent.

t_j is the time at which the counting rate m_j was recorded.

The normal equations are easily derived and the least-squares fitting procedure is straightforward. Initial estimates are required of all the λ_i. However, if the contribution of any particular component to the counting rate is relatively low throughout the experiment, then the decay-constant of that isotope should be determined in another experiment in which its intensity would predominate. The decay-constants for such isotopes should remain fixed during the present analysis. The least-squares determination of the decay-constants and the error analysis are as described in section I.3. The determination of a decay-constant which has a value within approximately 15% of the value of any other decay constant is usually impossible without the use of external constraints

since in such cases the intensity a_i may tend to go to negative values.

The parabolic fit as applied to gamma-ray scintillation spectra is carried out in a similar fashion to the above procedure, although the design matrix $\underline{R}$ is far more complex and difficult to construct.

Here, $\underline{S}$ is given at each channel j by;

$$s_j = \sum_{i=1}^{n} a_i r_i (E_i, E_j)$$

where a_i is the intensity of the i-th gamma ray component, and $r_i (E_i, E_j)$ is the response of the detector to the i-th gamma-ray having photon energy E_i, at the energy E_j corresponding to the j-th channel.

The dependence of r_i upon E_i and E_j is described in detail in Appendix II . In this case the non-linear parameters are the E_i, which therefore play the same role in scintillation spectra analysis as do the λ_i in decay curve analysis.

Limitations of the Parabolic Method

Considerable experience has been gained in the present work in the application of the parabolic technique to specific problems. The following observations may be made on the limitations inherent in the method.

1) Since the non-linear parameters have usually converged closely to the least-squares estimates following the fourth cycle, the values obtained for these parameters during the fourth cycle should be retained as the least-squares estimates.

Due to rounding errors in the calculations, the values obtained for the least-squares estimates when fitting to obtain the error estimates are often somewhat inaccurate.

2) The covariance between any two non-linear parameters will be large when the responses described by these parameters are nearly similar. The least-squares estimates obtained by the minimization are, in general, quite reasonable but the error estimate may be incorrect because of the approximations made.

3) The initial estimates supplied for the non-linear parameters should be close enough to the least-squares solutions so that the calculations are not perturbed through the presence of what could be considered (if the initial value was poor) a non-existent parameter. Here again, convergent least-squares solutions may be obtained, but the error estimates will usually not be correct. If error estimates are required, and if the final estimates are incorrect, then error estimates will be obtained by recalculating the fit using as initial guesses the least-squares values found in the first calculation.

A rule of thumb which has been used for half-life determinations by decay curve analysis is that

$$\epsilon_m < 0.05\, \bar{\lambda}_m$$

where ϵ is defined by equation (I.3.f).

It is usually very simple in practise to estimate the location of the photo-peaks in gamma-ray spectra to within one channel. Little difficulty has therefore been encountered in obtaining error estimates of these data.

I.5 Goodness-of-Fit Criteria Applied to Data Analysis

There are many good references available on least-squares techniques. Those which have proven to be of greatest assistance in the present work include works by Guest (R6) and Linnik (R7).

There are three meaningful criteria which have been found useful in this work in testing the validity of the mathematical model. These criteria are based upon the values calculated for:

1) X^2 (Chi-squared),

2) the standard deviations, σ , of each parameter, and

3) the differential weighted residuals, d_i at each data point.

The following discussion indicates the manner in which these quantities may be used in testing the model formulation.

1) Pearson's (R8) chi-squared test is probably the test most universally applied to statistically meaningful calculations. This test states that, for a large number of degrees of freedom f, X^2 should be normally distributed with an expectation of f. That is, over a number of individual measurements, X^2 should have a mean value of f. The variance of X^2 is 2f.

X^2 therefore serves as an indication of:

i) The appropriateness of the mathematical model and

ii) whether or not systematic deviations are present in the data.

The ability to distinguish between these causes requires a certain amount of experience. In the present case, f is often of the order of 200 and p is moderately large between (10 and 20). X^2 is usually not very sensitive to the presence or absence of low intensity parameters in calculations of this type. Therefore

use must be made as well of the following more sensitive indicators.

2) Information is also obtained from the least-squares error estimate in the determination of each parameter. An empirical test which is often used is, that if the error is as large as the value of the parameter, then the portion of the model designated by that parameter should be discarded. A more sophisticated guage is Student's t-test (R9) which will determine the statistical significance of the departure of the parameter from a value of zero.

3) The over-all indication of goodness-of-fit is determined by the X^2 test. However, it has been found that non-statistical deviations which are unaccounted for in the mathematical formulation of $\underline{S}$ tend to increase X^2/f, very often to a value of 2 or greater, although the fit may actually be very good otherwise. The criterion which will serve as a check for goodness-of-fit in this case is the evaluation of weighted residuals, $\underline{D}$, where:

$$d_i = (s_i - m_i)/m_i^{\frac{1}{2}}$$

Here, $\underline{D}$ is evaluated at the i-th data point where s_i is the calculated least-squares value and m_i is the measured value. If the values of d_i from point to point seem to show a random distribution about zero, with few numbers greater than one, then the fit may in general be considered satisfactory, regardless of whether or not the X^2 test so indicates. Systematic variations observed in $\underline{D}$ also give an indication of further revisions which are necessary in the mathematical model $\underline{S}$.

Taken as a combination these three criteria have proven to be relatively accurate guide-lines to completeness of the least-squares fit.

APPENDIX II

THE RESPONSE OF NaI(Tl) SCINTILLATION DETECTORS TO GAMMA RADIATION

II.1 Introduction

Three distinct processes contribute to the absorption of gamma-rays in a sodium-iodide detector. These are the photo-electric effect, the Compton effect, and pair-production. The relative cross-sections of these processes are a strong function of the incident photon energy. The photo-electric process predominates at low energies (0-300 keV), the Compton process at intermediate (300-7000 keV) energies, and pair production at high energies ($>$ 7000 keV). The solid line in Figure A2 shows the response S(E') one would obtain from 2 meV photons in a finite NaI crystal, based on the relative absorption cross-sections. Line functions are shown which correspond to the photo-effect and to pair-production with the escape of one and two annihilation gamma-rays, respectively. The line function at 511 keV corresponds to pair production in sorrounding materials, with subsequent absorption of an annihilation photon in the detector. The other non-continuous contributions correspond to the Compton effect and back-scatter. The actual pulse height distribution R(E) which would be obtained results from the convolution of the detector resolution G(E',E) with S(E') so that

$$R(E) = \int_0^{E_0} S(E')G(E',E)\, dE'$$

FIGURE A2.

APPROXIMATE RECOIL-ELECTRON ENERGY DISTRIBUTION.

ABSORPTION OF 2000keV PHOTONS IN A 3"x3" NaI CRYSTAL, WITH NO MULTIPLE COMPTON EVENTS.

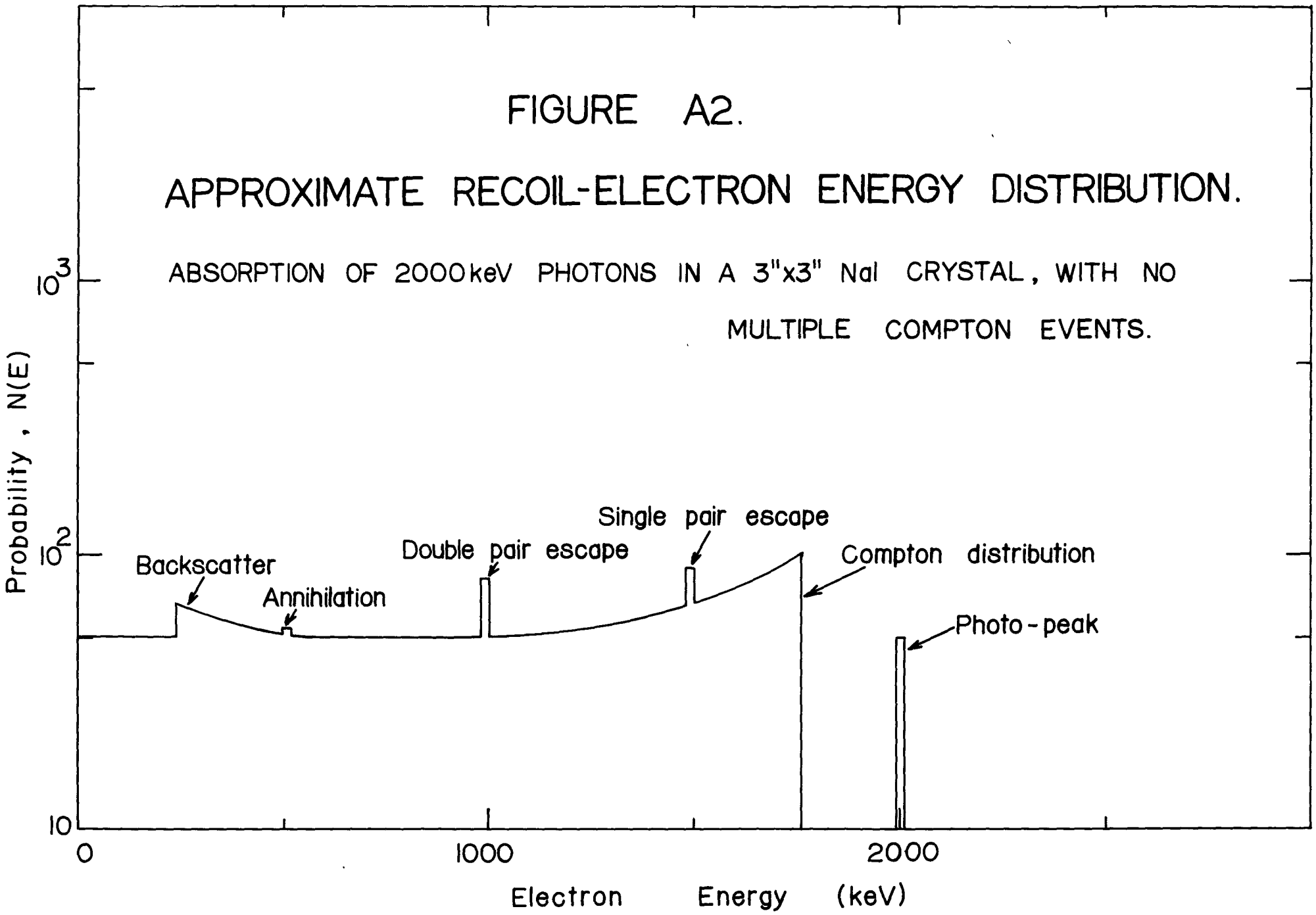

This response is shown as the dashed line in Figure A3 . The experimentally observed response is shown as a solid line in the figure. The disparity between these two curves is caused by multiple summing events in the detector and by the non-linear pulse height-energy response of the detector. Since the difference between these two curves arises in a very complicated manner it is very difficult to obtain an analytical description of the detector response. Since the detector response is energy dependent, one should consider the response surface

$$R(E,E_o) = \int_o^{E_o} G(E,E') S(E',E_o) dE'$$

where E_o is the incident photon energy. Zerby and Moran (R10) and Miller and Snow (R11) have calculated the NaI response surface by the use of Monte Carlo techniques. However, the use of such an approach for the generation of a library of response functions is impractical, since the experimental geometry (which may vary considerably for different experiments) affects the detector response in a complex fashion. Another approach to the problem of scintillation spectra analysis is by the use of iterative unfolding techniques. Such techniques have thus far proven to be of limited use in the analysis of complex spectra because of mathematical instabilities encountered in such solutions (R12).

The alternative approach to the generation of the response surface is to obtain a set of experimental parameters which adequately describe the response surface over the range of interest.

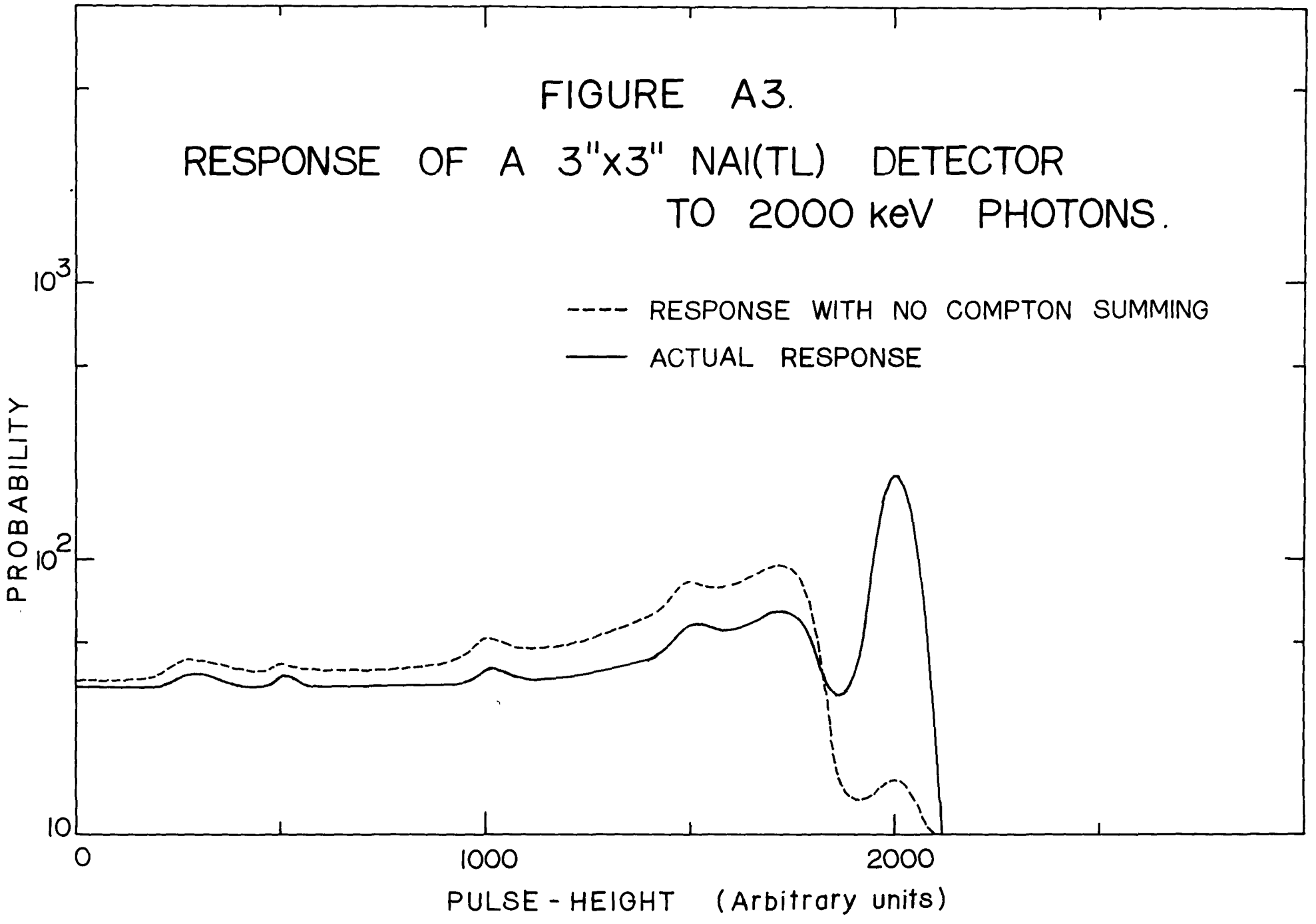
FIGURE A3.
RESPONSE OF A 3"x3" NAI(TL) DETECTOR
TO 2000 keV PHOTONS.
RESPONSE WITH NO COMPTON SUMMING
ACTUAL RESPONSE
PROBABILITY
10^3
10^2
10
0
1000
2000
PULSE - HEIGHT (Arbitrary units)

Interpolation techniques may then be used to calculate response functions at the desired energies. Methods embodying this technique have been developed by various authors (R13 ,R14). Heath et al (R14,R15) have developed such a method in great detail. Since the fitting of experimental data in this work required the generation of a large number of detector response functions, and since the empirical procedures just described are relatively fast, the use of these methods was strongly indicated.

In order to simplify the response generation program, the present work deviated considerably from that previously reported. The main emphasis was placed upon obtaining a good analytical representation of the photo-peak, since the photo-peak portion of the response has a more observable effect on least-squares residuals than the remainder of the response. The remainder of the detector response was simply defined in a numerical fashion. Following sections will describe in detail the methods developed for the generation of response functions and the application of these methods in the least-squares fitting program.

II.2 Obtaining and Using Suitable NaI(Tl) Response Functions

The analysis of complex scintillation spectra may be visualized as being separated into distinct problems. First, it is necessary to obtain standard line shapes (response functions) which effectively blanket the energy range of interest. Secondly, these response functions must be put in some form in which manipulation either analytically or numerically is possible. The remaining problem is

to generate and fit response functions of the required energy to the scintillation spectra to be analyzed.

II.2.1 Obtaining Standard Line Shapes

It has been mentioned before that the use of computers in data reduction places more stringent requirements on the experimental conditions. A given set of line shapes may be used for the analysis of data from many experiments. It therefore is obvious that the requirements of instrumental stability and reproducibility must be satisfied to a high degree throughout the recording of the line-shapes and throughout subsequent experiments. The majority of the more important conditions to be observed in recording line shapes are summed up in a check-list shown in Table A I. The appropriate details are discussed below.

1) It is necessary to correct the line-shape data for summing since a number of the standards used are short-lived, requiring a counting-rate which produces an objectionable amount of random summing. Certain of the standards (e.g. Cl^{38}) decay by gamma-cascade. The summing correction will also include coincident sums from the cascade.

2,3) The gain of the detection system may be varied (within limits) to suit the gamma-energy of the standard. It is well known that the absolute photo-peak resolution of NaI detectors varies approximately as $\sqrt{E_o}$ where E_o is the incident gamma-ray energy. To obtain the same amount of detail in each standard and at the same time to avoid distortion due to the detection system, the photo-peak is set at a channel position which

varies as $\sqrt{E_o}$. Over-all gain change is usually accomplished by varying the gain of the linear amplifier, except for very high energy or very low energy lines where it may also be necessary to vary the photo-multiplier voltage. Figure A4 shows a comparison of absolute photo-peak widths obtained from a Cr^{51} spectrum recorded at different gains obtained in turn by varying either the photo-multiplier voltage or the amplifier gain. The methods are shown to be equivalent. However, a plateau exists for the detector over which the detector resolution is essentially constant with photo-multiplier voltage. The voltage should be kept well within these limits.

4) The major portion of gain instability arises in the photo-multiplier. For swiftly decaying sources gain stabilization is a practical necessity, and is accomplished by an analog device which compensates for gain changes by appropriate adjustments of the high voltage. For longer-lived sources no gain stabilization is found to be necessary, providing the system is allowed to "settle down" before data recording begins. Zero and gain shift in the analyzer and gain shift in the amplifier have been found to be negligible over the short periods encountered in recording line shapes.

5) The analyzer zero is kept constant throughout the recording of standards in order that an appropriate correction may be applied later. The analyzer linearity correction (see section II.3.1 is determined only once, and indications are that this linearity correction will not change for pulse height zero

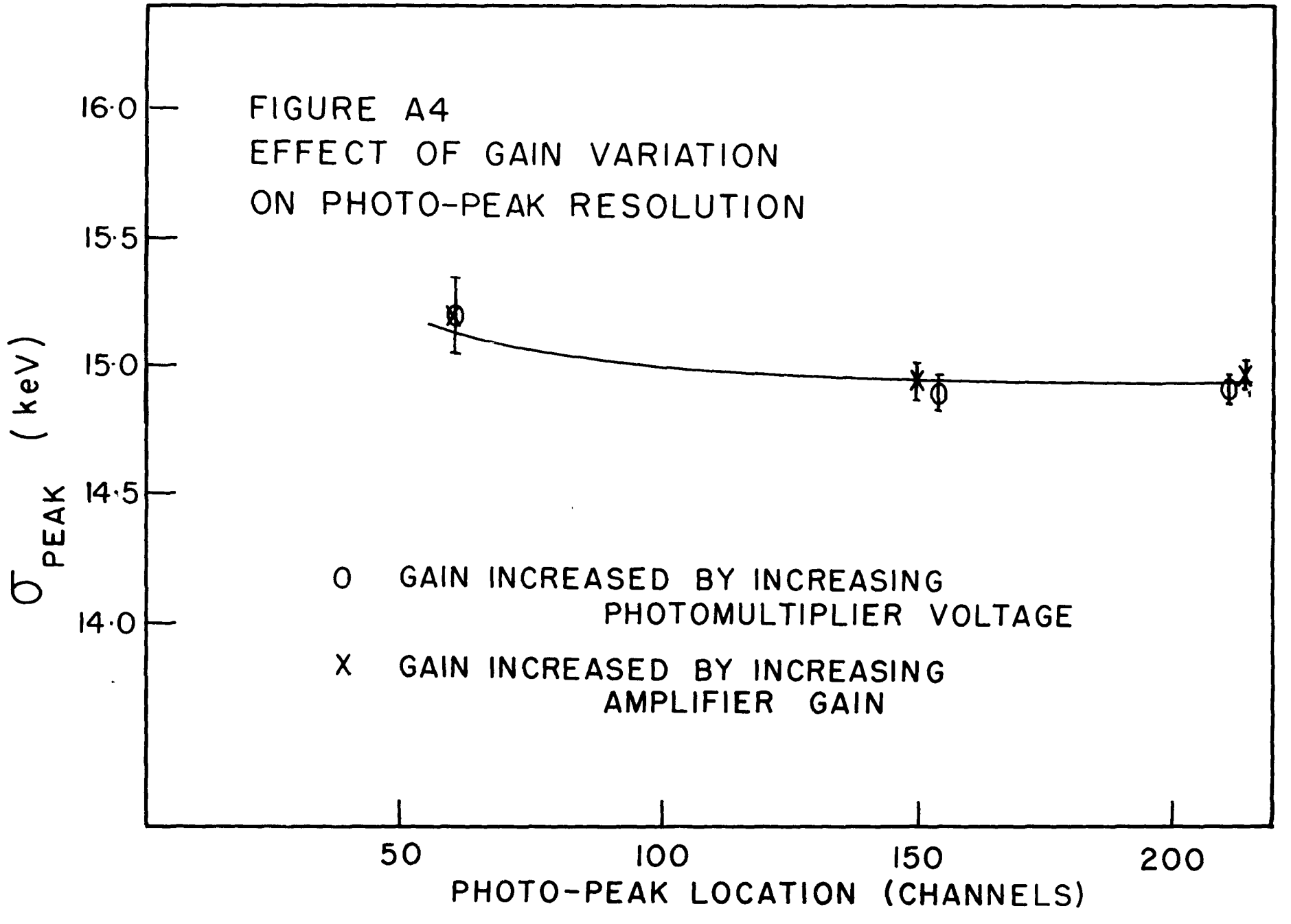
FIGURE A4
EFFECT OF GAIN VARIATION
ON PHOTO-PEAK RESOLUTION
16·0
15·5
15·0
14·5
14·0
σ PEAK (keV)
O GAIN INCREASED BY INCREASING PHOTOMULTIPLIER VOLTAGE
X GAIN INCREASED BY INCREASING AMPLIFIER GAIN
50
100
150
200
PHOTO-PEAK LOCATION (CHANNELS)

TABLE AI

CHECK-LIST FOR LINE SHAPE RECORDING

	Item	Comments
1	Summing, background	Recorded and subtracted from data.
2	System Gain	Varied (usually with linear amplifier) so photo-peak location $\alpha\sqrt{E_o}$
3	Photo-multiplier H.V. Supply	Kept well within plateau limits (700 - 950 volts)
4	Gain Stabilization	Photo-multiplier gain stabilized with "Spectrostat" H.V. supply
5	Geometry	Same as experimental geometry
6	Analyzer zero	Zero pulse height kept within ~5 channels of zero channels.
7	Analyzer ramp	Same as experiment

changes which are kept within about five channels of channel one. However, from experience with a similar analog-type zero suppressor used in a window amplifier, the analyzer linearity correction would be expected to be a function of the zero setting outside this range.

Radio-isotopes used for standards were selected whenever possible to have simple decay schemes. A minimum of correction to the line shape will then give the desired mono-energetic response function. The standards used are listed in Table A II. The Xe^{133} x-ray listed was not used as a standard, but was necessary for checking the evaluation of photo-peak parameters.

II.2.2 The Calculation of the Sodium Iodide Response Surface

The initial preparation of the sodium iodide line standards for analysis requires a certain amount of hand smoothing. This is especially necessary in the low energy portion, where interference from bremsstrahlung and x-rays tend to mask the Compton contribution of the gamma-ray. The Compton upturn at very low energies was neglected, and the gamma-standard in this region was given a constant value which was extrapolated from the higher energy continuum.

All remaining corrections were made by computer manipulation of the data. The portion of the line-shape from zero-energy to a point one photo-peak half-width below the photo-peak mean was smoothed using a seven-point cubic polynomial. The remainder of the photo-peak was fitted to an analytical expression by non-linear least squares techniques. The form of the analytical function which

TABLE AII

Line Shape Standards

Nuclide	Gamma Energy (keV)
Xe^{133} (X-ray)	30
Xe^{133}	81
Ce^{141}	145
Ba^{139}	166
In^{114}	192
Hg^{203}	279
Cr^{51}	320
Au^{198}	412
Cu^{64}	511 ($\beta+$)
Cs^{137}	662
Mn^{54}	835
Cu^{66}	1045
Zn^{65}	1114
Na^{22}	1280
V^{52}	1440
La^{140}	1600
Al^{28}	1780
Cl^{38}	2150
Thorium ore (Bi^{205})	2600
Na^{24}	2755
S^{37}	3100

accurately describes the photo-peak is discussed in detail in the following section.

II.2.3 The Analytical Function Describing the Sodium Iodide Photo-Peak

A probability plot of the Cs^{137} photo-peak is shown in Figure A5. The form of this curve suggests that the photo-peak might be represented by a Gaussian, given by

$$f(x) = A \exp\left(-(x - x_o)^2/2\delta^2\right) \qquad \text{(II.2.3.a)}$$

Here, A is the peak height

x_o is the mean peak position and

δ is the peak width parameter

In order that δ as used in this description will not be confused with other standard expressions for peak "width", it should be noted that δ is related to the "full-width at half maximum" (FWHM) by

$$FWHM = 2\delta\sqrt{2\ln 2} = 2.355\ \delta$$

δ will be referred to in this work as the "width".

A noticeable deviation from linearity in the probability plot of Figure A5 indicates that a considerable deviation from a Gaussian form begins to occur below a point approximately one peak-width below the mean. This has been shown by Heath (R 16) and others to be mainly a result of small-angle scattering in the source and in the beta-absorber. A non-linear least-squares fit of a Gaussian to a Cs^{137} photo-peak over the indicated "Gaussian region" is shown in Figure A6. Obviously the Gaussian is a rather poor approximation to the photo-peak, since X^2/f for this fit is 64.5.

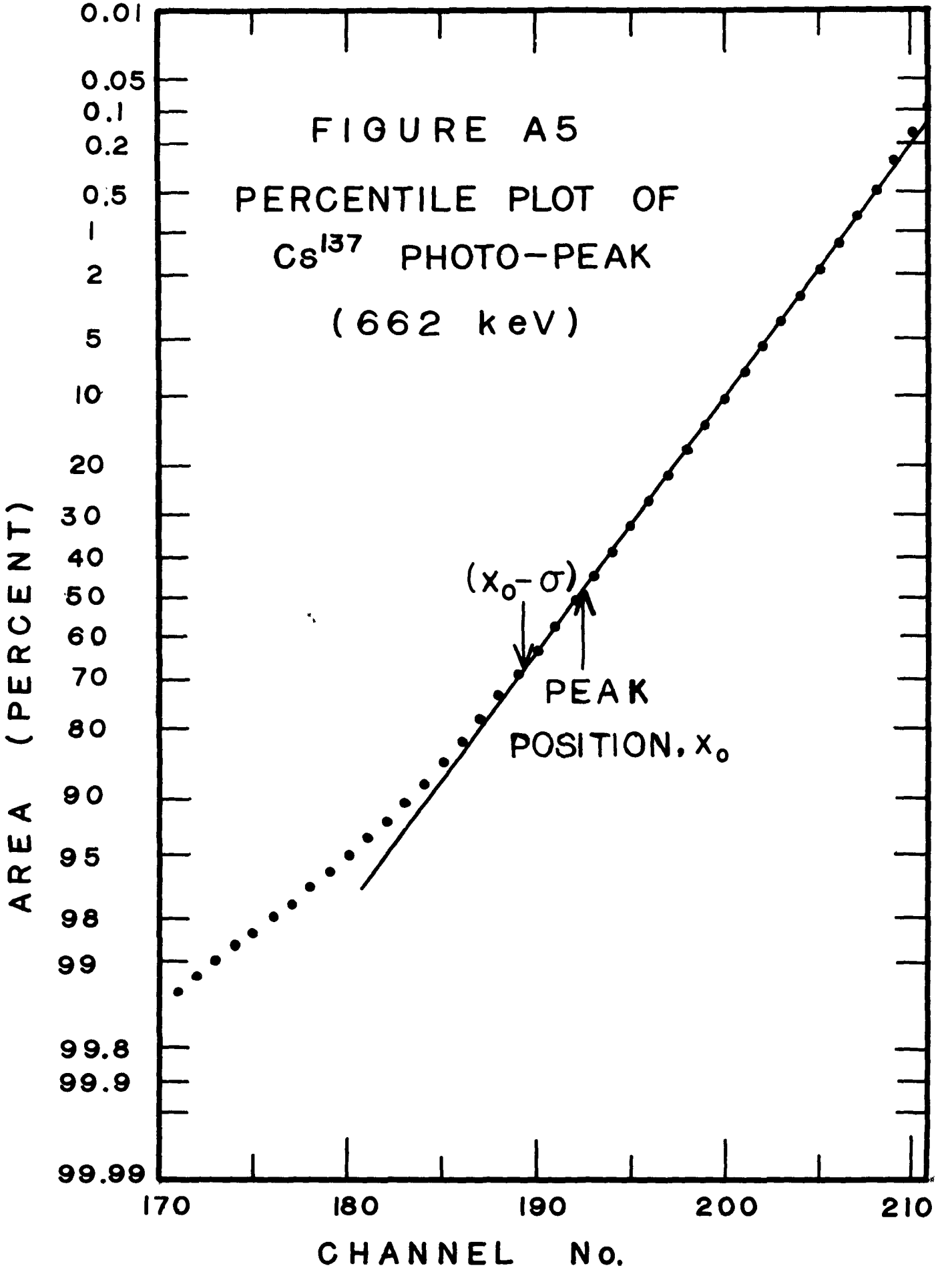
FIGURE A5
PERCENTILE PLOT OF
Cs137 PHOTO-PEAK
(662 keV)
(X0-σ)
PEAK
POSITION, X0
AREA (PERCENT)
0.01
0.05
0.1
0.2
0.5
1
2
5
10
20
30
40
50
60
70
80
90
95
98
99
99.8
99.9
99.99
170
180
190
200
210
CHANNEL No.

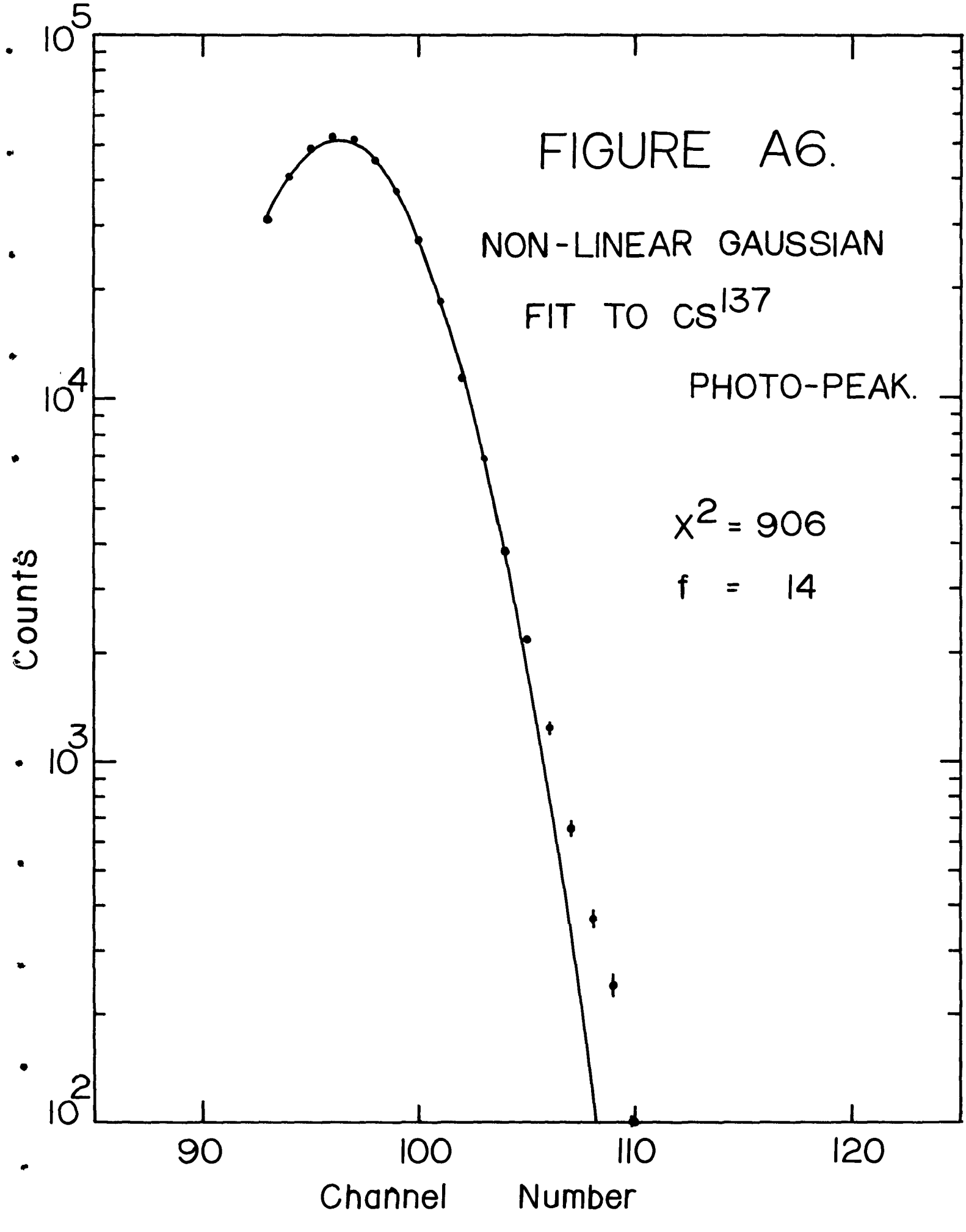
FIGURE A6.
NON-LINEAR GAUSSIAN
FIT TO CS137
PHOTO-PEAK.
X2 = 906
f = 14
Counts
10^5
10^4
10^3
10^2
90
100
110
120
Channel Number

Helmer and Heath (R17) have found that a function of the form

$$f(x) = A \exp\left(-(x - x_o)^2/2\delta^2\right)\left\{1 + \alpha_1(x - x_o)^4 + \alpha_2(x - x_o)^{12}\right\}$$

is very good approximation to the high energy portion of the photo-peak. If a series of photo-peaks for different gamma-ray energies are recorded on the same energy scale, they have found that α_2 plotted on a log-log scale against peak position falls roughly on a straight line. However, α_1 tends to follow a less uniform curve on the same type of plot. $\alpha_1(E_o)$ and $\alpha_2(E_o)$ are therefore indicated to be rather complicated parameters for use in interpolation.

A search was undertaken in the present work to find an analytical description of the photo-peak which would require parameters that were relatively insensitive to photo-peak energy.

The Exponentially-Adjusted Gaussian Photo-Peak Function

Since the eventual determination of parameters which were not sensitive to photo-peak energy or pulse-height was required, a dimensionless pulse height function was used, and denoted by

$$T = \left|x - x_o\right| / \delta\sqrt{2} \qquad \text{(II.2.3.b)}$$

The functional description of the photo-peak is given by

$$f(x) = A \exp(-T^u) \qquad \text{(II.2.3.c)}$$

For a Gaussian function, u=2. Since the photo-peaks have been shown to be non-Gaussian in shape, then u might be expected to have the form

$$u = u(E_o, T)$$

where E_o refers to the incident gamma-ray energy.

The functional form of u which most adequately described the photo-peak was found to be

$$u = B \exp(CT) \qquad \text{(II.2.3.d)}$$

Hence the term "exponentially-adjusted Gaussian". Here, B and C are functions of E_o only. The Gauss-Seidel least-squares technique (see Appendix I) was used to fit photo-peaks of energy 30 keV to 3100 keV to this function. The parameters of the fit were A,B,C, x_o and σ. The strong convergence of the fit and the reasonable values obtained for X^2/f showed that (II.2.3.c) subject to (II.2.3.d) is a good approximation to the photo-peak shape. The peaks were fitted over the range of x from $(x_o - \delta)$ on the low energy side to a point on the high energy side where the photo-peak had fallen to approximately 0.1% of maximum height. A comparison of the fits obtained for the "exponentially-adjusted Gaussian" with those obtained with the standard Gaussian and with the Helmer-Heath method is shown in Table A III . The values of B and C as functions of photo-peak energy are shown in Figure A7 . These plots indicate that B is a constant-valued function. To determine the validity of this assumption, the photo-peaks were again fitted to the exponentially-adjusted Gaussian, but subject to the constraint that B = constant. A determination of B by the parabolic method was carried out. The resulting values of X^2 as a function of B are shown in Table A IV . The parameters of the least-squares fit are interdependent to a certain degree. Therefore, C can be expected to change when the constraint $B = B_o$ is imposed. The new plot of C obtained under these conditions is shown in Figure A8 . Also, δ^2 as a function of energy is shown in Figure A9 . According to Breitenberger (R18) the width of the ideal photo-peak should vary according to the relationship

$$\delta^2 = A_1 E + A_2 E^2$$

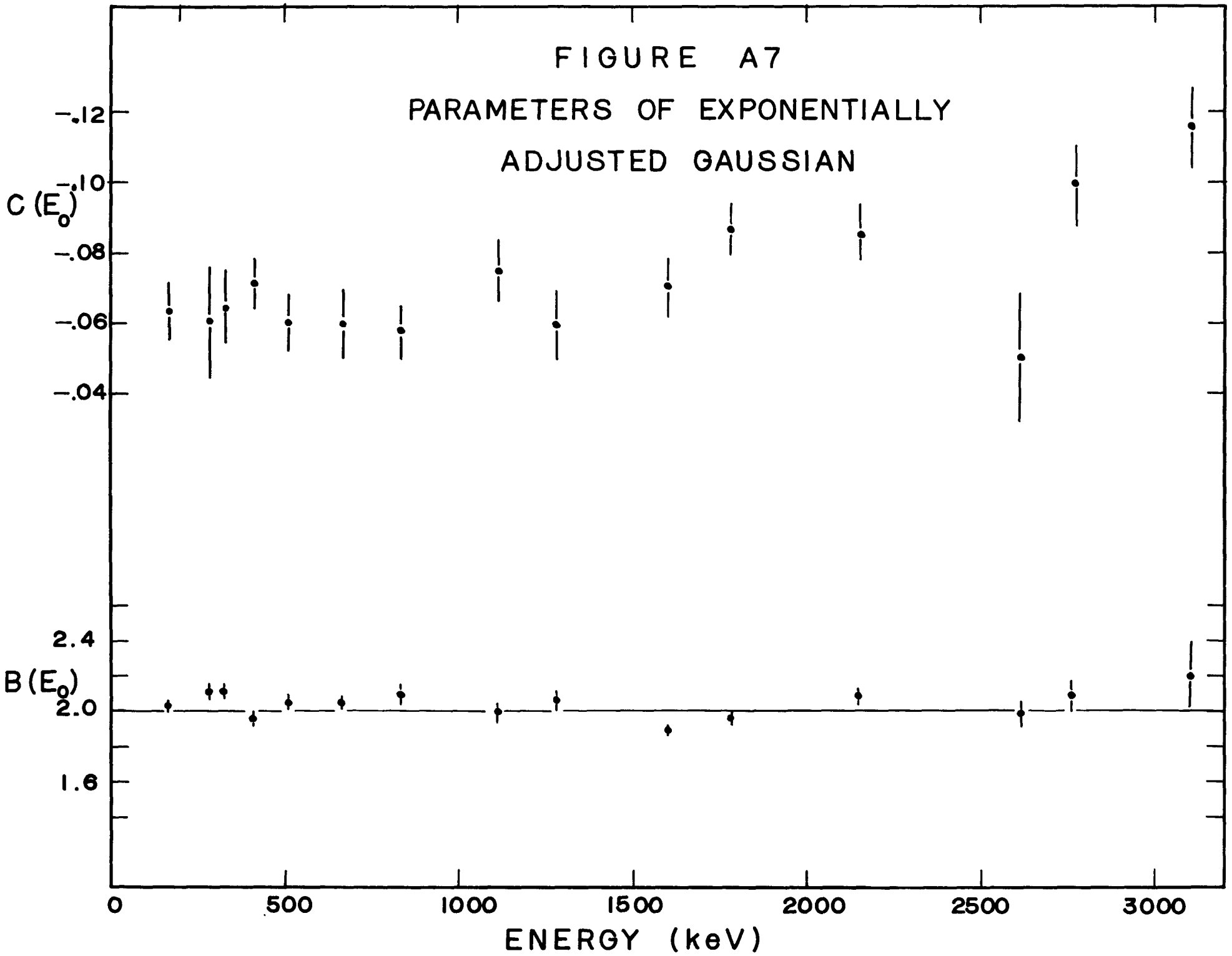
FIGURE A7
PARAMETERS OF EXPONENTIALLY
ADJUSTED GAUSSIAN
C (E0)
-.12
-.10
-.08
-.06
-.04
B(E0)
2.4
2.0
1.6
0
500
1000
1500
2000
2500
3000
ENERGY (keV)

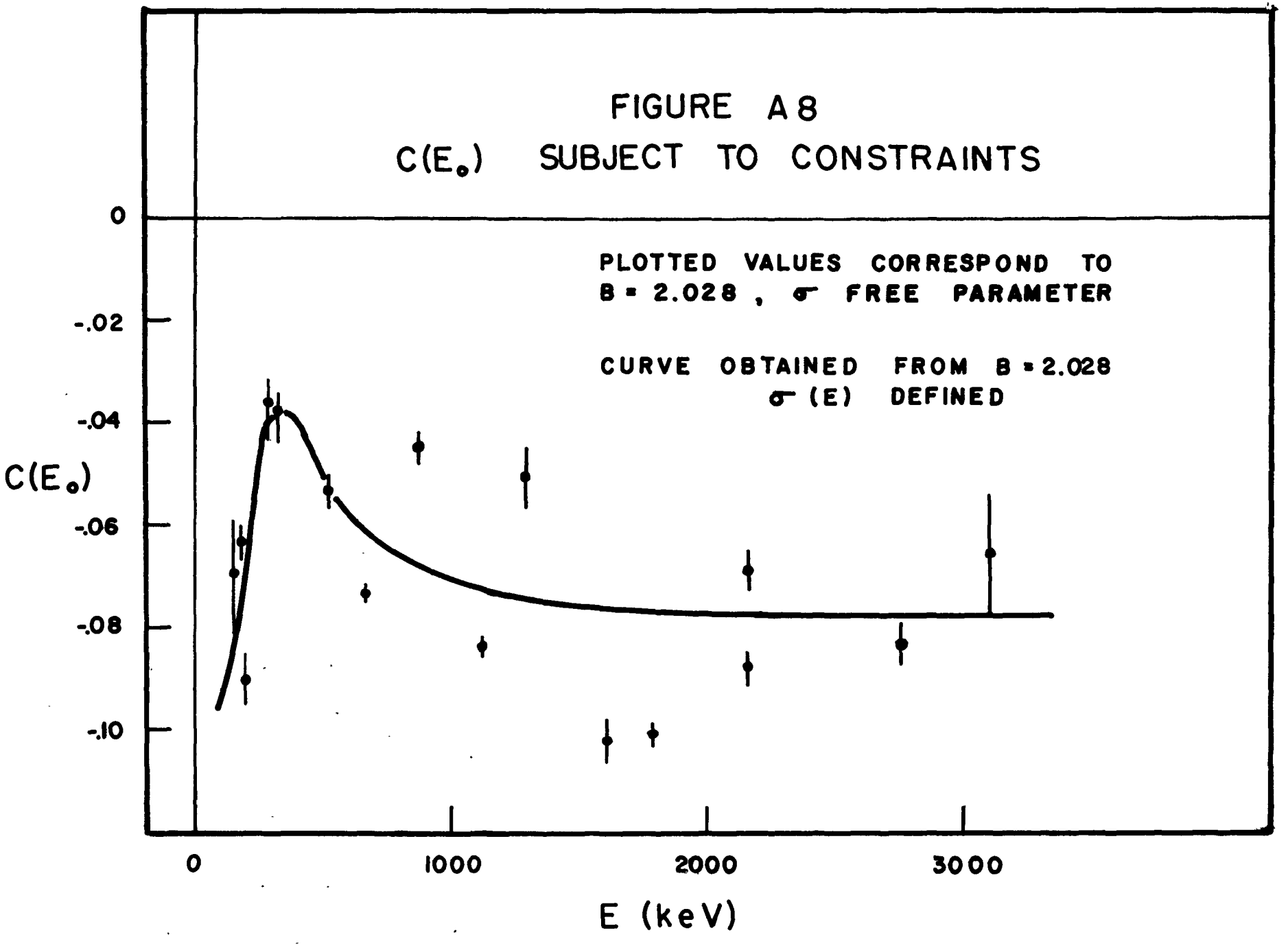
FIGURE A 8
C(E₀) SUBJECT TO CONSTRAINTS
PLOTTED VALUES CORRESPOND TO
B = 2.028 , σ FREE PARAMETER
CURVE OBTAINED FROM B = 2.028
σ (E) DEFINED
0
-.02
-.04
-.06
-.08
-.10
C(E₀)
0
1000
2000
3000
E (keV)

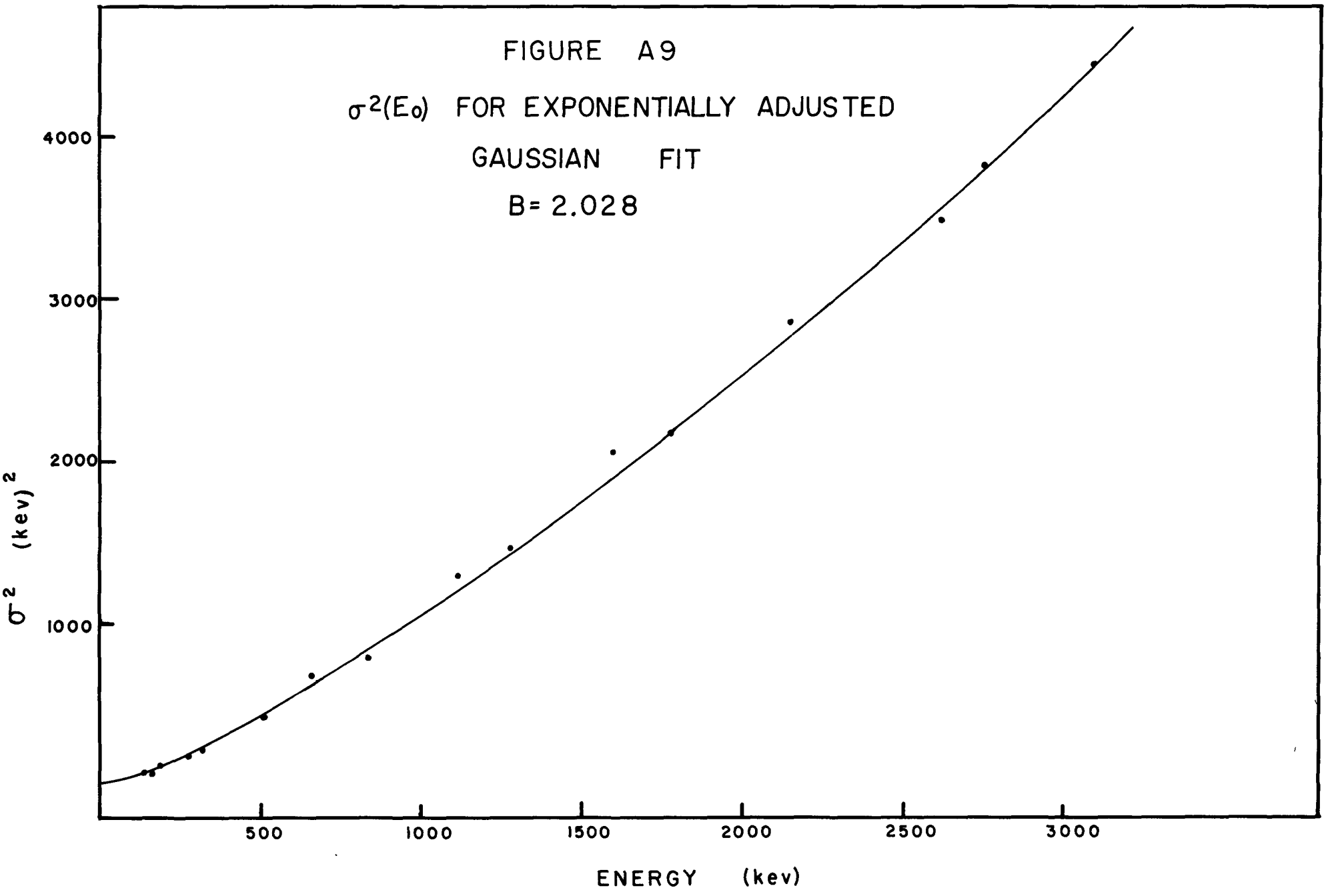
FIGURE A9
σ²(E₀) FOR EXPONENTIALLY ADJUSTED
GAUSSIAN FIT
B= 2.028
4000
3000
2000
1000
σ² (kev)²
500
1000
1500
2000
2500
3000
ENERGY (kev)

TABLE AIII

A COMPARISON OF ANALYTICAL FUNCTIONS
FITTED TO EXPERIMENTAL PHOTO-PEAKS

Energy (keV)	X^2			Degrees of Freedom
	Gaussian	Helmer-Heath Function	Exponentially Adjusted Gaussian	
81	11	8.1	4.9	6
166	264	14.2	14.7	15
192	219	3.9	4.8	6
279	47	8.5	13.8	11
323	143	8.6	20.1	15
511	305	23.8	24.3	18
662	906	21.0	16.5	12
835	145	11.4	10.3	10
1114	1563	26.7	19.2	16
1280	70	11.7	10.6	8
1600	774	17.9	17.3	18
1780	1541	32.3	24.8	18
2150	424	19.7	13.7	19
2755	287	9.7	11.1	14
3100	14	4.5	4.1	10
$\Sigma x^2/\Sigma f$	29.6	1.13	1.07	

Note: Degrees of freedom for the Gaussian fit in all cases is (Degrees of freedom) + 2

TABLE A IV

PARABOLIC LEAST-SQUARES FIT FOR B

B	X^2
2.08	350.06
2.06	326.95
2.04	314.64
2.00	323.38

$f = 244$

$$X_o^2 = 312.5$$

$$B_o = 2.028$$

$$\delta(B_o) = \pm 0.010$$

Fit includes 17 standard lines

Energy range = 81 keV - 3100 keV

It is expected that deviations from this relation may be found, particularly at low energies. Therefore, δ^2 was fitted to the form

$$\delta^2 = A_o + A_1 E + A_2 E^2 \qquad \text{(II.2.3.e)}$$

The solid curve in Figure A 9 is the resulting solution. The solid line in Figure A 8 corresponds to the values of C obtained under the constraint imposed by B = const = 2.028, and the new constraint imposed by the least-squares solution for $\delta^2(E)$.

The Physical Significance of C(E)

The response of NaI detectors to gamma-radiation was first shown by Engelkemeir (R19) to be a non-linear function of energy. Figure A10 shows the variation of pulse-height response with energy for the detector used in the present work, as determined by Prestwich (R 20). Due to the non-linear detector response, the summing of multiple events in the detector gives rise to a peak-broadening effect which is not Gaussian in form. Zerby et al (R 21) have determined this "intrinsic" peak broadening by means of Monte Carlo calculations. Since this effect is non-Gaussian the convolution of the intrinsic contribution with the approximately Gaussian response of the photo-multiplier may not result in a Gaussian photo-peak contribution. The intrinsic broadening does not represent the major contribution to photo-peak width, since it is effectively "smeared" by the larger photo-multiplier broadening. There is also a certain proportion of single events from photo-electric absorption which, of course, do not contribute to the intrinsic effect. Figure A 11 shows an adaptation of a plot of the intrinsic broadening

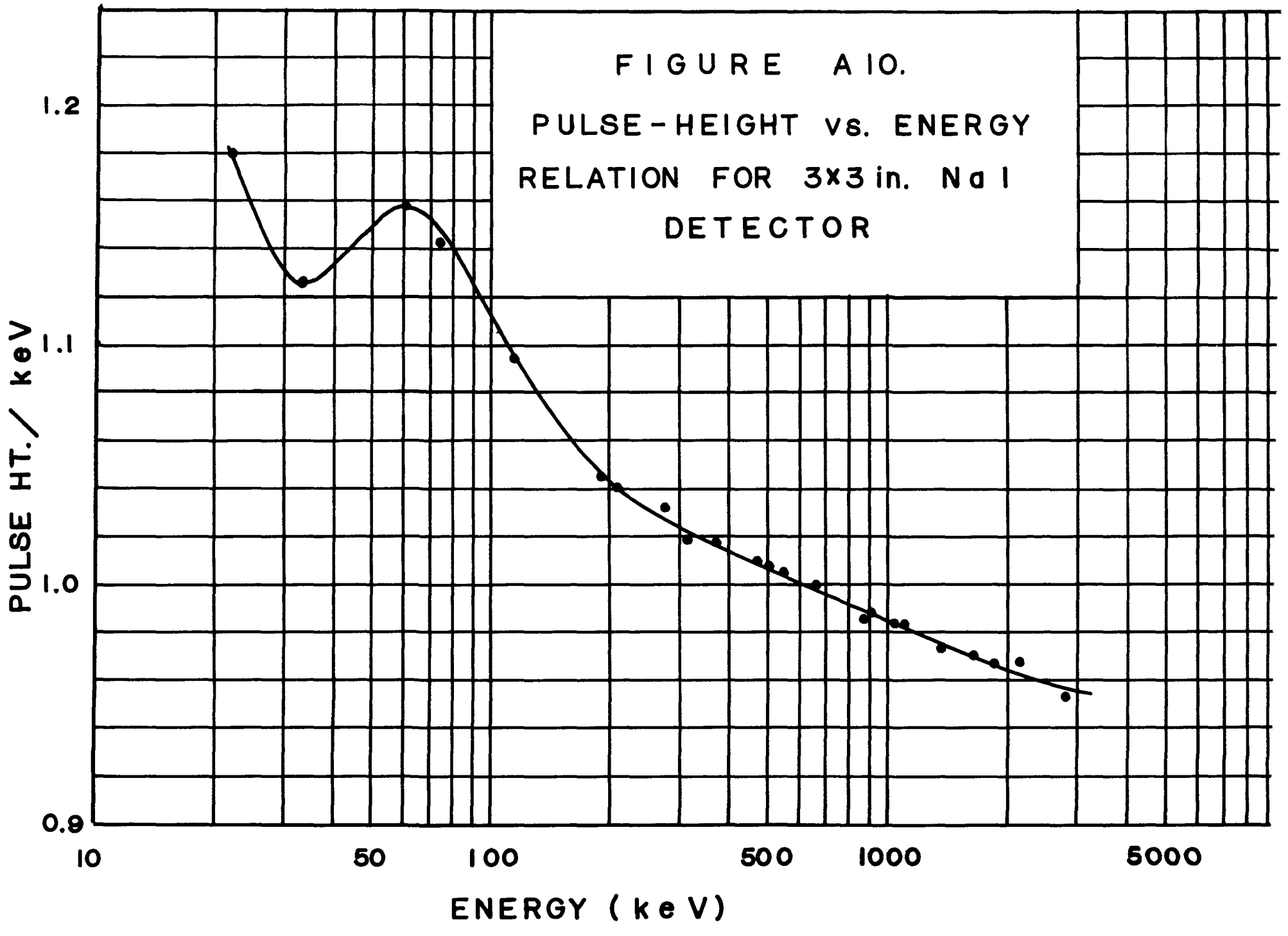
FIGURE A10.
PULSE-HEIGHT vs. ENERGY RELATION FOR 3x3 in. NaI DETECTOR
PULSE HT./ keV
1.2
1.1
1.0
0.9
10
50
100
500
1000
5000
ENERGY (keV)

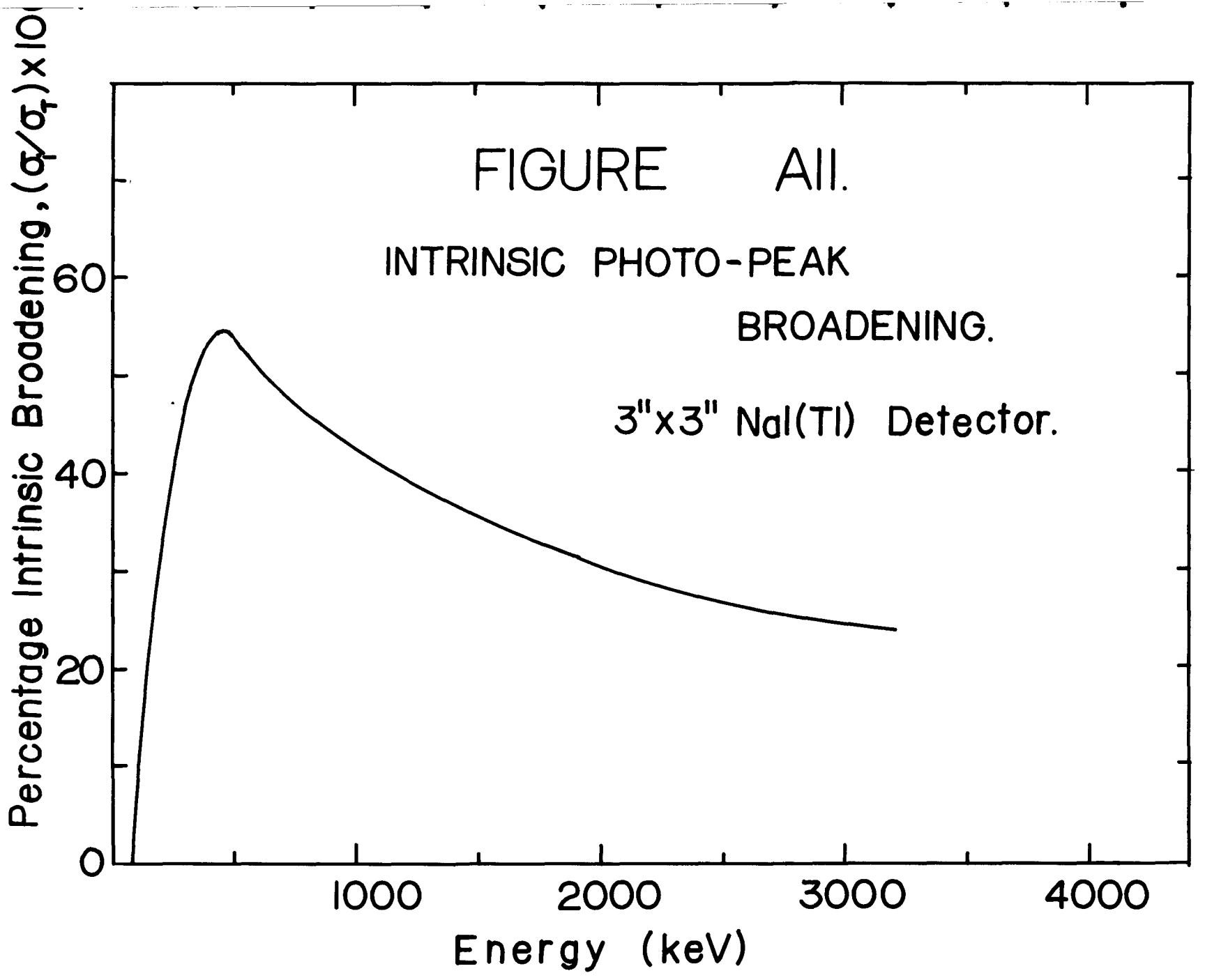
FIGURE AII.
INTRINSIC PHOTO-PEAK
BROADENING.
3"x3" NaI(Tl) Detector.
Percentage Intrinsic Broadening, (σi/σt) x 10
0
20
40
60
1000
2000
3000
4000
Energy (keV)

calculated by Zerby et al (R 21) for a 3" x 3" NaI detector. The ordinate is δ_i/δ_t.

Here, δ_i represents an "effective" intrinsic line width where the intrinsic contribution has been approximated by a Gaussian, and δ_t is the total line width as obtained in the present work.

A comparison of figures A 11 and A 8 shows that C is definitely related to the intrinsic line broadening. The functional relationship between these two variables is not obvious. However, the absolute value of C is a measure of the departure of the photo-peak from a Gaussian form. It is beyond the scope of this work to speculate further on the origin of the analytical form of the photo-response.

II.2.4 Manipulation of the Response Functions

Following the initial smoothing and photo-peak fitting, the entire response function is zero-justified (i.e. shifted with no change in pulse height scale so that zero energy corresponds to zero pulse height). All the response functions are handled in a similar fashion. However, since linear interpolation in energy is used in the line shape generation routine, it is necessary to generate an auxiliary response function at each standard energy which has the same pulse-height scale as the neighbouring standard line. This is carried out by the "stretching" routine. The area under each response curve is normalized to 10^5 counts and the response functions, along with all pertinent photo-peak parameters, etc., are stored on cards for use in the line-shape fitting program.

II.2.4.1 The Stretching Routine

Prior to the use of this routine the distortion due to analyzer non-linearity is removed. Since the energy non-linearity is to be conserved, the stretching routine is physically equivalent to a gain change of the analyzing system.

The analytical portion of the required response is generated after suitable adjustment of δ and x_o to the new values δ' and x_o' corresponding to the new pulse-height scale. B and $C(E_o)$ are, of course, gain independent. If zero pulse height is to correspond to channel Z, then the non-analytical portion of the response at channel location $x' + Z$, say, is generated by integrating the standard response function between channels $R.(x - \frac{1}{2})$ and $R.(x + \frac{1}{2})$. Here, R is the relative gain, given by

$$R = \frac{x_o}{(x_o' - Z)}$$

The integration is carried out by integrating a cubic polynomial across the region. The cubic polynomial is obtained by a seven-point fit with unit weighting in this region.

The joining of numerical to analytical response is accomplished by smoothing the numerical portion near the join according to the neighboring analytical form.

II.2.5 Line Shape Generation

Once the response functions are available in library form, the only major requirements remaining are to generate by interpolation response functions of the desired energies and to fit these functions to the experimental data.

For interpolation purposes the response function is divided into three sections, as illustrated in Figure A 12 . The low energy portion extends from zero energy to a point well above the back scatter peak or above the annihilation peak if it exists. The high energy portion comprises only the analytical section of the response. The intermediate region covers the remainder of the response function. The first step is to generate a "temporary" response function of the desired photo-energy on the same linear pulse-height scale as the two standards which bracket the desired response in energy. By pre-arrangement, any pair of adjacent standards available from the library are on the same pulse-height scale.

The high energy section is generated with the parameters $\delta(E)$ and $C(E)$ being determined from the appropriate equations. x_o is determined by the energy and the "temporary" pulse height scale, while A is determined by interpolation between the bracketing standards.

The low energy portion is obtained by shifting the corresponding portion of both standards so that the back-scatter peaks are centred at the same channel location as the required temporary back-scatter peak. A linear interpolation then serves to determine the temporary standard in this region.

The intermediate region is also obtained by shifting the standards, but in this case the photo-peaks of both standards are made to lie at the location x_o of the respective vectors. A linear interpolation across the intermediate region then defines the remainder of the temporary standard. It should be understood that "shifting"

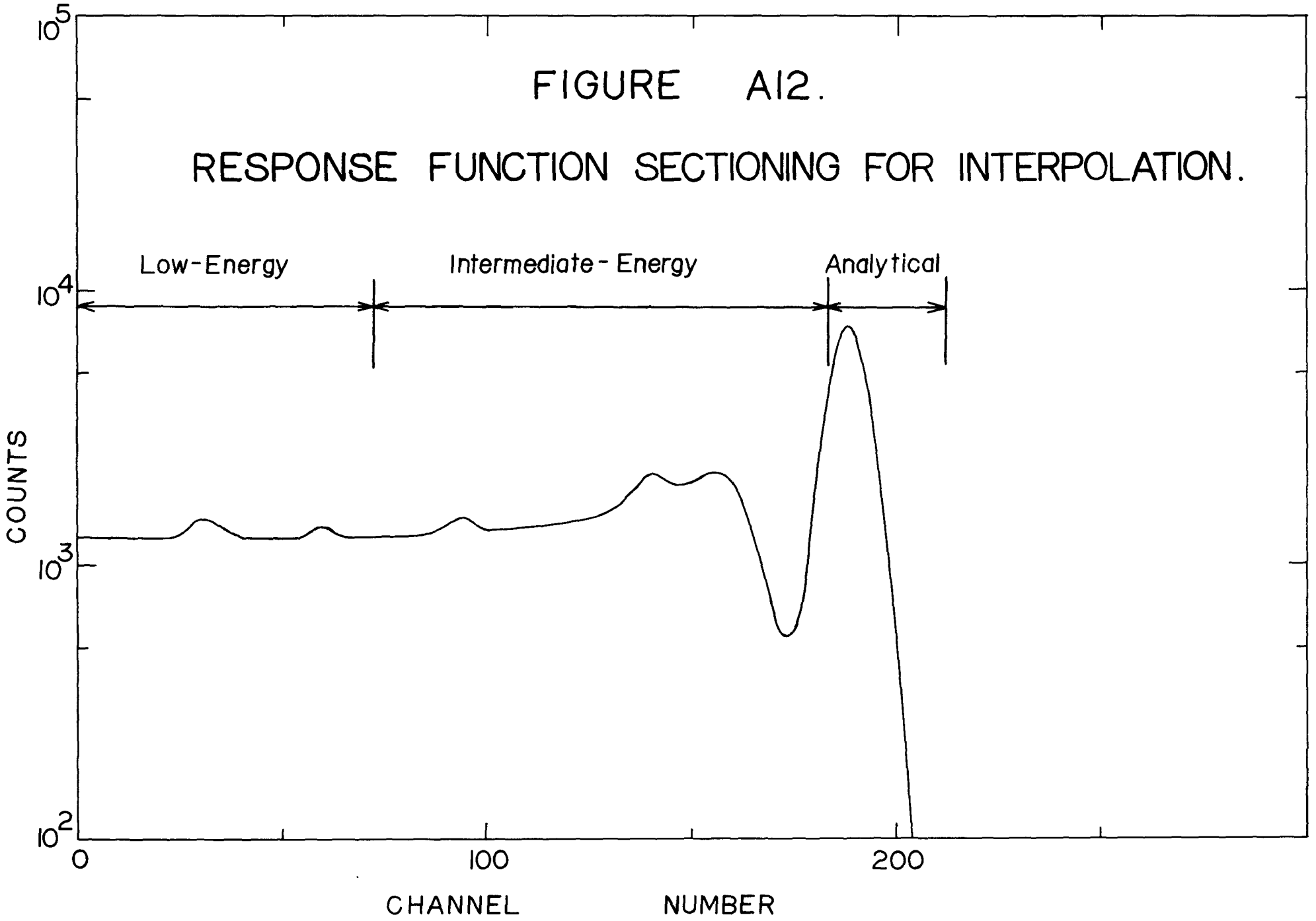
FIGURE A12.
RESPONSE FUNCTION SECTIONING FOR INTERPOLATION.
Low-Energy
Intermediate-Energy
Analytical
10^5
10^4
10^3
10^2
COUNTS
0
100
200
CHANNEL NUMBER

in the context of the foregoing paragraphs corresponds only to a zero change, with pulse-height scale remaining constant.

The stretching routine is then employed to place the generated function on the same pulse-height scale as that of the data to be analyzed. A further renormalization is carried out to ensure equal areas under all the response curves. A "response surface" obtained for a 3" x 3" NaI detector by generating a series of lines over the range 100 keV to 3000 keV is shown in Figure A13 .

II.2.6 Gain Shift and Zero Corrections

In certain restrictive circumstances in the recording of experimental data, it may not be possible to stabilize the equipment, and especially the photo-multiplier, against gain shift. If the source counting rate decreases considerably during the experiment or if the counting period is long, then spectral distortion due to gain shift is probable. Accurate analysis of the data would become impossible under such conditions. This situation may arise if the rapid decay of the source allows no time for gain stabilizer set-up, or if the spectrum does not contain prominent peaks to use as monitors, or possibly if daughter activity growth seriously disturbs the spectrum during analysis.

A subroutine has been developed which treats the gain and/or zero shift in the spectrum as two new parameters. These parameters may be determined by the parabolic method along with the line energies. The necessary assumption is that the rate of change of gain and/or

FIGURE A13

3" x 3" NaI(Tl) DETECTOR

GAMMA - RAY RESPONSE

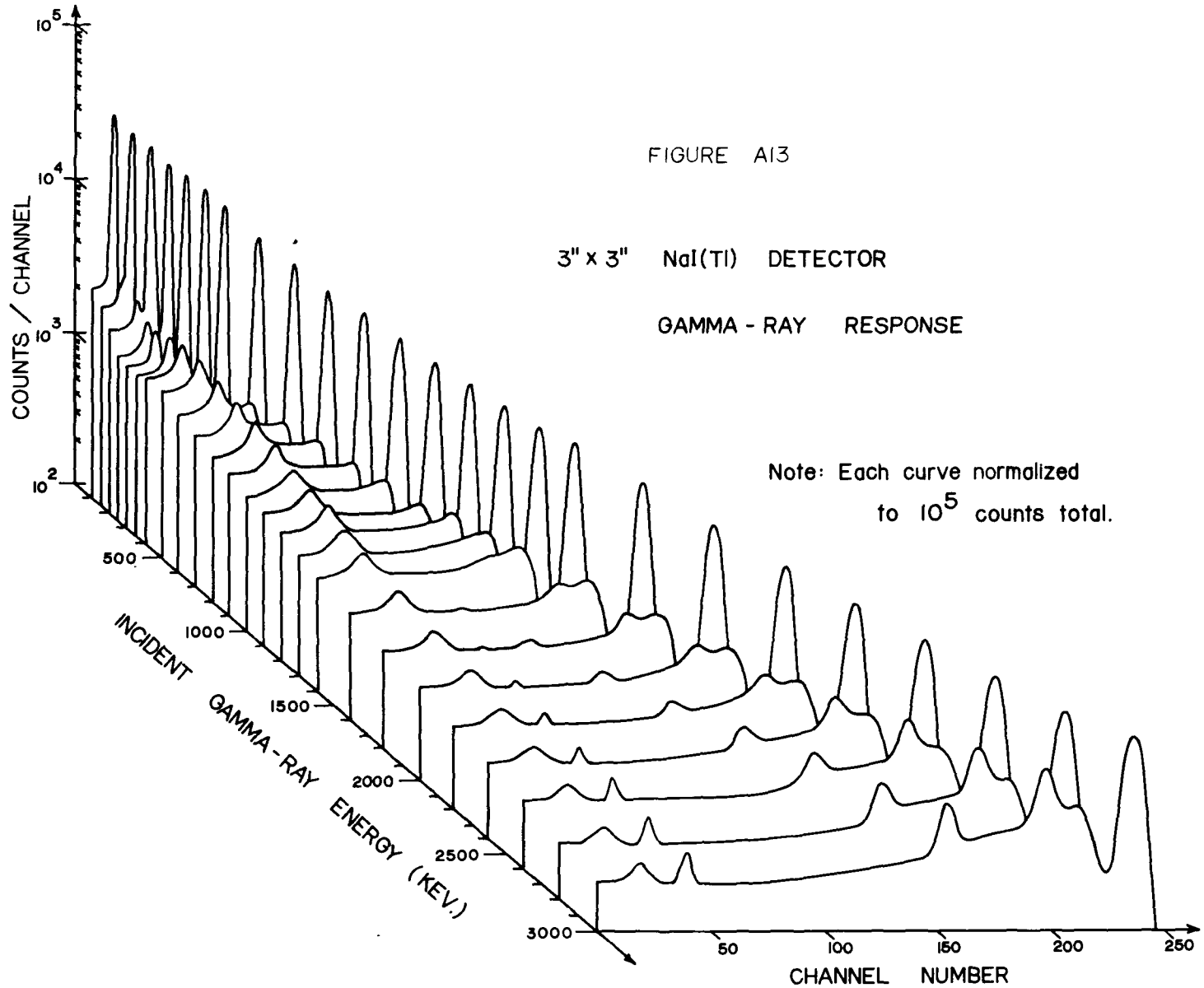

Note: Each curve normalized to 10^5 counts total.

zero shift is constant throughout the experiment. This is probably a logical assumption provided the shifts are not large. The subroutine folds into the line shape, which has been generated at the mean line location, a channel width which is proportional to the amount of shift. The effective channel width Δx_c is given by

$$\Delta x_c = 1.0 + \left| s + r\,(x_c - Z) \right|$$

Here, s is the zero shift (channels)

r is the gain shift (channels/channel)

x_c is the channel of interest ($\equiv$ channel number)

Z is the nominal zero position.

s and r are determined by the parabolic method, and the final lines fitted to the data contain these parameters. The details of the Fortran IV program which performs this data reduction are outlined in Appendix III

II.3 Data Distortions Introduced by the Analyzing System

There are several sources of distortion in the pulse-height spectra which are relatively simple to correct, thus adding to the quality of the final results. The main distortion, of course, arises through the NaI non-linear response. However, the entire concept of response surface generation by interpolation is built up because of the inability to correct for this. The general approach in this work has been to leave the experimental data untouched. Any distortions in the data are accounted for by introducing similar distortions into the response functions before the data reduction is attempted. Since the data is statistical in nature it is exceedingly difficult

to make proper corrections to the data itself without, in effect, smoothing and destroying the statistical significance of the data.

II.3.1 Analyzer Non-Linearity

Figure A14-a shows a plot of the differential linearity of the ND-160 analyzer. The differential linearity of the lower 5% of the channels is quite irregular. However, useful data is seldom recorded in this section of the analyzer. The remainder of the differential curve is shown in the figure. This curve may be fitted to a functional form given by

$$\omega_i = 2\alpha X_i + \beta \qquad \text{(II.3.1.a)}$$

The corresponding integral curve is shown in Figure A14-b . The departure from linearity is not so obvious in this curve, which obeys the relation

$$P_i = \alpha X_i^2 + \beta X_i + \gamma \qquad \text{(II.3.1.b)}$$

The standards recorded by the analyzer are shifted to a linear pulse height scale given by

$$P_i' = \beta X_i$$

Before the response function is fitted to the data, the appropriate correction is made on the new pulse height scale, so that

$$Q_i = \alpha y_i^2 + \beta y_i$$

The analyzer linearity is measured by means of a Victoreen pulse generator, according to the method outlined by Heath et al (R22). Measurements attempted with a sliding pulse generator showed distortion due mainly to non-linearity of the sweeping ramp voltage which was derived from a Tektronix oscilloscope.

N.D.-160 ANALYZER 512 RAMP 256 CHANNELS

FIGURE A 14-A

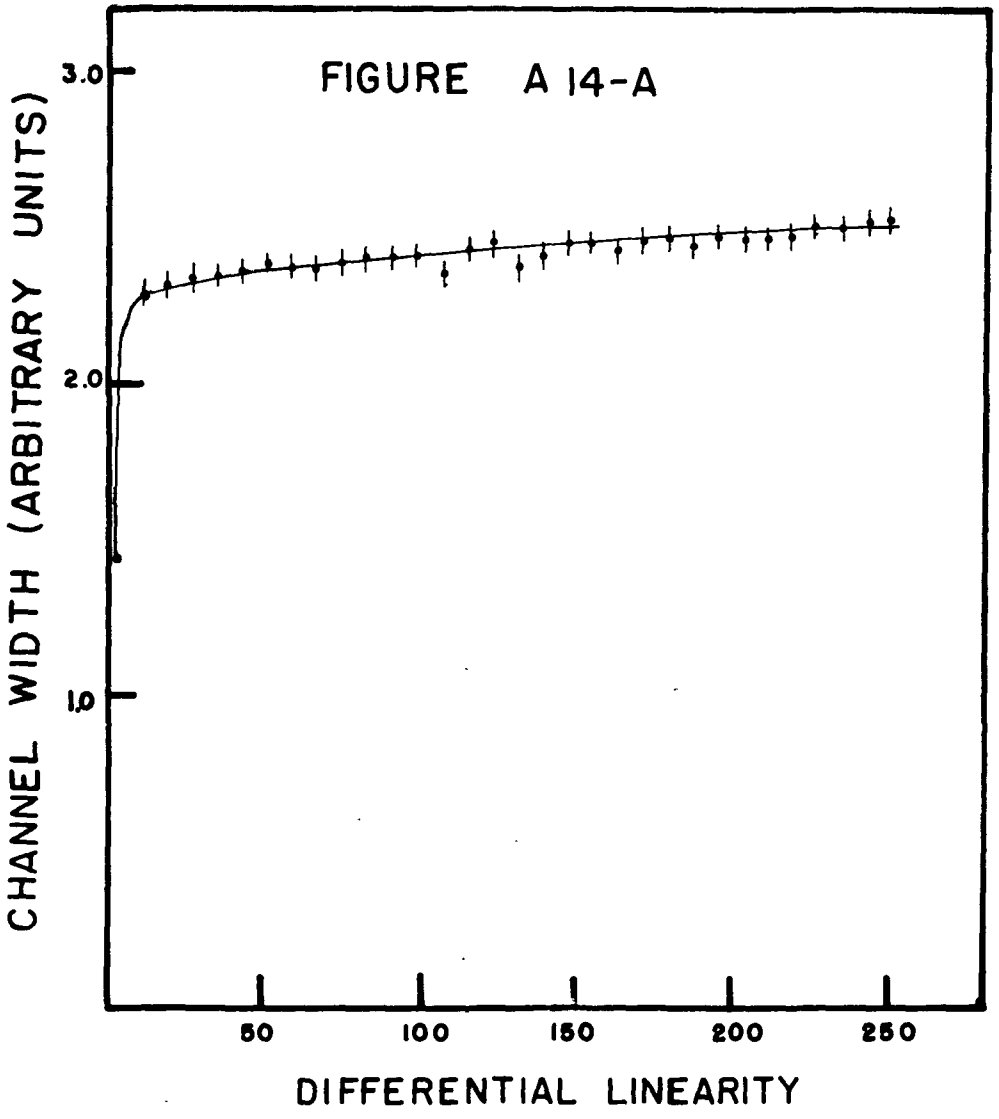

FIGURE A 14-B

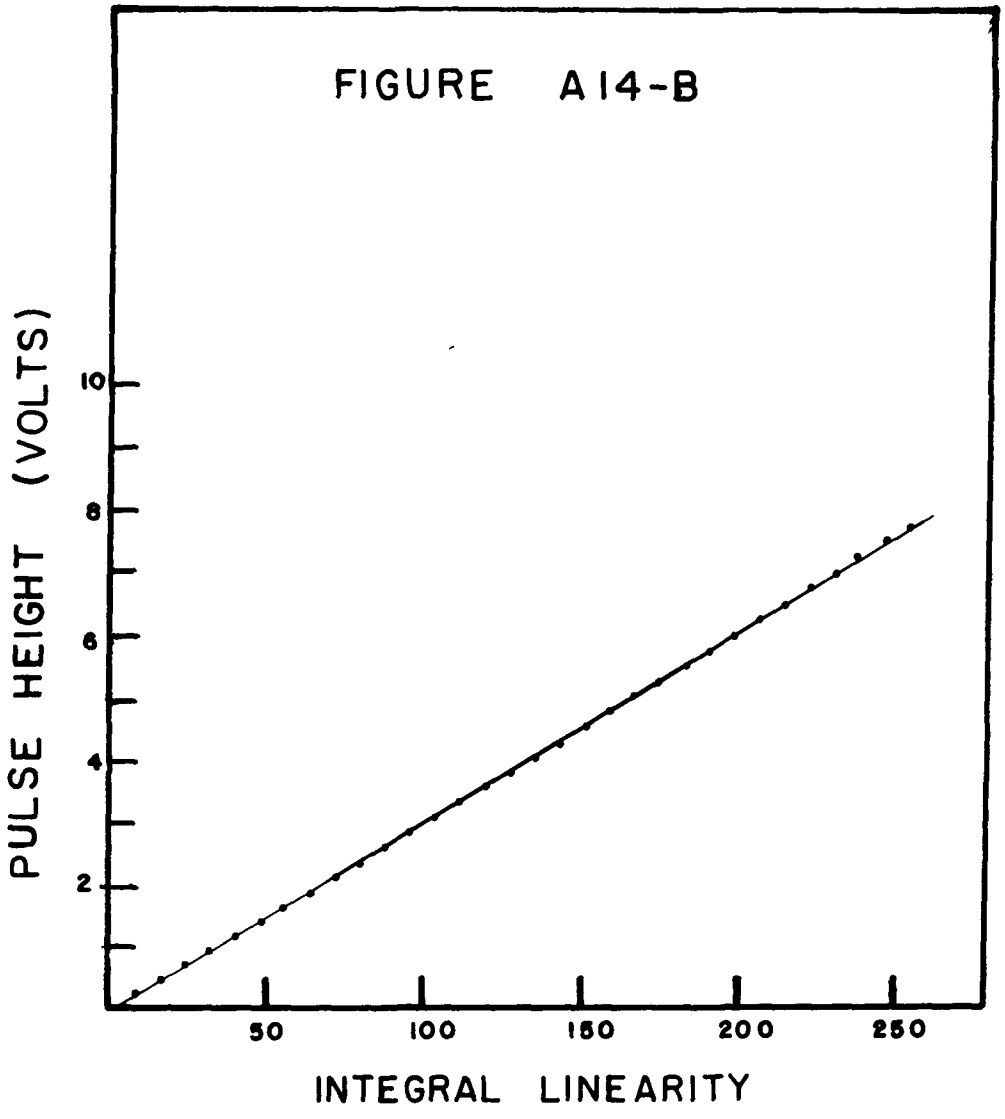

II.3.2 Channel Profile Effects

The channel profile for the ND-160 analyzer, which was used for most of this work, is shown in figure A 15 . Due to electronic jitter the channel edges are not sharply defined, with a resultant overlap in storage. The overlap in this case is 2% which is not a serious effect. Larger overlaps may be allowed for by folding the channel profile into the response functions which of necessity have assumed no overlap due to profile effects.

II.3.3 The Histographical Character of Analyzer Data.

The information recorded by a multi-channel analyzer is of necessity histographical in nature because of the finite number of storage locations available. The incoming pulses have a continuous pulse-height distribution while the number of events recorded in a particular channel represents the integral of the frequency spectrum of pulse heights falling across the channel.

In order to fit a function to the data, the functional value which is fitted must therefore be the mean value of the integral of the function over the channel width. If second and higher-order derivatives may be ignored, then the channel integral

$$\int_{x_c - \Delta x/2}^{x_c + \Delta x/2} f(x)\,dx \Big/ \int dx$$

is given by $f(x_c)/\Delta x$ and the functional value at the channel center may be chosen. However, in the case of a swiftly varying function such as a Gaussian, a certain amount of error is introduced by this

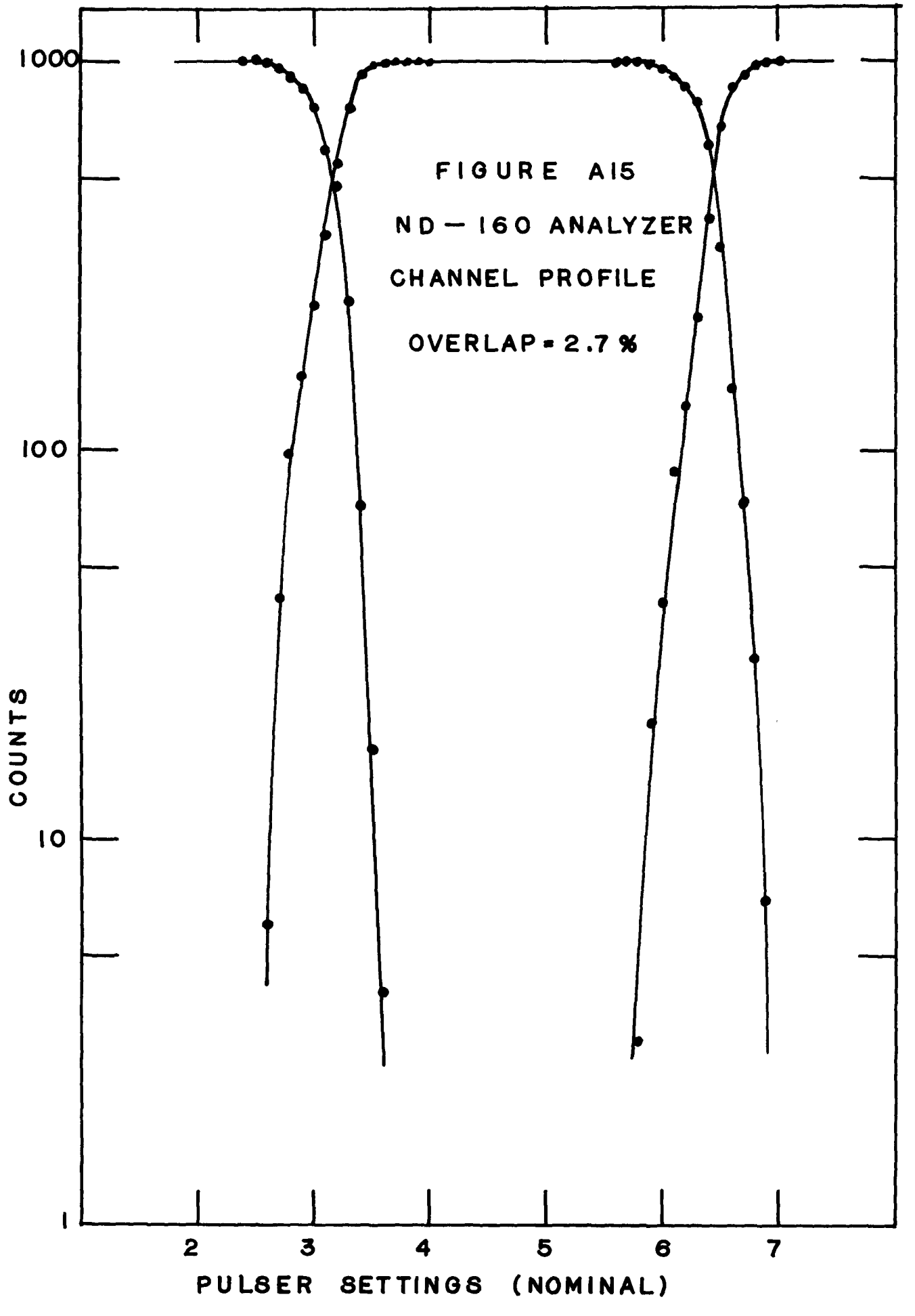

FIGURE A15

ND – 160 ANALYZER

CHANNEL PROFILE

OVERLAP = 2.7 %

assumption . Figure A16 shows the errors caused by approximating the channel integral of a Gaussian by the value of the function at the channel centre.

FIGURE A16

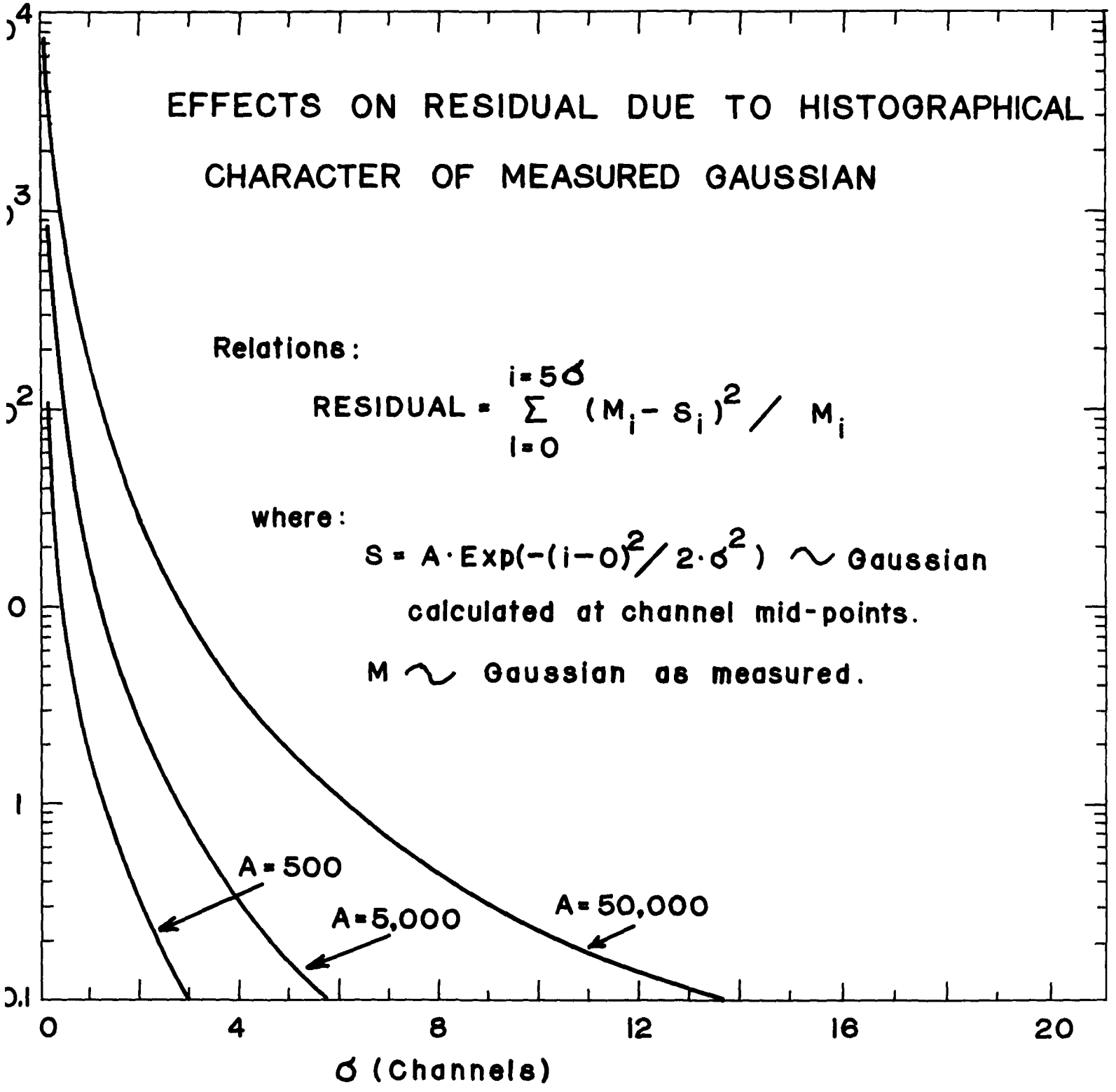
EFFECTS ON RESIDUAL DUE TO HISTOGRAPHICAL CHARACTER OF MEASURED GAUSSIAN
Relations:
RESIDUAL = $\sum_{i=0}^{i=5\sigma} (M_i - S_i)^2 / M_i$
where:
$S = A \cdot Exp(-(i-0)^2 / 2\cdot\sigma^2) \sim$ Gaussian calculated at channel mid-points.
$M \sim$ Gaussian as measured.
A = 500
A = 5,000
A = 50,000
)4
)3
)2
0
1
0.1
0
4
8
12
16
20
σ (Channels)

APPENDIX III

III.1 The Line Shape Fitting Program

The program has been made as versatile as possible without compromising in calculation efficiency. It has been programmed in Fortran IV for use with the IBM 7040 computer with 32k core storage. In addition, two utilities on the 1302 disk file are used for storage of the library lines and for temporary storage of line shapes in the gain-shift determination procedure. The program is "chained" in two "links" since the entire program exceeds the fast memory capacity of the computer. The first link handles preliminary data analysis and the majority of the input-output. The second link generates and fits lines to the spectrum by least-squares. This link also may determine the energies of selected spectral lines or it may solve for gain shift in the spectrum, by the parabolic technique described in Appendix I.

The program has a capacity of 30 lines per spectrum with a maximum of 256 data channels. The computer error due to rounding has been found to be negligible. The inversion of a 25 x 25 matrix from a typical calculation was checked by means of a double precision matrix inversion routine and the calculated intensities agreed to 5 figure accuracy. The line shape generation speed averages around 5 seconds per line, and a 30 line spectrum may be fitted in less than 4 minutes.

Flow charts for the various routines are shown in the follow-

ing pages, along with a typical data input and output. The program for the set-up of the standard library lines has not been included in the flow-charts since this program uses subroutines similar to those in the line-fitting program. A number of the more useful options which the program may carry out are included. However, for simplicity, several of the more complex options, such as the fitting of two-dimensional spectra with one spectrum in each pass, are not shown on the flow charts.

III.2 Main Control Link

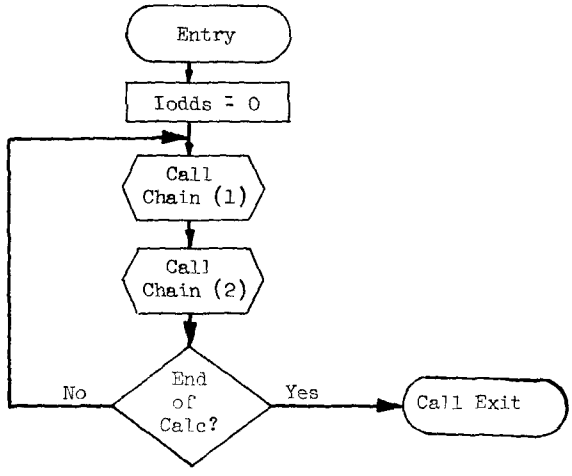

III.3 Link 1

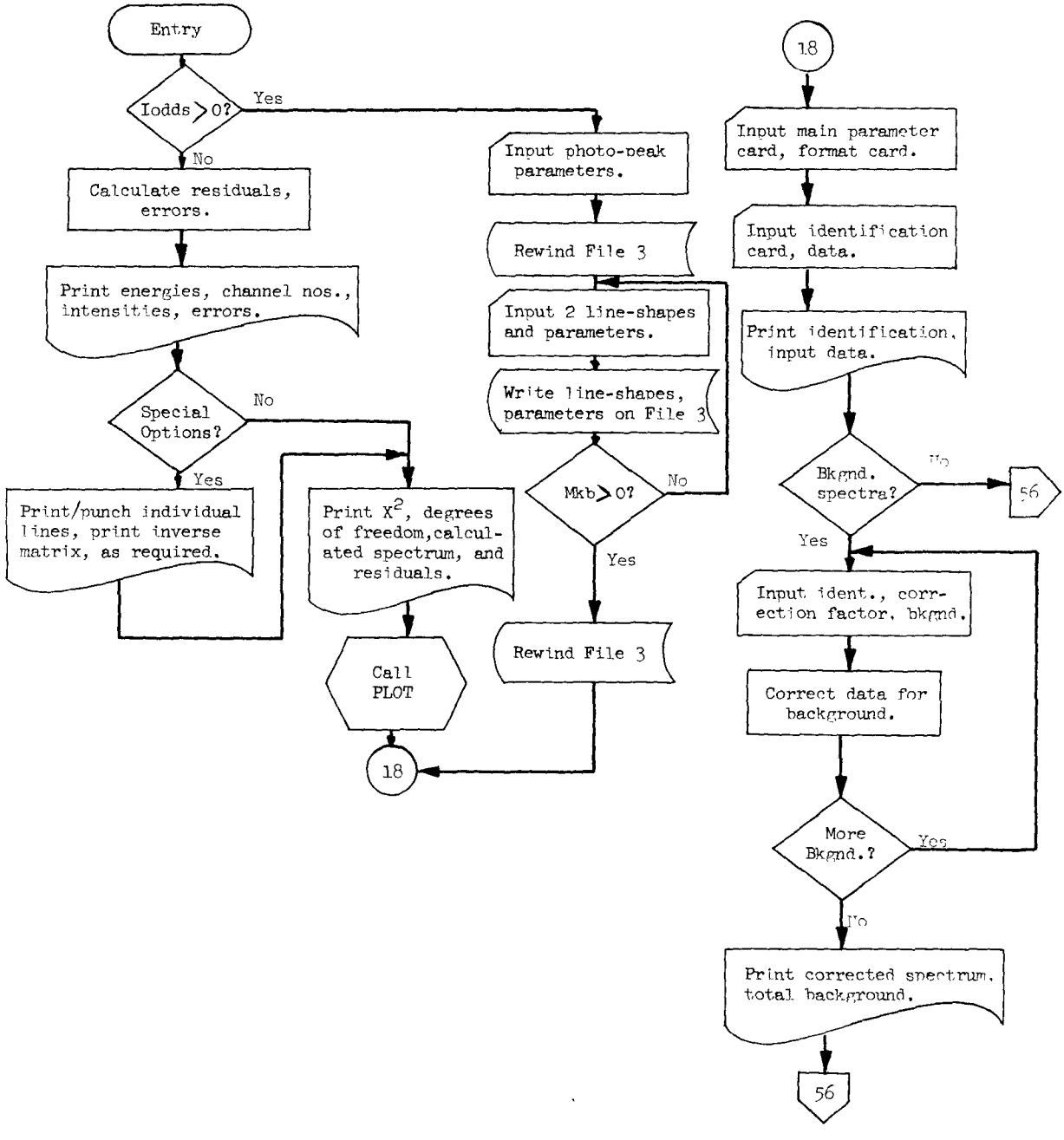

III.3.1 Link 1 Subroutine.

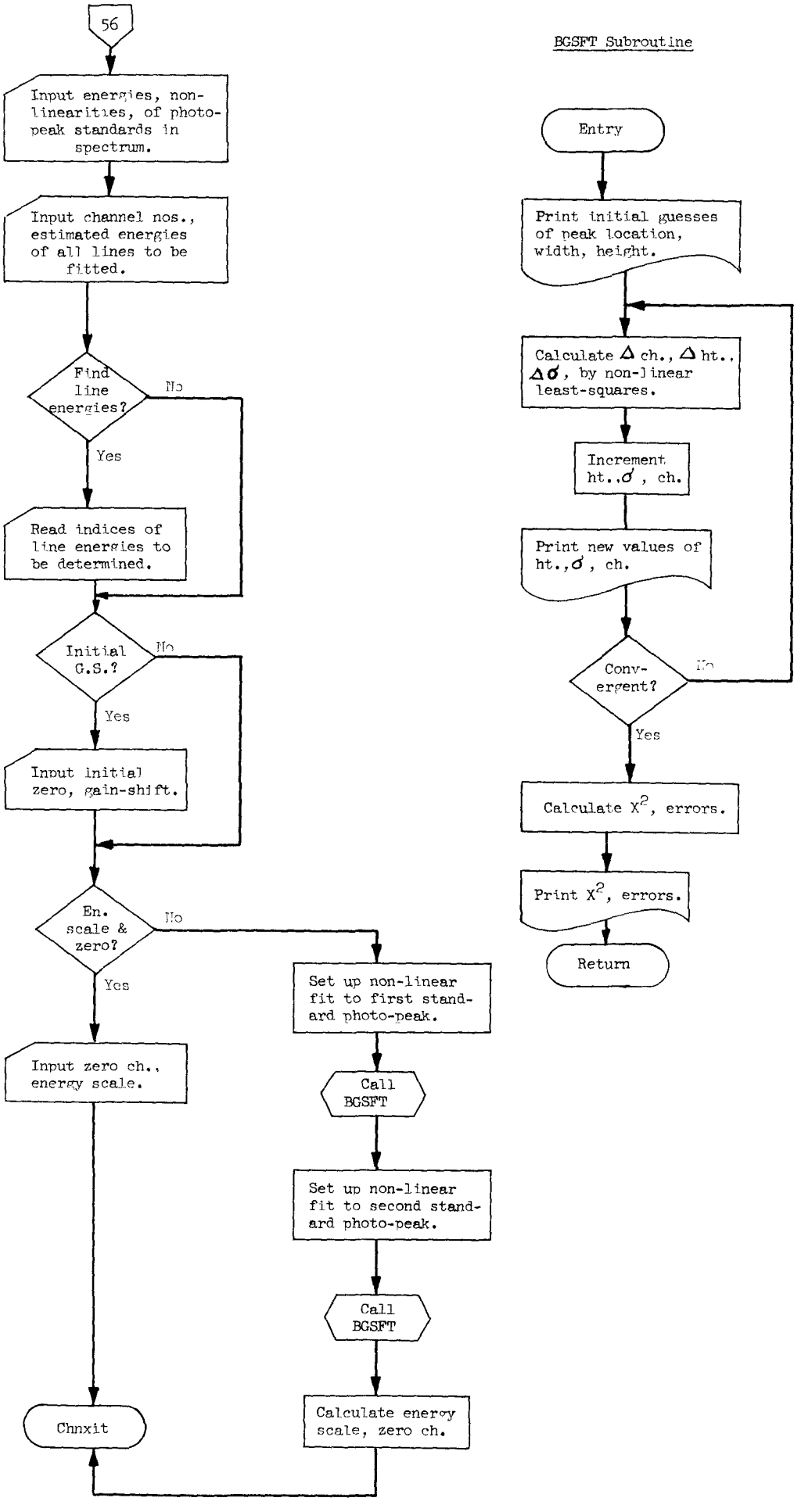

III.4 Link 2

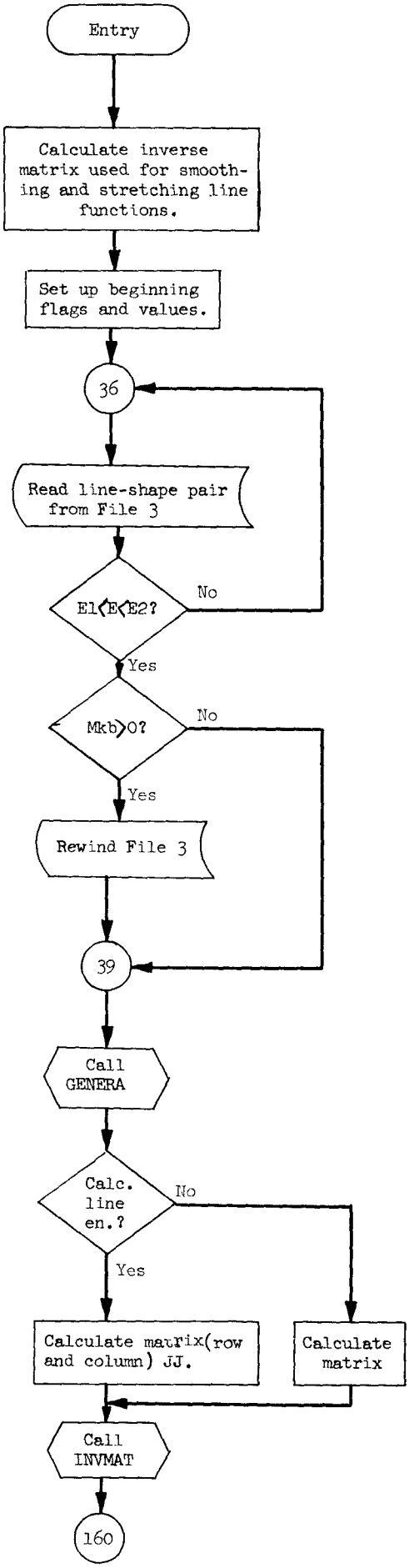
Entry
Calculate inverse matrix used for smoothing and stretching line functions.
Set up beginning flags and values.
36
Read line-shape pair from File 3
E1<E<E2?
No
Yes
Mkb>0?
No
Yes
Rewind File 3
39
Call GENERA
Calc. line en.?
No
Yes
Calculate matrix(row and column) JJ.
Calculate matrix
Call INVMAT
160

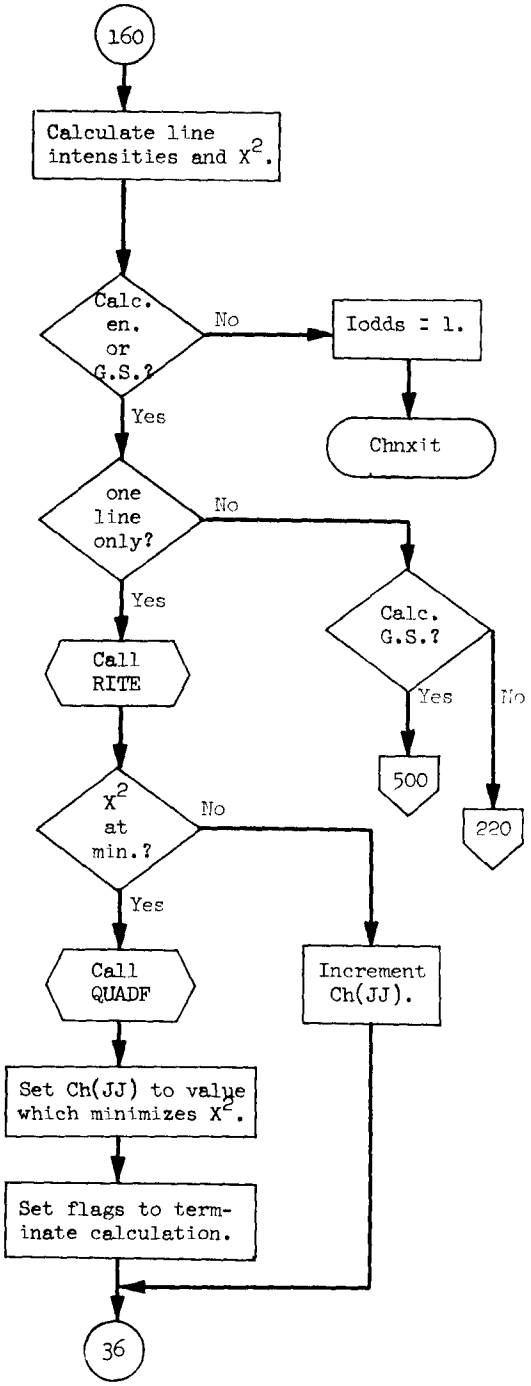
160
Calculate line intensities and X^2.
Calc. en. or G.S.?
No
Iodds = 1.
Chnxit
Yes
one line only?
No
Yes
Call RITE
Calc. G.S.?
Yes
No
500
220
X^2 at min.?
No
Yes
Call QUADF
Increment Ch(JJ).
Set Ch(JJ) to value which minimizes X^2.
Set flags to terminate calculation.
36

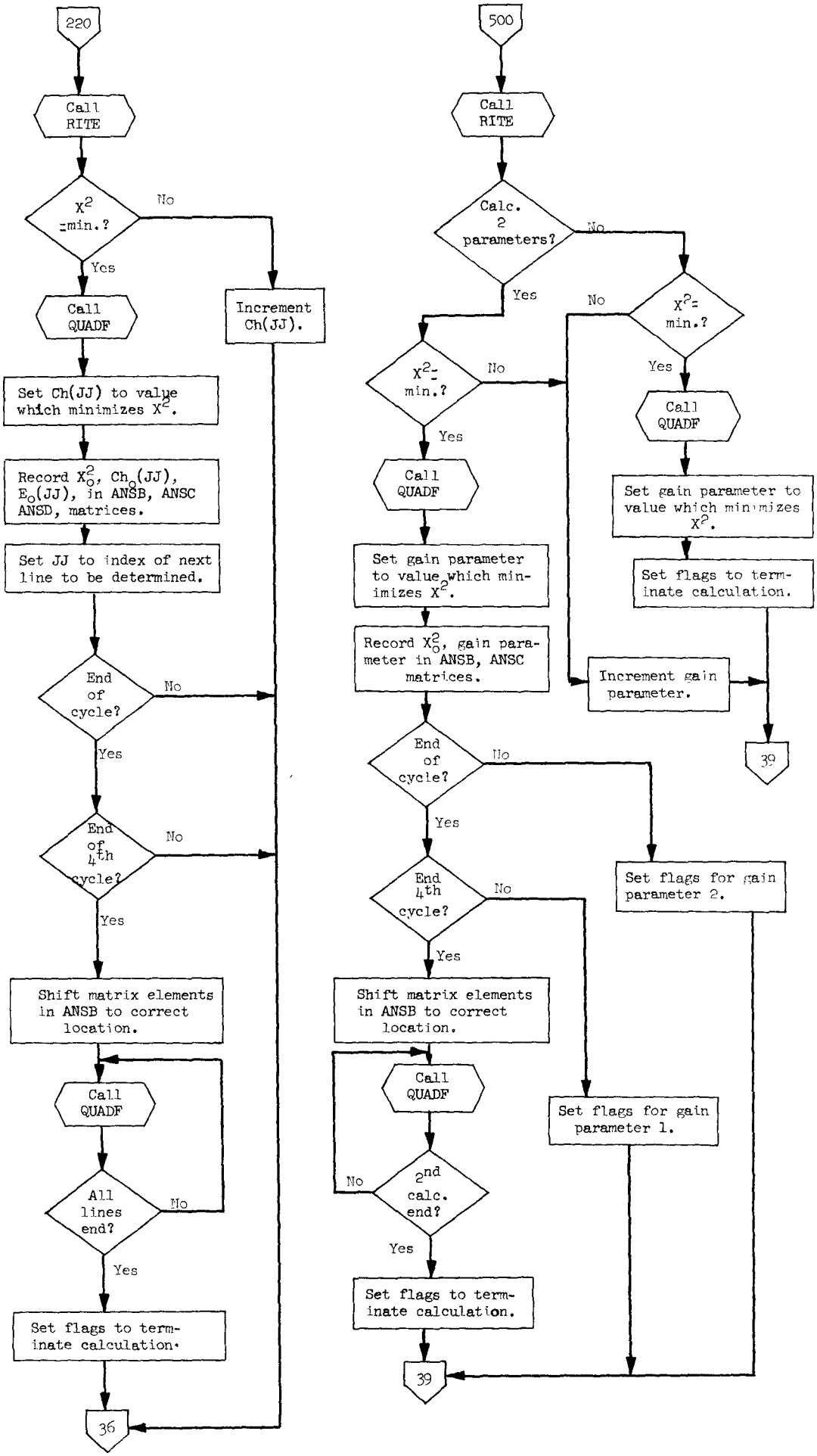
220
Call RITE
X^2 =min.?
No
Yes
Call QUADF
Increment Ch(JJ).
Set Ch(JJ) to value which minimizes X^2.
Record X_o^2, $Ch_o(JJ)$, $E_o(JJ)$, in ANSB, ANSC ANSD, matrices.
Set JJ to index of next line to be determined.
End of cycle?
No
Yes
End of 4th cycle?
No
Yes
Shift matrix elements in ANSB to correct location.
Call QUADF
All lines end?
No
Yes
Set flags to terminate calculation.
36
500
Call RITE
Calc. 2 parameters?
No
Yes
X^2= min.?
No
Yes
Call QUADF
Set gain parameter to value which minimizes X^2.
Set flags to terminate calculation.
39
X^2= min.?
No
Yes
Call QUADF
Set gain parameter to value which minimizes X^2.
Record X_5^2, gain parameter in ANSB, ANSC matrices.
Increment gain parameter.
End of cycle?
No
Yes
End 4th cycle?
No
Yes
Set flags for gain parameter 2.
Shift matrix elements in ANSB to correct location.
Call QUADF
Set flags for gain parameter 1.
No
2nd calc. end?
Yes
Set flags to terminate calculation.
39

III.4.1 Link 2 Subroutines

GENERA Subroutine

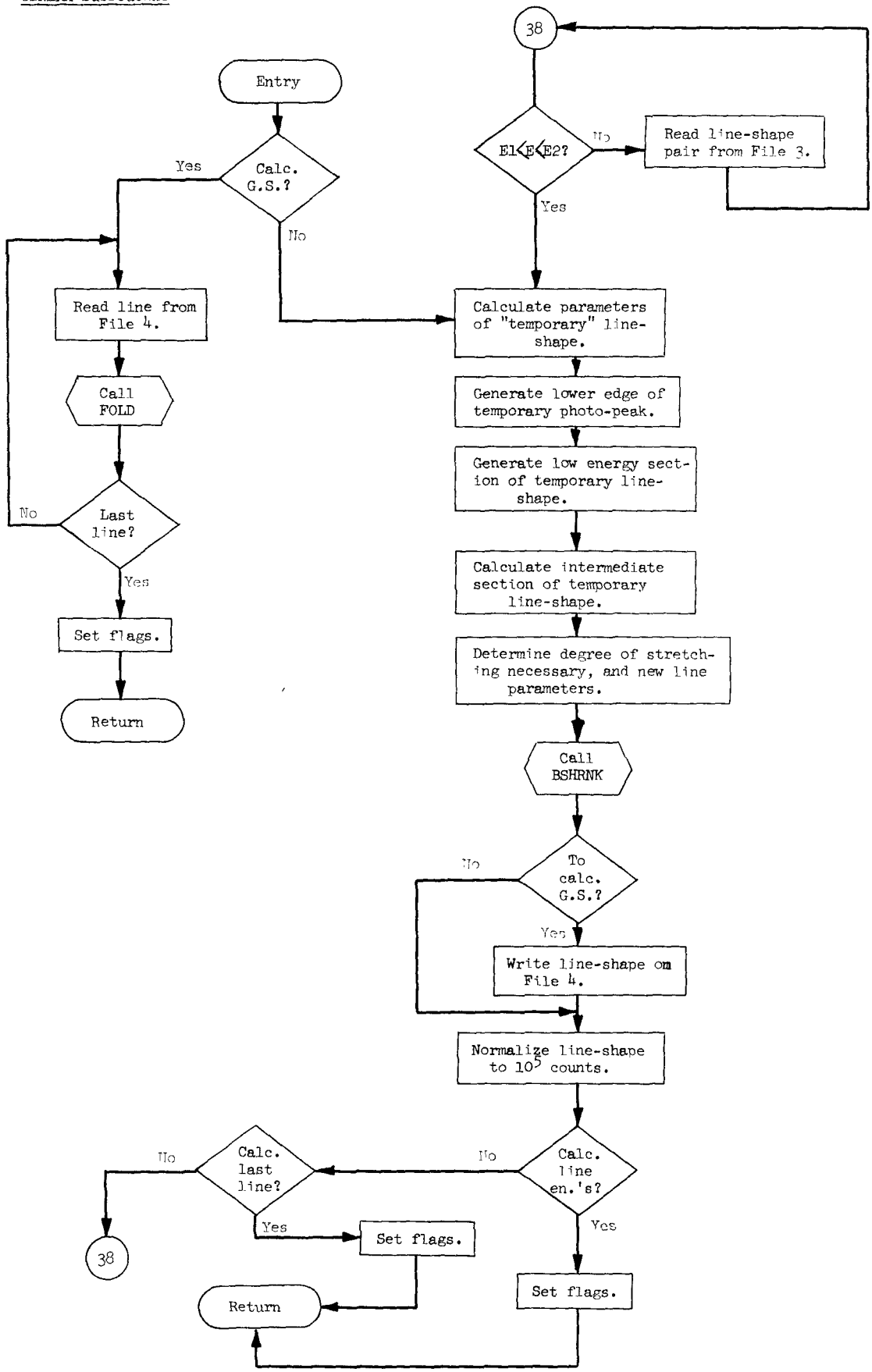

BSHRNK Subroutine

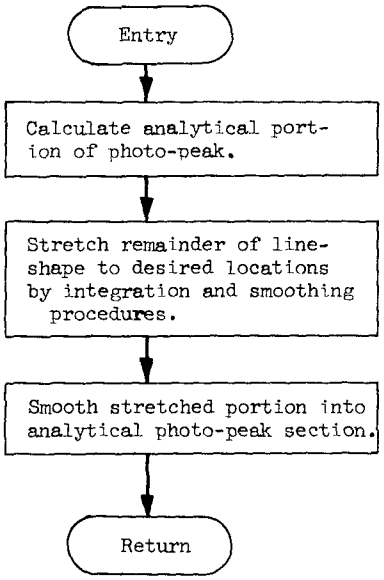

FOLD Subroutine

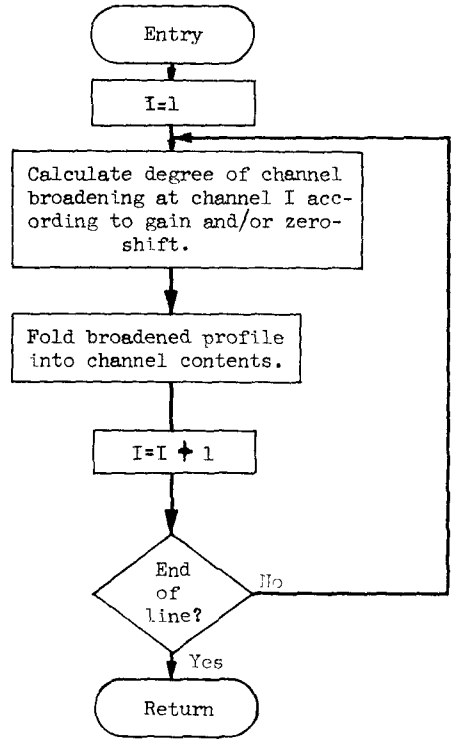

QUADF Subroutine

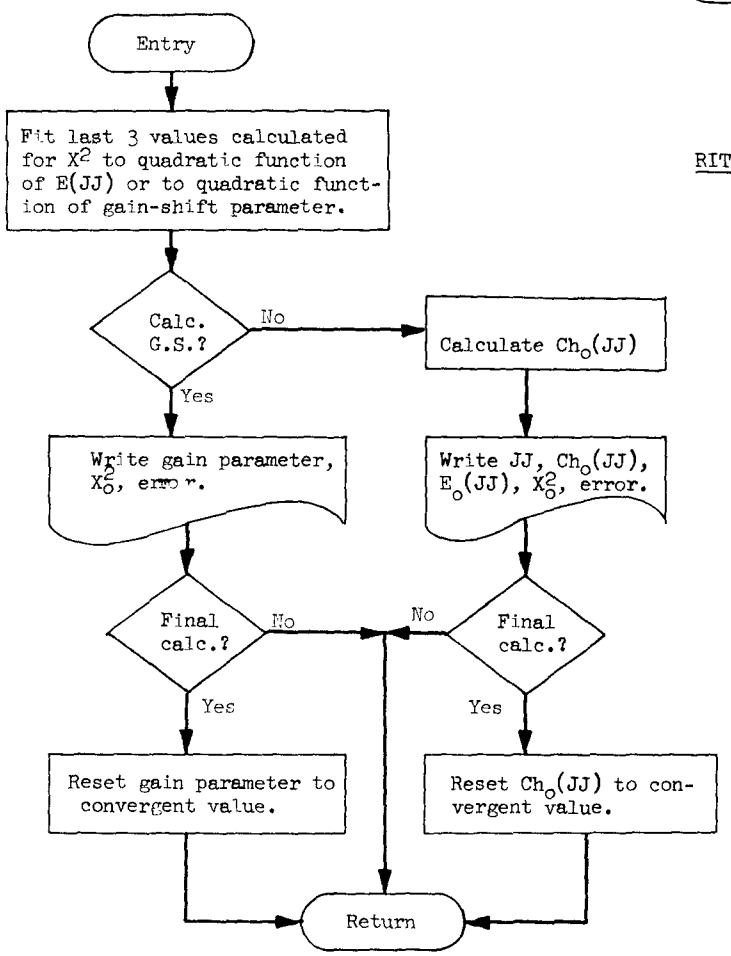

RITE Subroutine

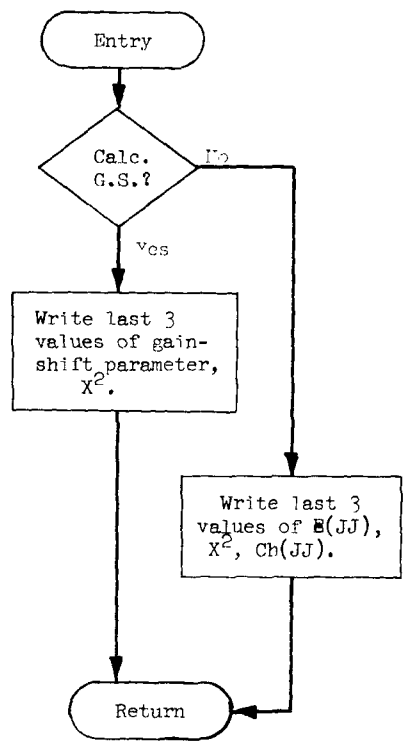

III.5 SAMPLE CALCULATION

The numbers which are contained in the following data are of no specific interest. However, the various options of the line-fitting program operation are demonstrated.

The input data is a 256 channel pulse-height spectrum, followed by one 'block' of background data. The first card is punched with the location of the two standard photo-peaks, the number of lines to be fitted (30), the number of lines to be 'searched' (1), the channel range to be fitted,and the output options. The last six cards contain the starting channel locations and the estimated photo-energies of the lines to be fitted. The last card contains the index of the line to be 'searched'. Pages A 52 to A58 illustrate the program output as the data is 'set-up', line 25 is 'searched' by the parabolic method, and the final data output.

*** SAMPLE DATA INPUT FOR LINE-FITTING PROGRAM. ***

```
 25  27  30 179 182 190   5   2  30   1   1  17 232           256         1         1
(16F5.0)
     XE    SINGLES    S-2A
      23  107  599 19263891955550511385619862765590665853116052062922680306965 66
27007 581067042551085327055933592448234550092542208317889301789484123426193 21834
19931199472024422858298984269457803715268310298791 76369736370767433712620178 3
1566616602176121688915036124481061 0 9307 8452 7882 7447 7170 7278 7437 7214 7277
 7368 7094 7076 7016 7058 6844 6712 6714 6355 6425 6309 6274 6144 6547 6 22 71 5
 7673 8132 8023 8310 8180 8214 7982 7488 7133 6632 6451 6467 6590 6394 6159 6035
 6164 6252 6278 6554 7356 7730 8088 8080 7977 7696 7175 6651 6298 5976 5837 5751
 5510 5548 5645 5730 5870 5943 6130 5855 5805 5761 5795 5808 5806 5971 6200 6418
 6704 6996 7249 7324 7291 7263 7239 7082 6736 6689 6613 6276 6048 5634 5584 5257
 5231 4832 4775 4672 4575 4585 4663 4814 5113 5835 6653 7685 915710781121021 173
1309212619111154 9609 7861 6136 4947 3968 3378 2961 2797 2657 2707 3028 3523 4217
 5292 6204 7543 8788 959310011 9750 8883 7905 6477 5096 3844 2854 2126 1548 1177
  955  820  758  768  903  976 1099 1303 1362 1467 1519 1491 1354 1226 1095  9
  819  625  563  438  408  343  290  228  240  235  248  260  294  269  269  2
  250  220  201  173  158  145  123  120  117   98  119   90   96  104  115   84
   55   53   48   41   33   35   36   33   29   36   30   33   42   37   37   47
     XE    BKGND    S-2A
    10000
                                                     1195011161103 13 9722 9302 8934
 8686 7858 7282 6825 6391 6117 5988 5973 6323 7062 6940 5868 4886 4315 3969 3740
 3483 3295 3223 3117 3208 3334 3645 4000 4321 4464 4676 4678 4269 3591 2749 2336
 2276 2279 2384 2304 2150 1837 1634 1516 1428 1409 1369 1365 1352 1352 1333 1321
 1254 1278 1205 1155 1099 1043  976  979  949  913  913  913  908  905  936  976
  960  951  951  893  856  857  830  881  931 1052 1114 1219 1243 1202 1107  965
  850  801  733  717  720  721  719  743  755  749  731  710  658  639  617  617
  563  566  563  522  536  536  518  521  553  539  613  647  723  848  939 1141
 1213 1294 1291 1182 1047  888  744  581  539  514  512  517  486  462  467  457
  469  475  462  460  474  455  448  465  438  449  458  525  494  529  549  573
  519  543  520  490  438  461  441  399  410  398  395  382  374  377  377  396
  374  443  462  492  542  539  563  517  490  462  426  382  336  331  278  276
  277  279  280  290  291  284  310  280  270  248  254  243  208  203  166  159
  142  161  124  111  111  111   97   98   93   82   76   89   82   75   76   71
   73   73   63   71   67   71   78   70   84   90   79   68   71   64   56   50
   49   44   34   31   33   35   36   33   29   36   30   33   42   47   37   47
  17  18  25  28  43
  26  27
  255          10270  2010           9630
  17.269   20.705   25.347   26.819   29.565   32.836   36.633   39.630   43.169   45.
  51.263   55.385   61.617   65.799   70.464   75.000   81.980   86.322   95.073  10 .
 108.710  119.106  132.037  145.199  160.800  171.500  182.135  203.554  211.610  225.166
   155.0    192.0    240.0    253.0    285.0    316.0    358.0    388.0    428.0    455.0
   516.0    558.0    621.0    675.0    723.0    770.0    856.0    902.0    994.0   1082.
  1152.0   1265.0   1413.0   1566.0   1753.0   1885.5   2005.0   2269.0   2363.0   2500.0
  25
```

III.5.2

COMPUTER OUTPUT

XE SINGLES S-2A

INPUT DATA

-0.	23.	107.	599.	1926.	38919.	53550.	51138.	56198.	62965.	59066.	58311.	60520.	62922.	68506.	90566.
27007.	5810.	67042.	55108.	53270.	53933.	59244.	82345.	50092.	54220.	81788.	93017.	89948.	41234.	26199.	21664.
19931.	19947.	20244.	22858.	29898.	42694.	57803.	71526.	83102.	98791.	7636.	97368.	70767.	43871.	26290.	17863.
15666.	16602.	17612.	16889.	15036.	12448.	10610.	9307.	8452.	7882.	7447.	7170.	7278.	7437.	7214.	7277.
7368.	7094.	7076.	7016.	7058.	6844.	6712.	6714.	6355.	6425.	6309.	6274.	6144.	6547.	6722.	7176.
7673.	8132.	8023.	8310.	8180.	8214.	7982.	7488.	7133.	6632.	6451.	6467.	6590.	6399.	6159.	6065.
6164.	6252.	6278.	6554.	7356.	7730.	8088.	8080.	7977.	7696.	7175.	6651.	6298.	5976.	5837.	5731.
5510.	5548.	5645.	5730.	5870.	5943.	6130.	5855.	5805.	5761.	5795.	5808.	5806.	5971.	6200.	6418.
6704.	6996.	7249.	7324.	7291.	7263.	7239.	7082.	6736.	6689.	6613.	6276.	6048.	5634.	5584.	5237.
5231.	4832.	4775.	4672.	4575.	4585.	4663.	4814.	5113.	5835.	6653.	7685.	9157.	10761.	12102.	13173.
13092.	12619.	11154.	9609.	7861.	6136.	4997.	3968.	3378.	2961.	2797.	2657.	2707.	3028.	3523.	4219.
5292.	6204.	7543.	8788.	9593.	10011.	9750.	8883.	7905.	6477.	5096.	3844.	2854.	2126.	1548.	1177.
955.	820.	758.	768.	903.	976.	1099.	1303.	1362.	1467.	1519.	1491.	1354.	1226.	1095.	942.
819.	625.	563.	438.	408.	343.	290.	228.	240.	235.	248.	260.	294.	269.	269.	265.
250.	220.	201.	173.	158.	145.	123.	120.	117.	98.	119.	90.	96.	104.	113.	84.
55.	53.	48.	41.	33.	35.	36.	33.	29.	36.	30.	33.	42.	37.	37.	47.

XE BKGND S-2A

CØRRECTED INPUT

0.	23.	107.	599.	1926.	38919.	53550.	51138.	56198.	62965.	47116.	47150.	50207.	53200.	59204.	81632.
118321.	97952.	59760.	48283.	46879.	47816.	53256.	76372.	143769.	247158.	274848.	187149.	85062.	36919.	22230.	18124.
16448.	16652.	17021.	19741.	26690.	39360.	54158.	67526.	78781.	94327.	102960.	92690.	66498.	40280.	23545.	15547.
13390.	14323.	15228.	14585.	12886.	10611.	8976.	7791.	7024.	6473.	6078.	5805.	5926.	6085.	5881.	5756.
6114.	5816.	5871.	5861.	5959.	5801.	5736.	5735.	5406.	5512.	5396.	5361.	5236.	5642.	5786.	6200.
6713.	7181.	7072.	7417.	7324.	7357.	7152.	6607.	6202.	5580.	5337.	5248.	5347.	5197.	5052.	5040.
5314.	5451.	5545.	5837.	6636.	7009.	7369.	7337.	7222.	6947.	6444.	5941.	5640.	5337.	5220.	5114.
4947.	4982.	5082.	5208.	5334.	5407.	5612.	5334.	5252.	5222.	5182.	5161.	5083.	5123.	5261.	5273.
5491.	5702.	5968.	6142.	6244.	6375.	6495.	6501.	6197.	6175.	6101.	5759.	5562.	5172.	5117.	4780.
4762.	4357.	4313.	4212.	4101.	4130.	4215.	4349.	4675.	5386.	6195.	7160.	8663.	10252.	11553.	12600.
12573.	12076.	10634.	9119.	7423.	5675.	4556.	3569.	2968.	2563.	2402.	2275.	2333.	2651.	3146.	3873.
4918.	5761.	7081.	8296.	9051.	9472.	9187.	8366.	7415.	6015.	4670.	3462.	2518.	1795.	1270.	899.
678.	541.	478.	478.	612.	692.	789.	1023.	1092.	1219.	1265.	1248.	1146.	1023.	929.	783.
677.	464.	439.	327.	297.	232.	193.	130.	147.	153.	172.	171.	212.	194.	193.	214.
177.	147.	138.	102.	91.	74.	45.	50.	33.	8.	40.	22.	25.	40.	57.	54.
6.	9.	14.	10.	0.	0.	0.	0.	0.	0.	0.	0.	0.	0.	0.	0.

TØTAL BACKGRØUND

```
   -0.     -0.     -0.     -0.     -0.     -0.     -0.     -0.     -0.     -0.   11950.   11161.   10313.    9722.    9302.    8934.
 8686.   7858.   7282.   6825.   6391.   6117.   5988.   5973.   6323.   7062.    6940.    5868.    4886.    4315.    3969.    3740.
 3483.   3295.   3223.   3117.   3208.   3334.   3645.   4000.   4321.   4464.    4676.    4678.    4269.    3591.    2745.    2336.
 2276.   2279.   2384.   2304.   2150.   1837.   1634.   1516.   1428.   1409.    1369.    1365.    1352.    1352.    1333.    1321.
 1254.   1278.   1205.   1155.   1099.   1043.    976.    979.    949.    913.     913.     913.     908.     905.     936.     976.
  960.    951.    951.    893.    856.    857.    830.    881.    931.   1052.    1114.    1219.    1243.    1202.    1107.     965.
  850.    801.    733.    717.    720.    721.    719.    743.    755.    749.     731.     710.     658.     639.     617.     617.
  563.    566.    563.    522.    536.    536.    518.    521.    553.    539.     613.     647.     723.     848.     939.    1145.
 1213.   1294.   1281.   1182.   1047.    888.    744.    581.    539.    514.     512.     517.     486.     462.     467.     457.
  469.    475.    462.    460.    474.    455.    448.    465.    438.    449.     458.     525.     494.     529.     549.     573.
  519.    543.    520.    490.    438.    461.    441.    399.    410.    398.     395.     382.     374.     377.     377.     398.
  374.    443.    462.    492.    542.    539.    563.    517.    490.    462.     426.     382.     336.     331.     278.     278.
  277.    279.    280.    290.    291.    284.    310.    280.    270.    248.     254.     243.     208.     203.     166.     159.
  142.    161.    124.    111.    111.    111.     97.     98.     93.     82.      76.      89.      82.      75.      76.      71.
   73.     73.     63.     71.     67.     71.     78.     70.     84.     90.      79.      68.      71.      64.      56.      50.
   49.     44.     34.     31.     33.     35.     36.     33.     29.     36.      30.      33.      42.      37.      37.      47.
```

```
      HEIGHT          PØSITIØN          SIGMA

  0.27484800E 06  0.27000000E 02  0.20000000E 01
  0.25501486E 06  0.26663007E 02  0.16768093E 01
  0.27354375E 06  0.26724590E 02  0.15295562E 01
  0.27572421E 06  0.26716122E 02  0.15290274E 01
  0.27574156E 06  0.26715902E 02  0.15287541E 01
  0.27574489E 06  0.26715894E 02  0.15287164E 01
  0.27574532E 06  0.26715894E 02  0.15287117E 01
  0.27574538E 06  0.26715894E 02  0.15287112E 01

     CØNVERGENT      AFTER     8  ITERATIØNS

     FINAL      RESULTS

  0.27574538E 06  0.26715894E 02  0.15287111E 01

CHI-SQUARE=      2397.1  DEGREES  ØF  FREEDØM=        3.

ERRØR(A)=     10923.7      ERRØR(PØSITIØN)=       0.06      ERRØR(SIGMA)=       0.06

      HEIGHT          PØSITIØN          SIGMA

  0.94719999E 04  0.18200000E 03  0.50000000E 01
  0.92767991E 04  0.18206058E 03  0.42508476E 01
  0.93428307E 04  0.18207134E 03  0.42565389E 01
  0.93423974E 04  0.18207123E 03  0.42568356E 01

     CØNVERGENT      AFTER     4  ITERATIØNS
```

FINAL RESULTS

0.93423929E 04 0.18207122E 03 0.42568440E 01

CHI-SQUARE= 18.1 DEGREES ØF FREEDØM= 9.

ERRØR(A)= 64.3 ERRØR(PØSITIØN)= 0.05 ERRØR(SIGMA)= 0.05

ENERGY SCALE IS 10.1180 KEV/CHANNEL AND ZERØ IS AT CHANNEL 1.0544

THESE RESULTS CØRRECTED FØR ANALYZER AND DETECTØR NØN-LINEARITIES

INITIAL ZERØ SHIFT = 0.0000 , INITIAL GAIN SHIFT = 0.0000 , PER CHANNEL

LINE NØ. 25 INCREMENT NØ. 3 CALCULATIØN 1

CHI-SQUARED 0.82073720E 03 0.81277406E 03 0.18933501E 04
ENERGIES 1750.5467 1756.3347 1761.9583
CHANNEL NØS. 160.8000 161.3000 161.8000

LINE 25 CALCULATED TØ BE IN CHANNEL 161.0535, WITH ENERGY 1753.4813 KEV

CHI-SQUARED = 0.67549999E 03 DEGREES ØF FREEDØM = 185. ESTIMATED ERRØR = 0.4640 KEV

FINAL RESULTS

LINE	ENERGY	CHANNEL	INTENSITY	ERRØR
1	154.5803	17.26900	2.66065	0.01847
2	187.9544	20.70500	0.37381	0.01529
3	238.8814	25.34700	1.79120	0.03488
4	252.8518	26.81900	11.95828	0.04355
5	285.2008	29.56500	0.33340	0.01697
6	316.4939	32.83600	0.14483	0.01149
7	358.1234	36.63300	0.13780	0.01519
8	388.0956	39.63900	2.65150	0.02474
9	428.0601	43.16900	6.89109	0.03367
10	454.8542	45.85300	0.59059	0.02254
11	516.1277	51.26300	0.89108	0.01476
12	557.9620	55.38500	0.22173	0.01250
13	621.0771	61.61700	0.08819	0.01271
14	674.9256	65.79900	0.11056	0.01460

15	722.5581	70.46400	0.13826	0.01479
16	768.7360	75.00000	0.04852	0.01394
17	856.3956	81.98000	0.28075	0.01684
18	902.0136	86.32200	0.45088	0.01756
19	993.8806	95.07300	0.14124	0.01577
20	1082.6095	103.53300	0.72083	0.02139
21	1152.0798	108.71000	0.18012	0.02060
22	1264.6328	119.10600	0.07013	0.01797
23	1413.0073	132.03700	0.12588	0.02230
24	1565.4630	145.19900	0.17478	0.02183
25	1753.4464	161.05350	3.79302	0.03089
26	1885.3511	171.50000	0.12238	0.01955
27	2005.2306	182.13500	3.95904	0.02838
28	2268.5896	203.55400	0.61458	0.01521
29	2363.3907	211.61000	0.04859	0.01065
30	2499.9560	223.16600	0.11515	0.00746

CHI-SQUARED = 0.6663817E 03, DEGREES ØF FREEDØM = 185.

CALCULATED SPECTRUM FRØM CHANNEL ØNE TØ CHANNEL 256

39662.	39662.	39662.	39683.	39730.	39819.	40180.	40974.	42098.	44594.	48347.	51243.	52862.	50922.	55958.	70[illegible].
118173.	99189.	56849.	48122.	48344.	46767.	52253.	78355.	140968.	250664.	274485.	185780.	85220.	37207.	22102.	17959.
16866.	16333.	16909.	20160.	26438.	39033.	55031.	67152.	78456.	94689.	103133.	92593.	66512.	40391.	23608.	15480.
13397.	14281.	15292.	14716.	12767.	10592.	8987.	7893.	7039.	6385.	5991.	5903.	5953.	6004.	5973.	5972.
5978.	5953.	5880.	5844.	5854.	5867.	5813.	5671.	5510.	5386.	5329.	5338.	5434.	5611.	5856.	6251.
6674.	7014.	7181.	7365.	7440.	7367.	7097.	6643.	6114.	5661.	5359.	5203.	5174.	5189.	5198.	5194.
5213.	5330.	5571.	5919.	6468.	7015.	7378.	7467.	7265.	6852.	6399.	5984.	5645.	5381.	5180.	5047.
4989.	5013.	5101.	5223.	5348.	5431.	5449.	5403.	5316.	5218.	5141.	5108.	5126.	5189.	5284.	5406.
5549.	5723.	5902.	6068.	6211.	6326.	6409.	6448.	6421.	6312.	6123.	5861.	5565.	5267.	5008.	4786.
4599.	4439.	4301.	4189.	4116.	4105.	4190.	4405.	4811.	5501.	6425.	7548.	8736.	10143.	11361.	12134.
12283.	11783.	10685.	9180.	7530.	5973.	4655.	3647.	2936.	2482.	2244.	2190.	2318.	2652.	3260.	4016.
4942.	5907.	7115.	8185.	8927.	9199.	8981.	8280.	7208.	5946.	4675.	3530.	2583.	1852.	1321.	956.
722.	589.	540.	545.	596.	682.	790.	933.	1068.	1173.	1231.	1228.	1176.	1073.	937.	789.
645.	517.	410.	325.	261.	214.	182.	163.	154.	153.	162.	175.	187.	195.	197.	191.
178.	159.	135.	110.	87.	66.	49.	35.	25.	17.	12.	8.	5.	4.	2.	2.
1.	1.	1.	0.	0.	0.	0.	0.	0.	0.	0.	0.	0.	0.	0.	0.

DIFFERENTIAL RESIDUAL RATIØS

0.00	0.00	0.00	0.00	0.00	0.00	0.00	0.00	0.00	0.00	0.00	0.00	0.00	0.00	0.00	0.00
0.40	-3.67	10.68	0.65	-6.00	4.28	3.93	-6.67	7.08	-6.86	0.68	3.07	-0.51	-1.35	0.74	0.97
-2.73	2.10	0.73	-2.60	1.39	1.52	-3.52	1.36	1.10	-1.13	-0.52	0.30	-0.05	-0.51	-0.37	0.47
-0.05	0.30	-0.45	-0.95	0.91	0.16	-0.10	-0.98	-0.15	0.92	0.93	-1.06	-0.29	0.87	-1.00	-0.17
1.47	-1.49	-0.10	0.19	1.16	-0.74	-0.88	0.73	-1.22	1.47	0.79	0.27	-2.36	0.36	-0.80	-0.56
0.42	1.75	-1.15	0.54	-1.22	-0.11	0.58	-0.39	0.98	-0.92	-0.25	0.51	1.96	0.09	-1.71	-1.84
1.20	1.44	-0.31	-0.96	1.87	-0.06	-0.10	-1.38	-0.46	1.03	0.51	-0.50	-0.06	-0.54	0.50	0.64

-0.55	-0.40	-0.24	-0.19	-0.18	-0.30	2.00	-0.87	-0.81	0.05	0.51	0.66	-0.54	-0.79	-0.28	-1.53
-0.66	-0.23	0.72	0.80	0.36	0.54	0.96	0.61	-2.63	-1.61	-0.26	-1.24	-0.04	-1.21	1.41	-0.08
2.16	-1.13	0.16	0.32	-0.21	0.35	0.36	-0.77	-1.83	-1.45	-2.72	-4.28	-0.75	1.02	1.71	3.98
2.48	2.55	-0.47	-0.60	-1.18	-3.67	-1.35	-1.18	0.52	1.40	2.80	1.54	0.27	-0.02	-1.83	-2.83
-0.32	-1.79	-0.38	1.16	1.24	2.66	2.03	0.89	2.26	0.83	-0.07	-1.04	-1.15	-1.15	-1.18	-1.49
-1.25	-1.44	-1.92	-2.06	0.47	0.27	-0.02	2.27	0.60	1.11	0.81	0.49	-0.75	-1.33	-0.22	-0.18
1.03	-1.89	1.10	0.07	1.59	0.84	0.54	-1.84	-0.41	-0.02	0.53	-0.20	1.30	-0.05	-0.20	1.20
-0.07	-0.70	0.19	-0.54	0.27	0.53	-0.27	1.07								

FØLLØWING IS A PLØT ØF THE DIFFERENTIAL RESIDUAL RATIØ ,R/SIGMA

THE VERTICAL SCALE IS 0.43 PER LINE

YMAX	YMIN	XMAX	XMIN	HEIGHT	WIDTH
0.11744121E 02	-0.11744121E 02	0.12800000E 03	0.00000000E-38	54	128

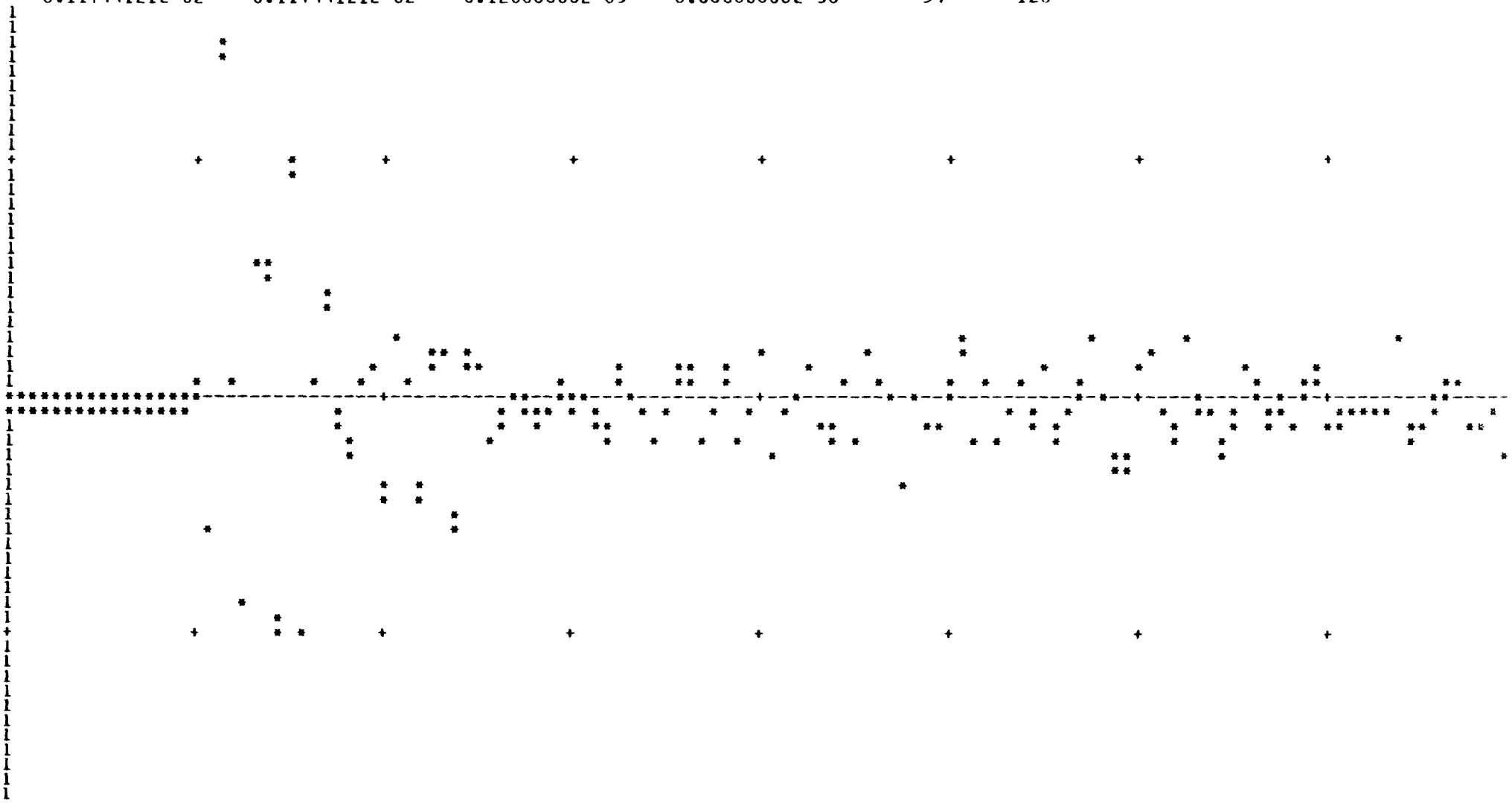

YMAX	YMIN	XMAX	XMIN	HEIGHT	WIDTH
0.11744121E 02	-0.11744121E 02	0.12800000E 03	0.00000000E-38	54	128

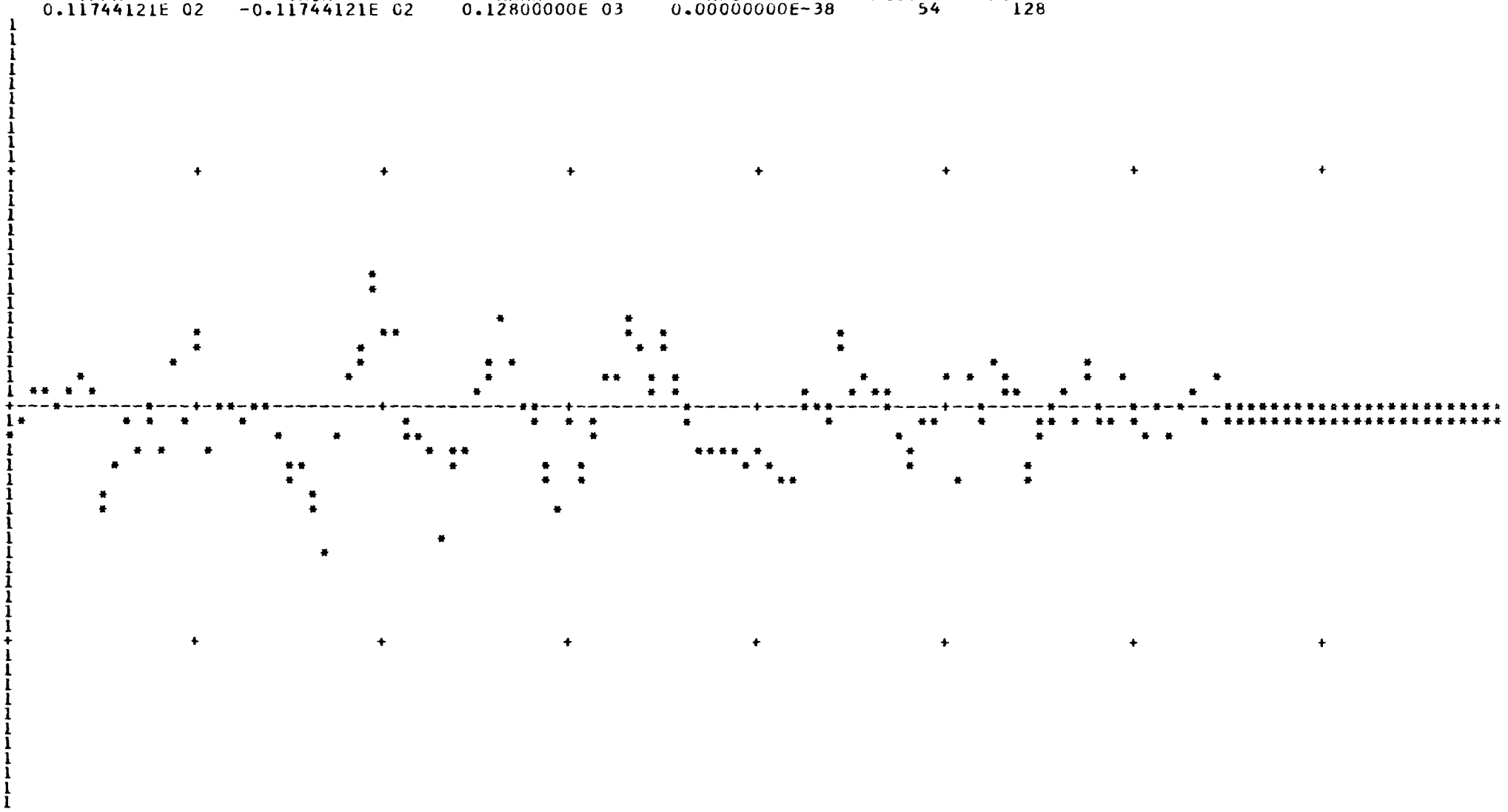

$CARD READ

00313 N.P.ARCHER 100 006MIN 10SEC CØST$022.25 REM. TIME 0160MIN 16SEC

McMASTER UNIVERSITY

FORM 66 43 75

REFERENCES

1. M. A. Preston, Physics of the Nucleus, Chapter 15 (Addison-Wesley, 1962).

2. J. M. Blatt and V. F. Weisskopf, Theoretical Nuclear Physics, Chapter 13 (Wiley, 1952).

3. S. A. Moszkowski, Phys. Rev. 82, 35 (1951).

4. A. H. Wapstra et al, Nuclear Spectroscopy Tables, North-Holland Publishing Co. (1959).

5. E. Feenberg, Shell Theory of the Nucleus, Chapter 5 (Princeton University Press, 1955).

6. V. F. Weisskopf, Phys. Rev. 83, 1073L (1951).

7. S. A. Moszkowski, Phys. Rev. 83, 1071L(1951).

8. L. A. Sliv and I. M. Band, Electron Conversion Coefficients (U.S.S.R. Academy of Sciences).

9. M. E. Rose, Internal Conversion Coefficients, North-Holland Publishing Co. (1958).

10. M. G. Mayer, Phys. Rev. 75, 1969L (1949).

11. O. Haxel et al, Phys. Rev. 75, 1766L (1949).

12. L. Nordheim, Phys. Rev. 78, 294 (1950).

13. M. H. Brennan and A. M. Bernstein, Phys. Rev. 120, 927 (1960).

14. A. deShalit and J. D. Walecka, Nuclear Physics, 22, 184 (1961).

15. C. J. Gallagher and S. A. Moszkowski, Phys. Rev. 111, 1282 (1958).

16. J. R. Erskine, quoted in private communication from Reference 17.

17. Y. E. Kim and J. O. Rasmussen, Phys. Rev. 135, B44 (1964).

18. B. L. Cohen, Phys. Rev. 130, 227 (1963).

19. L. S. Kisslinger and R. A. Sorenson, Rev. Mod. Phys. 35, 853 (1963).

20. O. Hahn and F. Strassman, Naturwiss. 28, 54 (1940).

21. G. N. Glasoe and J. Steigman, Phys. Rev. 58, 1 (1940).

22. S. Thulin et al, Phys. Rev. 76, 871 (1949).

23. W. B.Clarke and H. G. Thode, Can. J. Phys. 42, 213 (1964).

24. P. Patzelt and G. Hermann, Paper SM-60/60, Symposium on Physics and Chemistry of Fission, Salzburg (1965).

25. S. Nassiff and W. Seelman-Eggebert, Z. Naturforsch 10A, 83 (1955).

26. S. Thulin, Arkiv für Fysik 9, 137 (1955).

27. D. W. Ockenden and R. H. Tomlinson, Can. J. Chem. 40, 1594 (1962).

28. V. V. Ovechkin and N. N. Demidovich, Soviet Physics JETP 47, 1123 (1965).

29. A. C. Wahl, Radioactivity Applied to Chemistry, P. 182 (Wiley, 1951).

30. A. C. Wahl et al, Phys. Rev. 126, 1112 (1962).

31. F. F. Momyer, The Radiochemistry of the Rare Gases, NAS-NS 3025 (1960).

32. R. C. Koch and G. L. Grandy, Nucleonics 18, 76 (1960).

33. L. B. Loeb, Kinetic Theory of Gases, P. 325 (McGraw-Hill, 1927).

34. A. I. M. Keulemans, Gas Chromatography, Chapter 4 (Reinhold, 1957).

35. A. H. Snell and F. Pleasonton, Phys. Rev. 111, 1338 (1958).

36. S. J. Nassiff and W. Seelman-Eggebert, First Geneva Conf. on Peaceful Uses of Atomic En., 7, 193 (1955).

37. L. V. Johnson, Undergraduate Thesis, Eng. Dept., McMaster University (1964).

38. R. M. Bartholomew and A. P. Berg, Can. J. Chem., 34, 201 (1956).

39. M. E. Bunker et al, Phys. Rev. 103, 1417 (1956).

40. H. B.Evans et al, Paper 157, Radiochemical Studies: The Fission Products, Book 2, McGraw Hill (1951).

41. C. R. Dillard et al, Paper 68, Radiochemical Studies: The Fission Products, Book 2, McGraw Hill (1961).

42. H. J.Fiedler et al, Nucl. Inst. Methods, (to be published).

43. G. Murray et al, Nuclear Physics 63, 353 (1965).

44. A. H. Wapstra et al, Nuclear Physics 1, 245 (1956).

45. G. Lindström et al, Proc. Phys. Soc. 66B, 54 (1963).

46. T. Alväger, Arkiv für Fysik 17, 521 (1960).

47. T. J. Kennett et al, Nucl. Inst. Methods 29, 325 (1964).

48. Nuclear Data Sheets, Nat. Acad. Science-NRC (U.S.A.), U.S. Gov't. Printing Office, Washington, D.C.

49. T. J. Kennett et al, Nuclear Physics 58, 56 (1964).

50. T. J. Kennett, Rev. Sci. Inst. 35, 1230 (1964).

51. N. R. Johnson and G. D. O'Kelley, Phys. Rev. 108, 85 (1957).

52. C. D. Broyles et al, Phys. Rev. 89, 715 (1953)

53. D. D. Slavinskas et al, Nucl. Inst. Methods (to be published).

54. P. A.Seeger, Nuclear Physics 25, 1 (1961).

55. L. M. Langer et al, Phys. Rev. 89, 907A (1953).

56. O. Hansen and O. Nathan, Nuclear Physics 42, 197 (1963).

57. M. K. Pal and D. Mitra, Nuclear Physics 42, 221 (1963).

APPENDIX REFERENCES

R1 R. H. Moore, Applications of Computers to Nuclear and Radiochemistry NAS-NS3107, 305 (1962).

R2 J. P. Deutsch and P. Lipnik, Nuclear Physics 61, 97 (1965).

R3 R. Nordhagen and A. Iveter, Nuclear Physics 63, 529 (1965).

R4 G. Backenstross et al, Nuclear Physics 62, 449 (1965).

R5 E. J. Whittaker and G. Robinson, The Calculus of Observations, Chapter 12, (Blackie and Son (1958).

R6 P. G. Guest, Numerical Methods of Curve Fitting, Cambridge University Press (1961).

R7 Y. V. Linnik, Method of Least Squares, Pergamon Press (1961).

R8 K. Pearson, Phil. Mag. 50, 157 (1900).

R9 Student, Biometrics VI, 1 (1908).

R10 C. D. Zerby and H. S. Moran, Nucl. Inst. and Methods 14, 115 (1961).

R11 W. F. Miller and W. J. Snow, Rev. Sc. Inst. 31, 39 (1960).

R12 N. E. Scofield, Applications of Computers to Nuclear and Radiochemistry, NAS-NS 3107, 108 (1962).

R13 A. H. Wapstra and J. Oberski, Applications of Computers to Nuclear and Radiochemistry, NAS-NS3107, 137, (1962).

R14 R. L. Heath et al, USAEC Report No. IDO-17017 (1965).

R15 R. L. Heath, Applications of Computers to Nuclear and Radiochemistry, NAS-NS3107, 93 (1962).

R16 R. L. Heath, Scintillation Spectrometry, P.13, USAEC Report IDO-16880-1 (1964).

R17 R. L. Heath, Paper 5.2, U.S.AEC Report CU(PNPL) 227 (1962).

R18 E. Breitenberger, Progress in Nuclear Physics 4, 56 (1955).

R19 D. Engelkemeir, Rev. Sci. Inst. 27, 589 (1956).

R20 W. V. Prestwich, Ph.D. Thesis, McMaster University (1963).

R21 C. D. Zerby, Nuclear Inst. Methods 14, 115 (1961).

R22 D. F. Crouch and R. L. Heath, USAEC Report No. IDO-16923 (1963).